AFOSR Research Grant FA9550-15-1-0407

Faster-than-Realtime Electrostatic Force and Torque Modeling for SSA Applications

(2017 Annual Report)

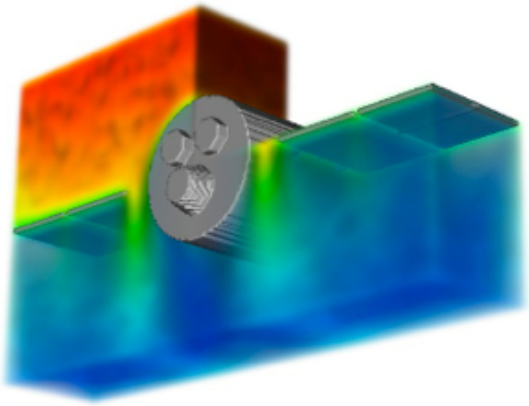

Principal Investigators:

Hanspeter Schaub[1] (PI)
University of Colorado, Boulder, CO 80309-0431

September 14, 2017

[1]Professor, Glenn L. Murphy Chair, hanspeter.schaub@colorado.edu, (303) 492-2767

Table of Contents

Chapter 1

Technical Progress Reports

This chapter discusses the technical results achieved over the last project year. The sections and sub-sections are numbered to match the research thrusts and tasks outlined in the GANTT chart in Figure **??**.

1.1 Research Thrust 1: MSM Development

1.1.1 E-field based MSM Development

1.1.1.1 Multi-Sphere Method Background

MSM provides a computationally fast approximate model of a spacecraft's electrostatic properties for applications that require faster-than-realtime results. MSM solves for the force and torque on a conductor by first finding the charge on a number of virtual spheres placed within the body. The charge on the spheres is found by assuming all spheres are equipotential across a single space object and solving a linear system of equations. MSM divides into VMSM, which uses a small number of spheres placed within the *volume* of the conductor, and SMSM, which places a large number of spheres on the *surface* of the conductor. It is more difficult to generate VMSM models because the size and location of the spheres must be found using an optimizer; however, VMSM models are much faster to run once completed due to the much smaller number of sphere employed. In contrast, SMSM models are easier to set up because the sphere locations are specified, and the sphere size can be found by matching self capacitance, which is computed from commercial FEM software. Generally, SMSM models show higher accuracy when compared to FEM-generated force and torque data.[1] Although SMSM greatly reduces the effort required to create a MSM model for a given spacecraft geometry and increases the accuracy of the model, it comes at increased computational cost at runtime due to the large number of spheres.

Both the Volume Multi-Sphere Method and Surface Multi-Sphere Method represent a conducting object as N spheres, as shown in Figure 1.1. These methods only differ in the number, size and placement of the spheres used to represent the conductor. The MSM formulation currently assumes that the surface of the target craft or debris is perfectly conducting, which implies that all MSM spheres that constitute a model are equipotential.

The charge on each sphere, which may include multiple distinct spheres outside of the target model, is only a function of the sizes of the spheres in the complete model and their relative positions. Letting N_T be the total number of MSM spheres in a MSM model, computed as the sum of the number of spheres in the target model and the number of spheres outside the target

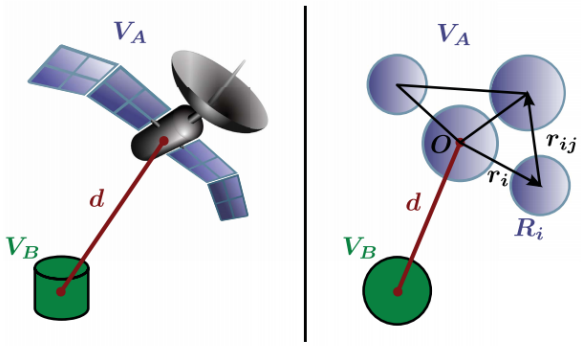

Figure 1.1: *Illustration of the MSM concept showing how two conducting space objects are decomposed into a series of body-fixed sphere with the same potential.*[2]

model, all MSM spheres can approximated as point charges. The $N_T \times 1$ charge matrix, $\mathbf{q} = \begin{bmatrix} q_1 & q_2 & \dots & q_{N_T} \end{bmatrix}^T$, which contains the charge on each sphere of a MSM model, is related to the $N_T \times 1$ sphere voltage matrix $\mathbf{V} = \begin{bmatrix} V_1 & V_2 & \dots & V_{N_T} \end{bmatrix}^T$ through Eq. (1.1)[3]

$$\mathbf{q} = \frac{1}{k_c} [C_M] \mathbf{V} \tag{1.1}$$

where $k_c = 1/4\pi\epsilon_0$ is the Coulomb constant, and the $N_T \times N_T$ matrix $\frac{1}{k_c}[C_M]$ is the Position Dependent Capacitance (PDC) matrix. For a general N_T sphere MSM model, the PDC matrix is difficult to produce; however, its inverse, the elastance matrix $[S]$, contains only functions of the sphere radii R_i and relative distances between spheres $r_{i,j}$. $[S]$ is formulated as shown in Eq. (1.2)[4]

$$[S] = k_c \begin{bmatrix} \frac{1}{R_1} & \frac{1}{r_{1,2}} & \dots & \frac{1}{r_{1,N_T}} \\ \frac{1}{r_{2,1}} & \frac{1}{R_2} & \dots & \frac{1}{r_{2,N_T}} \\ \vdots & \vdots & \ddots & \vdots \\ \frac{1}{r_{N_T,1}} & \frac{1}{r_{N_T,2}} & \dots & \frac{1}{R_{N_T}} \end{bmatrix} \tag{1.2}$$

The charges, which lead to the force and torque, are found by solving the linear system. For an isolated conductor with a small number of spheres this can be done analytically,[5] but in the majority of cases it is done numerically. This computation is expensive if many spheres are used, and is the cause of decreased run-time performance when using the SMSM method.

The charge set $\mathbf{q}$ is calculated using Eq. (1.1). The charges, q_i, are used to calculate the electric field produced by the model, and forces and torques that an object model experiences subject to one or more external point charges. Denoting the position vector of an external point charge as $\mathbf{r}_k$ and the relative position vector of each MSM model sphere with respect to its center of mass as $\mathbf{r}_i$, the force, $\mathbf{F}$, and torque, $\mathbf{T}_O$, applied to the target model about its center of mass by all external spheres with charges q_k are given in Eqs. (1.3) and (1.4)[2]

$$\mathbf{F} = -k_c \sum_{k=1}^{M} q_k \sum_{i=1}^{N} \frac{q_i}{||\mathbf{r}_{i,k}||^3} \mathbf{r}_{i,k} \tag{1.3}$$

$$\mathbf{T}_O = -k_c \sum_{k=1}^{M} q_k \sum_{i=1}^{N} \frac{q_i}{||\mathbf{r}_{i,k}||^3} \mathbf{r}_i \times \mathbf{r}_{i,k} \tag{1.4}$$

where $\mathbf{r}_{i,k}$ is the relative position of the k^{th} external sphere with respect to the i^{th} internal MSM sphere as shown in Figure 1.1. Let N be the total number of spheres in the target model, while M is the total number of spheres external to the target such that $N_T = N + M$. Adding arbitrary numbers of external spheres does not add to the complexity of MSM modeling because they can be appended to the charge and elastance matrices; however, doing so will increase computational burden–primarily due growing size of the elastance matrix, which always needs to be inverted. Whole MSM models can be appended when the calculation of force and torque between two complex geometries is desired. The electric field at any point exterior to the spheres of a MSM model is given by the superposition of the electric fields of each sphere, as shown in

$$\mathbf{E} = k_{\mathsf{c}} \sum_{i=1}^{N_T} \frac{q_i}{||\mathbf{r}_{i,l}||^3} \mathbf{r}_{i,l} \tag{1.5}$$

where l is a point of interest in the space outside of the MSM model spheres, and $\mathbf{r}_{i,l}$ is the relative position between the i-th MSM model sphere and l.

Prior VMSM model fitting methods minimize a cost function based upon the difference between the force and torque vectors predicted by a VMSM model and the force and torque vectors generated by commercial FEM software. One such cost function is given in Reference 5 by

$$J = \frac{100}{2L} \left(\sum_{l=1}^{L} \frac{||\mathbf{F}_{\text{VMSM},l} - \mathbf{F}_{\text{FEM},l}||}{||\mathbf{F}_{\text{FEM},l}||} + \frac{||\mathbf{T}_{\text{VMSM},l} - \mathbf{T}_{\text{FEM},l}||}{||\mathbf{T}_{\text{FEM},l}||} \right) \tag{1.6}$$

To alleviate far-field data noise effects in the optimization process, current methods utilize a self-capacitance constraint is proposed in Reference 5. Enforcing the VMSM model match the self capacitance of the target object ensures that the forces will match as the two objects get very far from each other. The self-capacitance C of a MSM model is given by[5]

$$C = \frac{Q}{V} = \frac{\sum_{i=1}^{N} q_i}{V} = \frac{1}{k_{\mathsf{c}}} \sum_{i=1}^{N} \sum_{j=1}^{N} (C_{\mathsf{M}})_{ij} \tag{1.7}$$

To enforce a self-capacitance constraint, the self-capacitance of the target geometry is calculated using FEM and the MSM model self-capacitance is matched to the FEM result– reducing the optimizer search space by one dimension. The capacitance matching can be accomplished analytically for simple models, or numerically for large models. Matlab's *fmincon* optimizer allows the self-capacitance constraint to be defined in a constraint function and enforced numerically.

1.1.1.2 Electric Field VMSM Model Fitting

1.1.1.2.1 SMSM E-field Data Generation

Using the current VMSM methodology, the sphere positions and radii are varied by an optimizer to best match force and torque data produced by a commercial FEM program.[2,3,5] This methodology requires significant hand-tuning of model parameters for a model that fits force and torque data accurately due to noisy FEM data in the far field, dependance on probe size, and convergence properties of the force and torque cost function. Recent work largely streamlines the process of generating VMSM models using ANSYS Maxwell 3D to generate numerical data.[5] The workflow for current VMSM model fitting starts with generating solid models for a target and probe geometry in FEM software and calculating accurate force and torque values between them at many relative positions. Self-capacitance of the target spacecraft is also calculated.

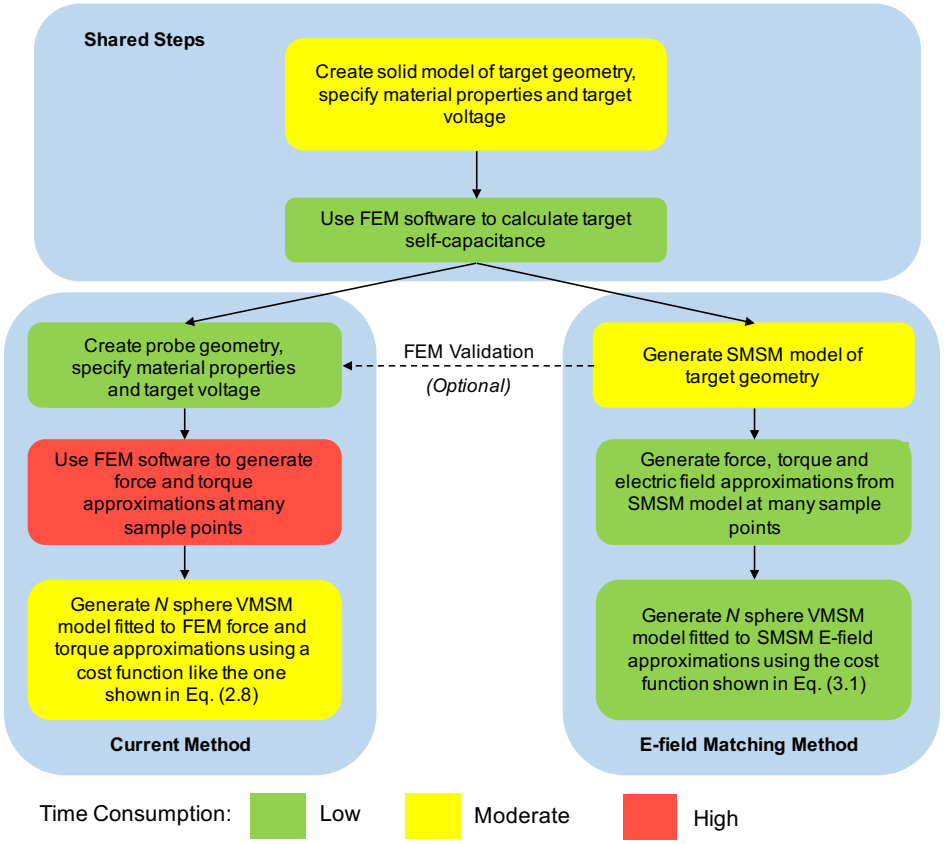

Figure 1.2: *Proposed Workflow Comparison with Previous Force and Torque Methods*

Generating the FEM truth data is by far the most time-consuming step. A complete sweep of locations for force and torque matching and validation may take hours and variations in accuracy depend heavily upon how many data points are used. In addition, complicated workarounds that automatically change probe radius are required to get accurate results when the object/probe separation distance is large. Current techniques use a spherical probe which has a radius that is a function of its distance from a target. The dependence on external probe geometry for force and torque calculations is clear in the above force and torque equations. This dependence is included into VMSM model generation when a cost function based on force and torque is used.

The workflow proposed in this paper seeks to address both of these issues. The initial step in modeling is the same — a single solid model of the target spacecraft is created. However, a solid model of external probe geometry is optional, and only used to gather limited force and torque data for verification of a model. A target voltage is prescribed and FEM software is used to calculate the self-capacitance of the target.

A SMSM model of the target geometry is then generated using any appropriate method. Note that the VMSM setup process in this paper is not tied to using SMSM in this step, but other fast methods such as a boundary element method or the method of moments could be used as well. All these solutions provide fast and accurate E-field predictions about a general shape. The SMSM method is used here because it provides an infinitely smooth E-field prediction and it's simplicity to setup. One SMSM development method, appropriate for spherical and cylindrical geometries, is to use a golden spiral algorithm to distribute SMSM spheres on the surface of the geometry.[2] A method appropriate for flat geometries is to use a function like MATLAB's *meshgrid* to generate a distribution of sphere positions on the surface of a plane. This distribution can then

be translated, rotated and combined with other planar distributions of spheres to form complex SMSM geometries.[6] When combining distributions, care should be taken to eliminate redundant spheres so that none overlap. Root finders like Matlab's *fsolve* can then be used with Eq. (1.7) to determine appropriate sphere radii to match the SMSM model self-capacitance to the self-capacitance of the solid model. Using the prescribed target voltage and Eq. (1.1), the charge on each SMSM sphere is calculated. Using the same equation applied to an N-sphere VMSM model optimization problem, an optimizer is used to select the optimal positions and radii of the model spheres to minimize the following cost function at sample points l

$$J\left(R_1, R_2, \ldots, R_N, \mathbf{r}_1, \mathbf{r}_2, \ldots, \mathbf{r}_N\right) = \sum_{l=1}^{L} \frac{||\mathbf{E}_{VMSM,l} - \mathbf{E}_{SMSM,l}||}{||\mathbf{E}_{SMSM,l}||} \tag{1.8}$$

where L is the total number of electric field sample points.

Using this cost function results in several major improvements to the prior methodology. The first improvement is the separation of VMSM model generations from any external probe geometry. Next, while the torques go to zero about particular symmetry axes, causing issues computing the relative MSM fit error, the E-field is always non-zero at any location relative to a charged spacecraft outside the convex hull formed by its conducting surface. The final improvement is in the time required to complete all the steps in generating a VMSM model. Although the proposed E-field fitting methodology adds the step of creating a SMSM model for a given target geometry and voltage, this process requires significantly less computational effort than computing forces and torques at many relative positions with FEM. While the FEM takes a few minutes to compute the force and torque at each position, a SMSM model with a few hundred spheres will compute the electric field at a few tens or hundreds of positions in a less than a minute. Reference 5 discusses fitting to much smaller numbers of force and torque data points; however, using the proposed method, hundreds of data points are calculated rapidly and used to create a VMSM model in much less than the time it requires to calculate one force and torque calculation using commercial FEM software. A flowchart comparing the previous force and torque optimization procedure and the proposed E-field matching method is included in Figure 1.2. The fitting speed are compared in detail in the following numerical simulation sections.

1.1.1.2.2 SMSM Validation

Before optimizing on a cost function built from a SMSM model, it is prudent to compare the accuracy of SMSM to other methods. The Method Of Images (MOI) provides an analytic infinite series solution to the problem of predicting the force between two spherical conductors.[7,8] The method consists of placing smaller and smaller image charges within the body of each sphere to balance out the potential on the surfaces. As the number of image charges increases, the solution converges.

SMSM models of spheres are made with a variable number of spheres, and the force between the two bodies is compared to that predicted by MOI. For this case, two spheres with 1 meter radius are separated by 5 meters, and charged to $\pm$10 kV. The SMSM model is shown in Fig. 1.3(a), a cartoon for MOI showing the iterative charges is shown in Fig. 1.3(b), and the results are plotted in Figure 1.3(c).

The x-axis indicates either the number of images charges used in each sphere for the MOI, or the number of individual spheres in each SMSM sphere. The MOI converges with 40 image charges, and SMSM converges with around 100 spheres. Since both methods converge to the same value, SMSM is validated as a method for predicting forces and torques on a sphere.

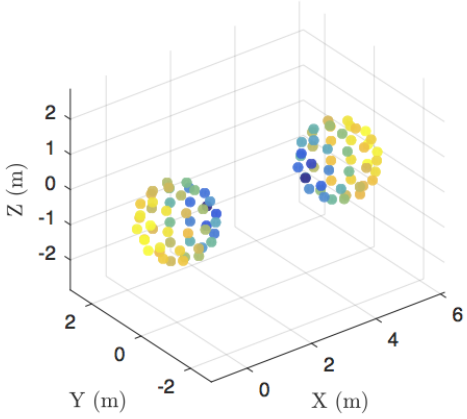

(a) SMSM schematic, color indicates charge

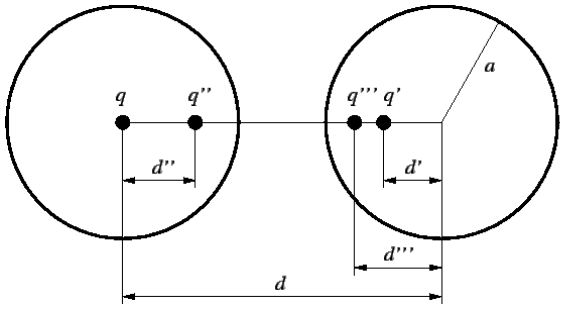

(b) MOI iterative image charge placement illustration

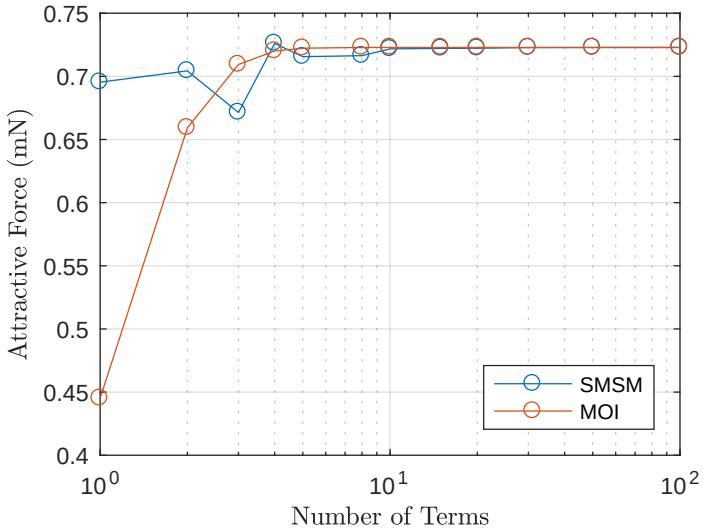

(c) Comparison Between MOI and SMSM

Figure 1.3: *Comparison of MOI and SMSM for predicting force on two spheres*

Now consider a more complex shape for which there is no analytical answer to compare to. In this case SMSM must be compared to an FEM program. Force and torque accuracy of a box-and-panel SMSM model with respect to FEM analysis is shown in Figure 1.4. Average force and torque errors of the SMSM model are within a few percent of FEM-computed forces and torques.

The errors are shown via color in Figures 1.4(a) and 1.4(b) and the shell-averaged error is shown in Fig. 1.4(c). The color plots show that the error is concentrated across certain directions. For instance, the torque errors are greatest along the negative z axis. This is because the actual torque is very near zero along that direction and thus it is very susceptible to FEM grid noise. The shell-averaged errors also show some interesting structure - the errors initially drop from around 5% down to around 2.5% at near 10 meter separations, and then climb up to around 4% at 15 meters. This may be due to two opposite trends that become more or less dominant with distance. At very close distances ($\sim$ 5 meters), FEM performs very well and grid resolution is not a problem, but the relatively coarse nature of SMSM gives large errors. At medium distances ($\sim$10

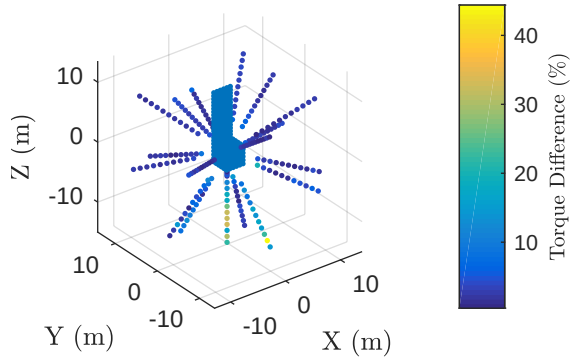

(a) SMSM Torque Error with Respect to FEM

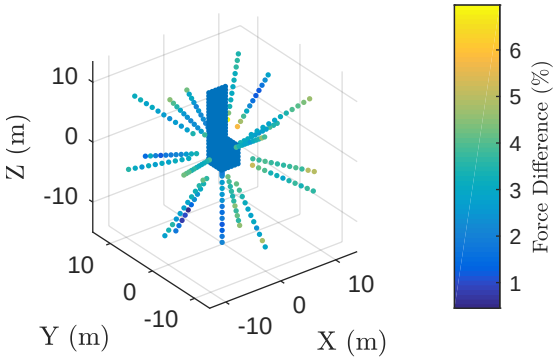

(b) SMSM Force Error with Respect to FEM

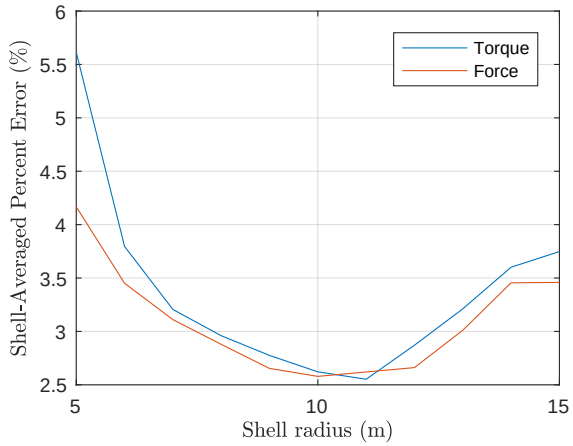

(c) SMSM Force and Torque Errors with Respect to FEM

Figure 1.4: *SMSM Force and Torque Errors*

meters) FEM is still performing well, but the increased distance causes grid resolution problems which increase FEM grid noise and decrease the accuracy of the FEM solution, however, SMSM increases in accuracy due to the increased separation distance. At far separations ($\sim$15 meters), the grid noise is very large which causes increased differences from the truth, even though SMSM is performing very well at this distance. It is thought that the middle region near 10 meters is where the increase in SMSM accuracy from being far apart best balance out the errors in FEM accuracy from grid noise.

1.1.1.2.3 Target Geometry, Data Generation and Optimization Methods

Two target geometries are used to compare the proposed E-field matching method to the previous force and torque method and to establish the accuracy of models generated using E-field matching. A two-sphere VMSM model is created for a charged cylinder, with a radius of 0.5 m and a height of 3 m, centered at the origin and oriented along the y-axis using the E-field matching method. This geometry is selected for easy comparison to previous work using force and torque matching.[2,3,5]

Data for the study involving the cylinder geometry are generated at evenly spaced intervals on 90 degree arcs centered at the origin, lying in the x-y plane and in the fourth quadrant. The

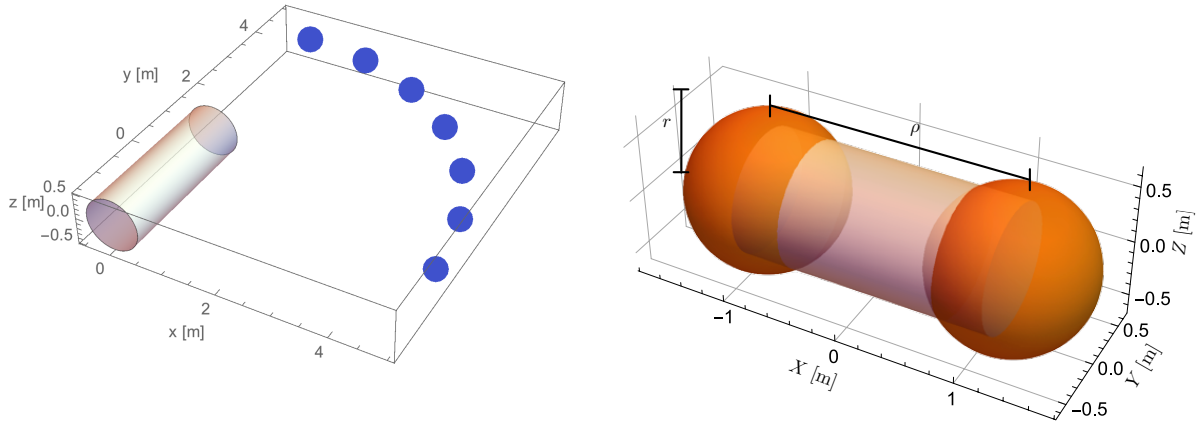

(a) Distribution of Sample Points Around Cylinder

(b) Two-Sphere VMSM Cylinder Model with Parameter Annotations[5]

Figure 1.5: *Cylinder Data Distribution and VMSM Model Parameters*

symmetry of the cylinder model requires data in only one quadrant for the optimization process. Force and torque data is generated using Maxwell 3D at the selected sample points. A SMSM model of the cylinder, shown in Figure 1.6, is created to generate E-field data at the same sample points. Only sample points lying on the arc of a 5 m radius circle are used for optimization, as shown in Figure 1.5(a).

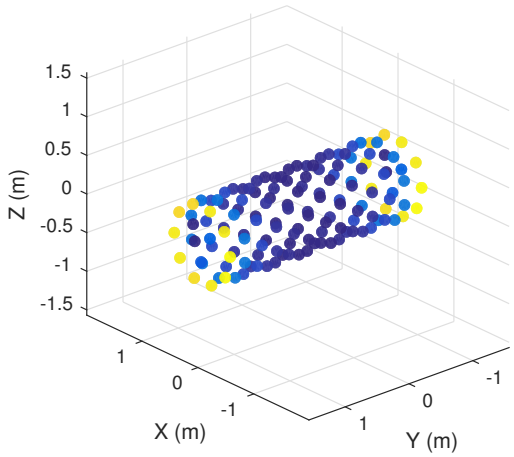

Figure 1.6: *SMSM Model of a Cylinder, Color Indicates Charge*

Two optimization methods are used to generate cylinder VMSM models: a global optimization method using Mathematica's Differential Evolution algorithm is used to optimize the force and torque cost function of Eq. (1.6), and MATLAB's *fmincon* local optimizer is used to minimize the E-field cost function of Eq. (1.8). Self-capacitance for the cylinder is calculated using Maxwell 3D.

Since a two-sphere VMSM model is used to represent the cylinder and the cylinder has symmetry about the x-axis, the VMSM model can be parameterized by one radius value r, which is

shared by both spheres, and the separation distance, ρ, between the two spheres. This model is shown in Figure 1.5(b).

Using this model, an exact formula for the VMSM model self-capacitance can be derived[5]

$$C = \frac{1}{k_c}\frac{2r\rho}{r+\rho} \tag{1.9}$$

where r and ρ are the radius and separation of the spheres as shown in Fig. 1.5(b). Imposing a self-capacitance constraint, matching the VMSM model self-capacitance to the value calculated by FEM, ensures that Lorentz forces and far-field Coulomb forces are automatically matched. In addition, it reduces the optimization problem to one dimension, because for any r value there is only one corresponding ρ value for which the constraint is met. Solving Eq. (1.9) for ρ yields[5]

$$\rho = \frac{rC_{\text{mod}}}{2r - C_{\text{mod}}} \tag{1.10}$$

where

$$C_{\text{mod}} = k_c C \tag{1.11}$$

Since C_{mod} is a scaling of the self-capacitance, it is used to impose the self-capacitance constraint in the following studies because its value is on the order of model parameters. Both the optimal r and ρ values are solved for using *fmincon* and the self-capacitance constraint is imposed numerically.

The second target spacecraft geometry that is selected for this study is a box-and-panel satellite modeled as a cube shaped bus with a long, slender panel attached. The bus width, height and depth are 3 m. The panel width is 3 m, depth is 0.2 m and height is 8.5 m. The panel is located on the top of the bus extending in the z-axis direction with one of its large faces coplanar with the positive y face of the bus. This model geometry is shown in Figure 1.7. This geometry is selected because it has significant variation from simple geometric shapes like cylinders and represents a more realistic target spacecraft. It also shows symmetry that can be used to impose additional constraints on the positions of the VMSM model spheres, and this symmetry is exploited to reduce the amount of data that is required for the optimization procedure.

A SMSM model of the box-and-panel is generated using MATLAB's *meshgrid* feature to create many rectangles which are translated and rotated to make the full spacecraft, and electric field data is generated using Eq. (1.5), at positions spread radially about the SMSM model. Sample points are generated using the golden spiral algorithm, which places equally spaced points on the surface of a sphere.[9] This radial spread of electric field data produces distributions of shells of data, which are easily selected or neglected, or reduced to hemispheres or octants for fitting, such as the one shown in Figure 1.7. Whole spherical shells of data are produced for the box-and-panel geometry; however, due to the symmetry of the model, the complete behavior of the electric field produced by the SMSM model can be captured in one hemisphere of data.

One, two and three-sphere VMSM reduced-coordinate models are created with this data using E-field matching and MATLAB's *fmincon* optimization algorithm. Various sets of data, including whole spheres, hemispheres and multiple shell sets, are used in the optimization processes. In addition, a three-sphere 4 degree-of-freedom VMSM model is generated using E-field matching and *fmincon*. Only shells with radii larger than 12 m are used for optimization to avoid overlap between sample points and SMSM spheres, which would invalidate Eq. (1.5). Like the cylinder model optimization process, the box-and-panel self-capacitance is calculated using Maxwell 3D and the self-capacitance constraints on the optimization processes are imposed numerically. Additional inequality constraints are imposed for the two and three-sphere VMSM models to ensure aesthetically pleasing models in which spheres do not overlap.

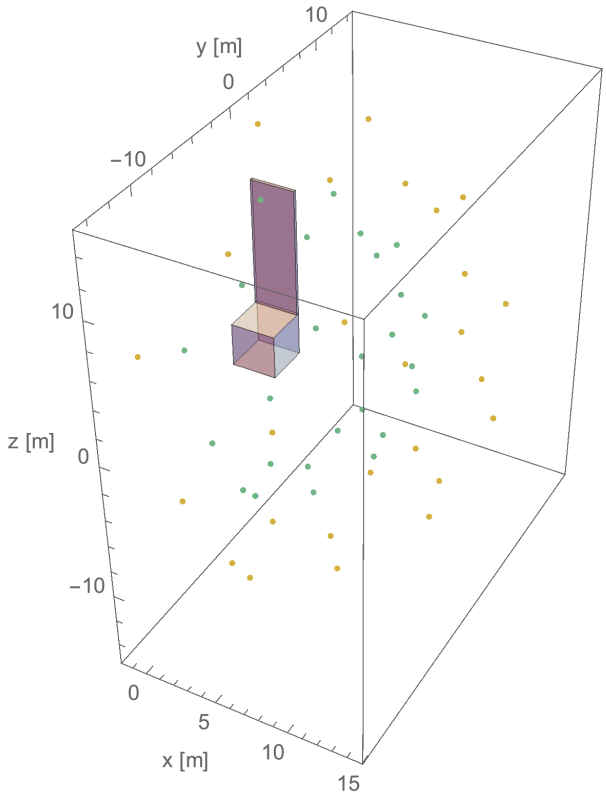

Figure 1.7: *Box-and-Panel Geometry with Data Point Distribution*

1.1.1.3 Cost Function Comparison

The cost function of Eq. (1.6) is compared with the proposed electric field cost function of Eq. (1.8) to compare their characteristics. Both cost functions are used to generate two-sphere VMSM models for a perfectly conducting cylinder charged to 30 kV. Maxwell 3D is used to determine a cylinder self-capacitance value of 106.8345 pF. Noting a potential singularity in Eq. (1.10) when r is one half C_{mod}, the cost function values, shown in Figures 1.8(a) and 1.8(b), along the intersection with the self-capacitance constraint surface are plotted against r for which ρ is positive. The force and torque cost function is evaluated across one quadrant and shell of FEM-generated force and torque predictions. The E-field cost function is evaluated across the same quadrant and shell, but using SMSM-generated E-field predictions.

The r values minimizing both cost functions are nearly identical, differing by only 0.2%. Investigating the cost function sensitivities near both minima suggests that force and torque errors are more sensitive to model parameters than E-field errors are. The proposed E-field cost function shows desirable characteristics, particularly for a local optimization algorithm like *fmincon*. It is generally smooth when compared with the force and torque cost function, and apart from a small region near the singularity in ρ, approaches its minimum unimpeded.

1.1.1.4 Constrained and Unconstrained Box-and-Panel VMSM Models

One, two and three-sphere box-and-panel VMSM models are generated with and without a self-capacitance constraint in order to determine the usefulness of the constraint when applied to an optimization problem without far-field data noise. Models are fit to data in three whole spherical

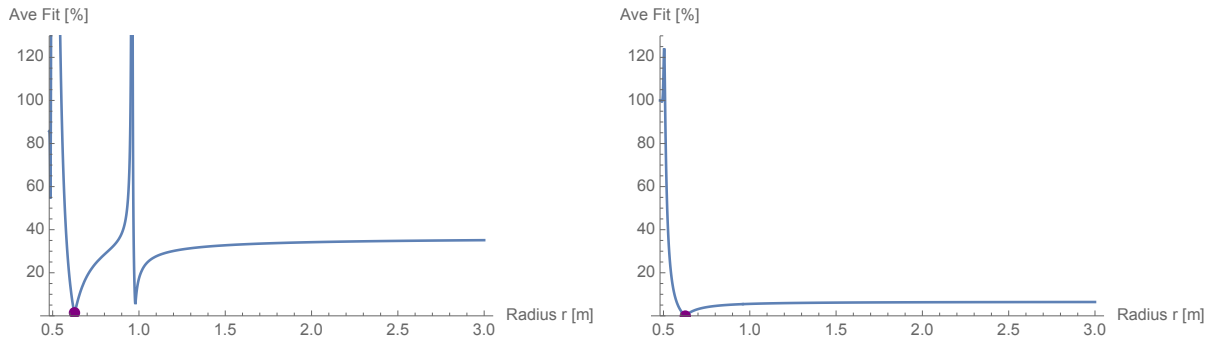

(a) Former Force and Torque Cost Function (b) New E-field Cost Function

Figure 1.8: *Force and Torque and E-Field Cost Functions for Cylinder Model.*

shells with radii of 15, 20 and 25 m. Symmetry of the box-and-panel geometry about the $y-z$ plane is used to reduce the $4N$ degree-of-freedom optimization problem to a $3N$ degree-of-freedom problem. Imposing a self-capacitance constraint reduces the degrees-of-freedom to $3N-1$. The model is charged to 30 kV. Maxwell 3D is once again used to calculate self-capacitance, and returns a value of 336.14 pF. Optimizer initial conditions are chosen loosely based on the box-and-panel geometry. A visualization the VMSM models of the box-and-panel geometry is included in Figure 1.9.

Tables 1.1-1.3 show the initial and final conditions for the one, two and three-sphere box-and-panel models, with and without the self-capacitance constraint.

Table 1.1: *Initial and Final States for One-Sphere VMSM Model Optimization, C- Constrained, NC- Non-Constrained*

	R_1 [m]	y_1 [m]	z_1 [m]
Initial	1.000	0.000	0.000
Final C	3.021	0.626	2.914
Final NC	2.951	0.608	2.785

Table 1.2: *Initial and Final States for Two-Sphere VMSM Model Optimization, C- Constrained, NC- Non-Constrained*

	R_1 [m]	R_2 [m]	y_1 [m]	z_1 [m]	y_2 [m]	z_2 [m]
Initial	1.000	1.000	0.000	0.000	1.400	6.000
Final C	2.202	1.458	0.135	0.210	1.596	8.183
Final NC	2.201	1.471	0.134	0.207	1.600	8.177

Table 1.3: *Initial and Final States for Three-Sphere VMSM Model Optimization, C- Constrained, NC- Non-Constrained*

	R_1 [m]	R_2 [m]	R_3 [m]	y_1 [m]	z_1 [m]	y_2 [m]	z_2 [m]	y_3 [m]	z_3 [m]
Initial	1.000	1.000	1.000	0.000	0.000	1.400	6.000	1.400	9.000
Final C	2.039	1.323	1.120	-0.008	-0.166	1.319	4.584	1.555	8.972
Final NC	2.041	1.322	1.119	-0.007	-0.163	1.321	4.612	1.556	8.974

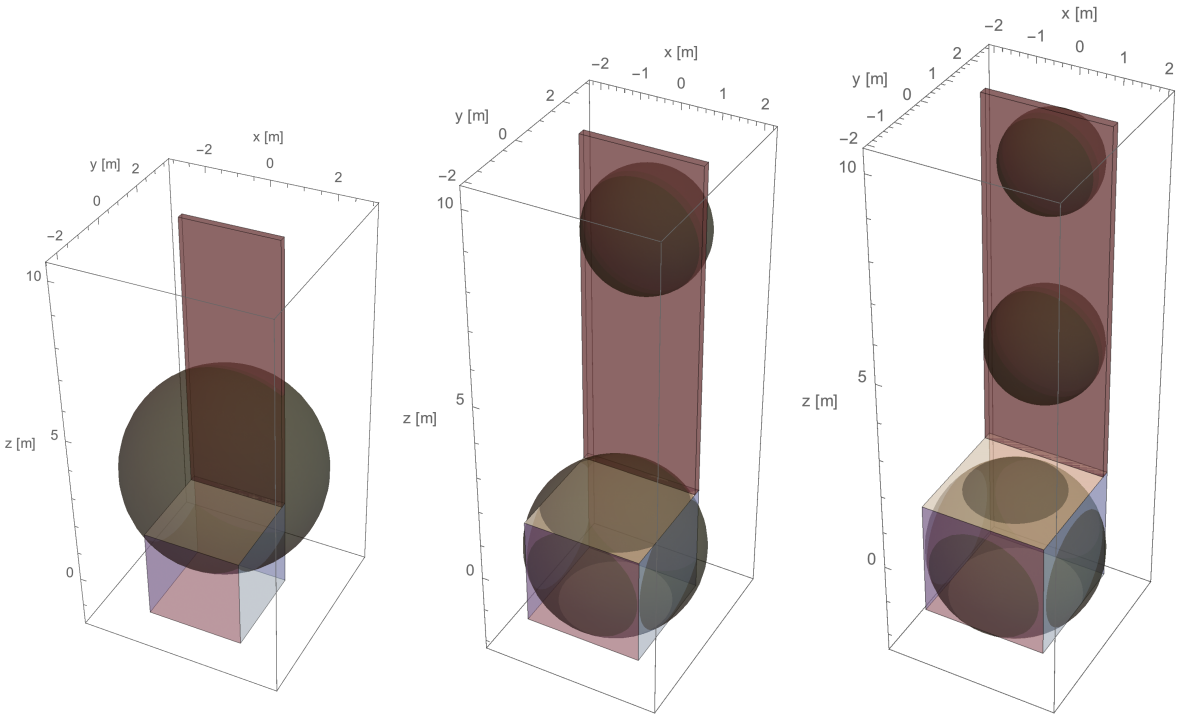

(a) One-Sphere Model (b) Two-Sphere Model (c) Three-Sphere Model

Figure 1.9: *Visualizations of VMSM Box-and-Panel Geometry Models Generated Using the E-Field Fitting Method*

Shell-averaged force and torque errors of the six VMSM models with respect to the SMSM generated data are shown in Figures 1.10(a) and 1.10(b), respectively. As can be seen, the self-capacitance constraint has utility even when far-field noise is not a concern. In particular, when generating a one-sphere model the self-capacitance constraint ensures that force errors far from the target geometry continue to decay as sample point radius is increased. The effect of the self-capacitance constraint is also dramatic for the two-sphere model. The force errors of the two and three-sphere models are nearly identical at 30 m from the target geometry when the constraint is imposed, whereas without it the two-sphere model model force errors remain significantly larger than the three-sphere model's. It is interesting to note that, as more spheres are added to the VMSM model, self-capacitance is matched automatically as displayed by the three-sphere force and torque errors. Both the constrained and non-constrained model errors overlap, and the optimal model parameters of each are nearly identical.

Another benefit of imposing the self-capacitance constraint is that it can significantly reduce computational effort. The number of function calls required to generate each of the six models is recorded. The results are shown in Figure 1.11. The results show that imposing the self-capacitance constraint consistently results in increased performance regardless of how many sphere are used to create the VMSM model. This performance increase is due to the reduced dimension of the search space when a self-capacitance constraint is enforced. Given the increased force and torque accuracy and decreased computation effort, the self-capacitance constraint should be enforced even when far-field noise is not a concern.

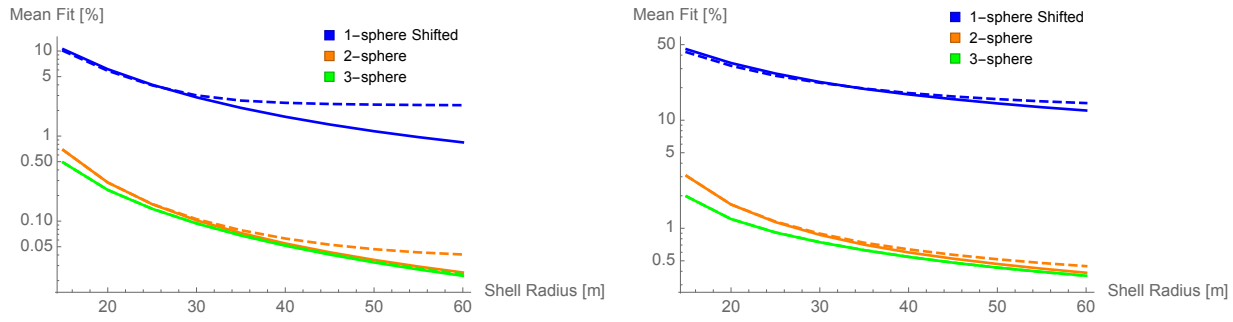

(a) Force Errors (b) Torque Errors

Figure 1.10: *One, Two and Three Sphere VMSM Model Force and Torque Errors with Respect to SMSM Force and Torque Predictions, (—) Constrained, (- -) Non-Constrained*

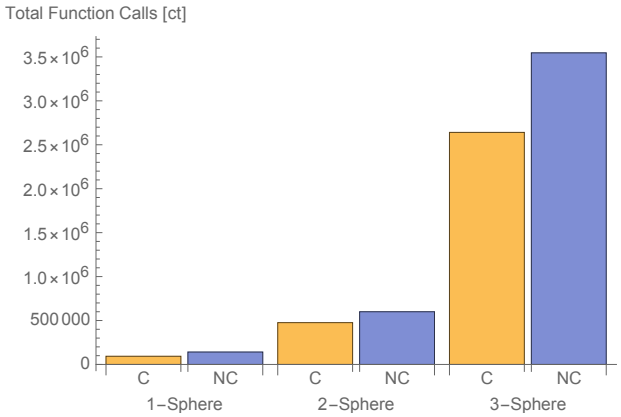

Figure 1.11: *Total Matlab Function Calls Required to Generate One, Two and Three-Sphere Box-and-Panel VMSM Models using E-Field Fitting*

1.1.1.5 Reduced-Shell Data Sets with Self-Capacitance Constraint

Since imposing a self-capacitance constraint forces force vectors in the far-field to automatically match, it is desired to investigate whether or not fewer numbers of shells with smaller radii can be used to effectively generate VMSM models. This question is interesting for two reasons: smaller data sets will reduce the amount of time required for optimization, and fitting to data closer to the target might increase near-field accuracy without significantly affecting accuracy at larger distances.

A three-sphere VMSM model is used to model the box-and-panel geometry. The VMSM model is fit to single shells at radii of 12, 14 and 15 m. The model voltage is set to 30 kV, and a self-capacitance constraint of 336.14 pF is imposed. The accuracy of these models are compared with each other and to the three-sphere constrained model generated using three whole shells. The resulting shell-averaged force, torque, and average error plots when compared with the SMSM model are shown in Figures 1.12(a)-1.12(c). These results show negligible differences in force and torque accuracy near the target, while the model fitted to the 12 m radius shell shows degraded accuracy far from the target. Accuracies of models fit to three whole shells and to 14 m and 15 m shell radii are nearly identical. The practical impact of the degraded accuracy for the model fitted to the 12 m shell is very small; however, for high accuracy at large distances from a target, a model should be fitted to at least one shell with a larger radius.

The performance impact of reducing the number of shells is analyzed by recording the number

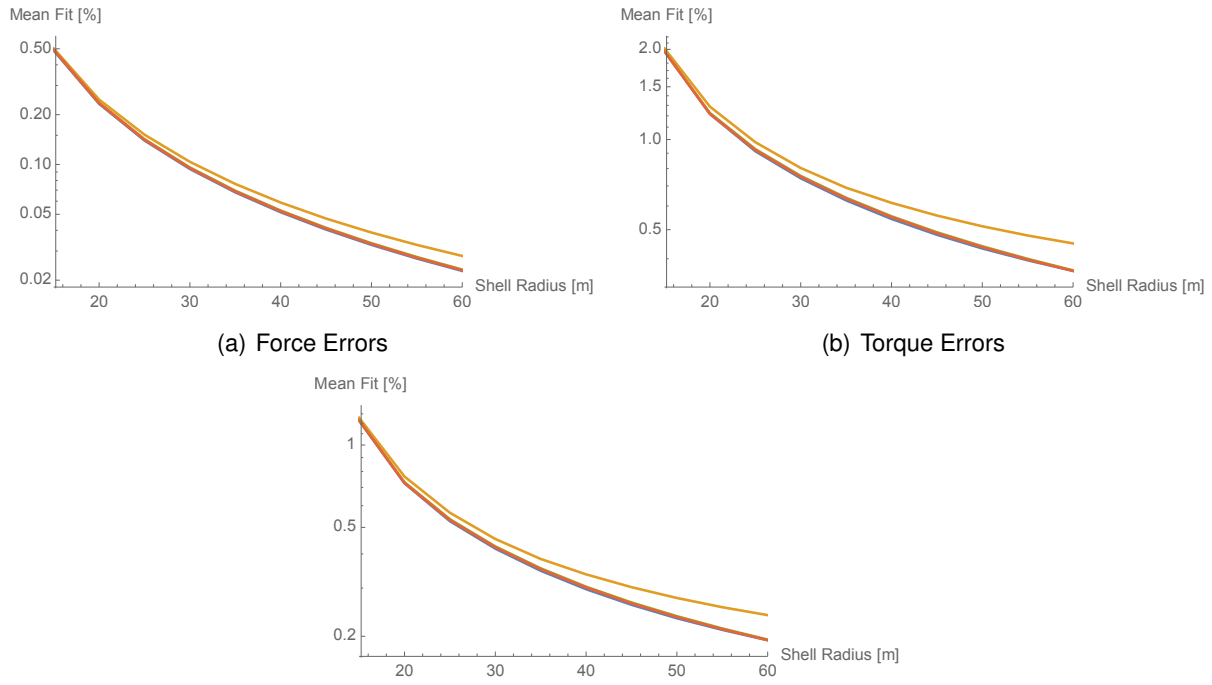

(a) Force Errors

(b) Torque Errors

(c) Average Errors

Figure 1.12: *Model Force, Torque and Average (Force and Torque) Errors of Three-Sphere Box-and-Panel VMSM Models Generated Using: (—) 3 Whole Shells, (—) 15 m Shell, (—) 14 m Shell, (—) 12 m Shell*

of *fmincon* iterations and total time required to generate each model. The results are shown in Figures 1.13(a) and 1.13(b). These results show that there is not necessarily a positive correlation between decreased numbers of data points and increased performance. Fitting to data points very close to the target geometry increases the number of iterations required to generate a model. In addition, the time required to generate a model is not solely dependent upon the number of data points. While it takes more time to generate a model using three whole shells of data when compared to one whole shell at a radius of 15 m, it takes approximately the same amount of time to generate a model using one whole shell with a radius of 12 m even though the number of *fmincon* iterations is 12% less. The competing interests of maintaining a self-capacitance constraint while fitting to electric field data near the target – which is far more variable than the same data at larger radii – is likely the reason for this phenomenon. Due to the increased error and decreased performance associated with fitting to shells very close to the target, it is recommended to fit models using shells at intermediate ranges. Doing so aids convergence of the optimizer, and the total time required to generate a model is decreased either because the number of iterations to convergence is decreased or because the total time required for one iteration of the optimizer is decreased, or both.

1.1.1.6 Modeling using General 4 Degree-of-Freedom MSM Spheres

Previous work focuses on simple geometries that have high levels of symmetry, like the cylinder model. For geometries like these, the number of MSM optimization parameters can be reduced significantly by specifying, for example, that the cylinder MSM spheres must lie on the symmetry axis. As geometric complexity increases, so does the effort required to find symmetries to exploit

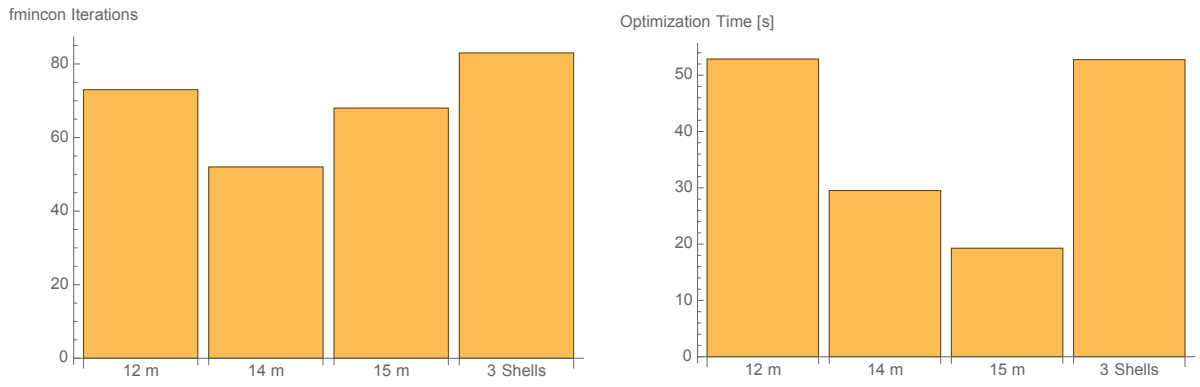

(a) *fmincon* Iterations (b) Total Model Generation Times

Figure 1.13: fmincon *Iterations and Total Model Generation Times Required to Generate Three Sphere VMSM Models Using E-Field Fitting and Shell Reduction for Various SMSM-Generated E-Field Data Sets*

Table 1.4: *Initial and Final States for Three-Sphere 4DOF VMSM Model Optimization*

	Initial	Final
R_1 [m]	1.000	2.051
R_2 [m]	1.000	1.299
R_3 [m]	1.000	1.106
x_1 [m]	0.000	-0.004
y_1 [m]	0.000	-0.004
z_1 [m]	0.000	-0.136
x_2 [m]	0.000	0.038
y_2 [m]	1.400	1.385
z_2 [m]	6.000	4.788
x_3 [m]	0.000	-0.028
y_3 [m]	1.400	1.534
z_3 [m]	9.000	8.993

and analytically parameterize them. Using general MSM 4 degree-of-freedom (4DOF) modeling allows each MSM sphere to have 3 location and one radius degree of freedom. This avoids the need to find symmetry and allows for optimization in a $4N$ dimension search space. Each parameter associated with a VMSM model sphere is found through optimization, and the up-front human-involvement cost of generating a model is reduced.

A three-sphere VMSM model of the box-and-panel geometry is generated using data in three whole shells with radii of 15, 20 and 25 m. A self-capacitance constraint is enforced using a value of 336.14 pF. The model voltage is set to 30 kV. The initial and final conditions for the 4DOF fitting problem are shown in Table 1.4.

The force and torque accuracy of the 4DOF model with respect to the box-and-panel SMSM model is compared to three-sphere 3DOF models using three whole shells and one half shell at 15 m in Figures 1.14(a) and 1.14(b). The model with the least accuracy is the 3DOF model fitted to one half shell of data. The 4DOF model's accuracy resembles the 3DOF model fitted to three whole shells. Since the optimizer knows nothing about the symmetry of the box-and-panel model, a whole shell of data must be used to generate an accurate model when 4DOF is used. Total *fmincon* iterations for each of the models shown in Figure 1.14 are shown in Table 1.5.

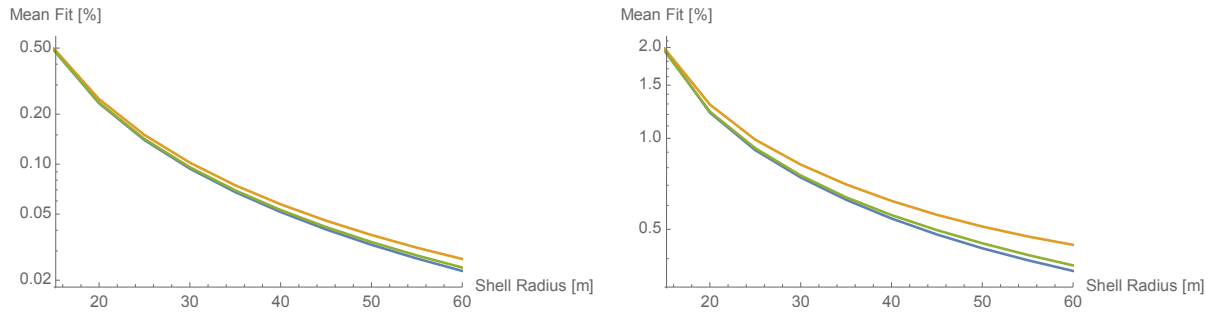

(a) Force Errors (b) Torque Errors

Figure 1.14: *4DOF Force and Torque Percent Relative Error Comparison to SMSM Force and Torque Predictions for: (—) Three-Sphere Model Three Whole Shells, (—) Three-Sphere Model One Half Shell, (—) Three-Sphere Model One Whole Shell (4DOF)*

Table 1.5: *Total Function Calls for 4DOF Model Comparison*

Model	Total *fmincon* Iterations
4DOF 3 Whole Shells	77
3DOF 3 Whole Shells	83
3DOF 1 Half Shell	132
3DOF 1 Whole Shell	68

Surprisingly, the 4DOF modeling method yields a converged result using only 58% of the iterations required for a 3DOF model using a half shell of data with the same radius. These results reiterate that the number of iterations required for convergence upon a useful model is far more dependent on using data at intermediate radii than on the number of data points used. However, when considering time required to generate a model, the 3DOF 1 half shell model is by far the most efficient to generate, requiring only about a third as much time as the three whole shell models. An interesting result is that the 4DOF model is generated in approximately the same amount of time as the 3DOF 3 whole shell model. These results show that 4DOF modeling using E-field fitting is promising from both an accuracy and performance perspective, and a 4DOF can be generated in approximately the same amount of time as a 3DOF model using the same number of data points at the same shell radii.

1.1.2 Appropriate Fidelity Models (AFMs)

1.1.2.1 Motivation for AFMs

The problem of two charged conductors interacting through electrostatics is similar to that of two bodies interacting gravitationally. The differential force in both cases is proportional to the product of either the masses or charges, and inversely proportional to the square of the distance between them. The gravitational problem can be readily solved using conic sections if both bodies are treated as point masses. For added fidelity, the larger body is treated as a general shape through the use of a spherical harmonic expansion. If both bodies are near the same size and very close, they must both be treated in a general manner solving the full gravitational two-body problem. This problem can be solved using a range of methods including expansions of mass distribution through MacCullagh's approximation,[10] inertia integrals[11] or numerically using a lumped-mass approach.[12] In the electrostatic problem, there is also an added complication: the total mass and its distribution

is fixed in a rigid body while the total charge and associated charge distribution change easily within a conductor. As the two conductors rotate and translate, the charge distribution changes and impacts the electrostatic forces and torques. For example, consider to negatively charged objects approaching each other. The electrons will repel each other and gather on the far sides of the objects, causing a differential charge distribution. In contrast, as two asteroids approach each other their mass distribution remain unchanged.

Many methods exist to solve the electrostatic problem numerically, and they all begin with prediction of the charge distribution. This can be done using full FEA software which is very accurate but much too slow for dynamics simulations, or more coarse methods like the Method of Moments.[13] Once the charge distribution is known, the total Coulomb force can be found by summing the force between every facet in one body and every facet in the other body. A new method for force and torque prediction is the Multi-Sphere Method (MSM),[3] which places spheres of tunable radii and position throughout the conductor. This process divides into Surface MSM (SMSM), which was optimized for large numbers of spheres constrained to be on the surface of the conductor by Stevenson et. al. in[2] and Volume MSM (VMSM), which uses a small number of spheres with unconstrained positions and was optimized by Chow et. al. in.[3,5] While these methods offer an excellent trade study between accuracy and speed, all are numerical and do not enable closed-form analysis. Analytical insight is instrumental in any dynamics and stability studies, such as for the de-spin and ET concept.

Analytical formula for the electrostatic two-body problem are found for the special case of two conducting spheres using the Method of Images.[7,8,14] If the bodies are not spherical, the multipole expansion method can be used to find the electric potential in the vicinity of a charge distribution by expanding the charge distribution in powers of $1/R$.[14] The potential energy of two charged molecules can also be found and differentiated with respect to position attitude to find force and torque.[15] These expansions use terms similar to the inertia integrals used by Hou.[11] The conference paper cited in Reference[16] introduces a similar method for finding the electrostatic force and torque between two charged spacecraft, but differs in that it does not find the potential but finds the force and torque directly. This method for predicting force and torque is called the Appropriate Fidelity Measures (AFM) method, named for the measures of the charge distribution that appear due to the appropriate fidelity truncation of the binomial series.

Reference[16] illustrates an early form of the AFM concept and investigates some special cases of an isolated body in a flat or radial field, but doesn't develop the full two body AFM theory. Flat field analysis was furthered for the special case of a High Area-to-Mass Ratio (HAMR) object's orbit being perturbed by Earth's magnetic field in Reference.[1] This report provides the first comprehensive theory of AFMs for general spacecraft applications, including the general case of two interacting charged bodies, and shows how the radial field is a special case of the general two body problem.[17] Providing a general formulation enables developing any particular AFM models that consider the local environmental electric and magnetic fields, as well as electric fields due to arbitrary neighboring charged spacecraft. This work differs from the multipole expansion cited in Reference[15] in that this work also presents a method for predicting the moments of the charge distribution from the voltage and attitude of each craft as well as their separation.

1.1.2.2 Problem Statement

This section establishes the notation and variables used in this paper, as well as the fundamental charging and force models employed and the key binomial expansion used. Consider two charged, conducting neighboring spacecraft as is shown in Figure 1.15 with a known charge distribution. This later assumption is relaxed later in the development to assume that only the potentials and

relative attitude and separation are known. They each experience a force and torque due to the other's charge. The force and torque on body 2 is found by integrating the differential force, which is a function of body 1's charge distribution, across body 2.

$$\mathrm{d}\boldsymbol{F}_2 = \frac{\mathrm{d}q_1 \mathrm{d}q_2 \boldsymbol{R}}{4\pi\epsilon_0 R^3} \tag{1.12}$$

where $\boldsymbol{R}$ points from $\mathrm{d}q_1$ to $\mathrm{d}q_2$. The separation vector is expressed from body vectors and a vector between the center of mass of each body $\boldsymbol{R} = \boldsymbol{R}_c + \boldsymbol{r}_2 - \boldsymbol{r}_1$. Using this substitution makes the differential force

$$\mathrm{d}\boldsymbol{F}_2 = \frac{\mathrm{d}q_1 \; \mathrm{d}q_2 \; \boldsymbol{R}_c + \boldsymbol{r}_2 - \boldsymbol{r}_1}{4\pi\epsilon_0 \; ||\boldsymbol{R}_c + \boldsymbol{r}_2 - \boldsymbol{r}_1||^3} \tag{1.13}$$

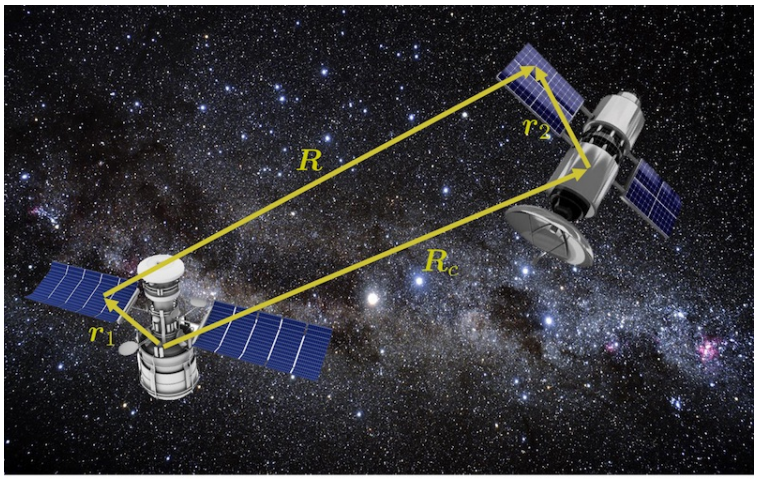

Figure 1.15: *Coordinate system for inter-craft derivation*

Where ϵ_0 is the permittivity of free space, $\epsilon_0 \approx 8.854187 * 10^{-12}$ F/m. The differential force is approximated by binomially expanding the denominator and truncating higher-order terms on the assumption that the body radii ($\boldsymbol{r}_1$ and $\boldsymbol{r}_2$) are small compared to their separation ($\boldsymbol{R}_c$).

$$\frac{1}{||\boldsymbol{R}_c + \boldsymbol{r}_2 - \boldsymbol{r}_1||^3} = (R_c^2 + r_1^2 + r_2^2 + 2(\boldsymbol{R}_c \cdot \boldsymbol{r}_2 - \boldsymbol{R}_c \cdot \boldsymbol{r}_1 - \boldsymbol{r}_2 \cdot \boldsymbol{r}_1))^{-3/2} \tag{1.14}$$

$$= \frac{1}{R_c^3}\left[1 + \left(\frac{r_2^2}{R_c^2} + \frac{r_1^2}{R_c^2} + \frac{2}{R_c^2}(\boldsymbol{R}_c \cdot \boldsymbol{r}_2 - \boldsymbol{R}_c \cdot \boldsymbol{r}_1 - \boldsymbol{r}_2 \cdot \boldsymbol{r}_1)\right)\right]^{-3/2} \tag{1.15}$$

Expand the denominator to second order using a binomial series $(1+x)^{-3/2} \approx 1 - \frac{3}{2}x + \frac{15}{8}x^2$ and reassemble to approximate the differential force as:

$$\mathrm{d}\boldsymbol{F}_2 = \frac{\mathrm{d}q_1 \; \mathrm{d}q_2}{4\pi\epsilon_0 R_c^3}(\boldsymbol{R}_c + \boldsymbol{r}_2 - \boldsymbol{r}_1)\Bigg(1 - \frac{3r_1^2}{2R_c^2} - \frac{3r_2^2}{2R_c^2} - \frac{3(\boldsymbol{R}_c \cdot \boldsymbol{r}_2 - \boldsymbol{R}_c \cdot \boldsymbol{r}_1 - \boldsymbol{r}_2 \cdot \boldsymbol{r}_1)}{R_c^2} + \frac{15((\boldsymbol{R}_c \cdot \boldsymbol{r}_2)^2 + (\boldsymbol{R}_c \cdot \boldsymbol{r}_1)^2 - (\boldsymbol{R}_c \cdot \boldsymbol{r}_1)(\boldsymbol{R}_c \cdot \boldsymbol{r}_2))}{2R_c^4}\Bigg) \tag{1.16}$$

This differential is integrated over the entire body to obtain the net electrostatic force on this object, or crossed with the body position vector and integrated over the body to obtain torque.

1.1.2.3 Appropriate Fidelity Measures

1.1.2.3.1 Fundamental AFM Expansion Terms Definition

The problem of two charged bodies interacting through electrostatics is similar to two massive bodies interacting through gravity. Just as moments of the mass distribution play a key role in solving the gravitational two-body problem,[11] moments of the charge distribution play a key role in predicting electrostatic force and torque. Three especially important moments of the charge distribution are identified and named here:

$$Q = \int_B \mathrm{d}q \qquad \boldsymbol{q} = \int_B \boldsymbol{r}\,\mathrm{d}q \qquad [Q] = \int_B -[\tilde{\boldsymbol{r}}][\tilde{\boldsymbol{r}}]\,\mathrm{d}q \tag{1.17}$$

Q is a scalar and is the total charge, $\boldsymbol{q}$ is a 3×1 vector and is defined as the dipole moment, and $[Q]$ is a 3×3 tensor defined as the charge tensor. The vector $\boldsymbol{r}$ points from the center of mass to the differential charge $\mathrm{d}q$, and $[\tilde{\boldsymbol{r}}]$ is the matrix form of the vector cross product: $\boldsymbol{a} \times \boldsymbol{b} = [\tilde{\boldsymbol{a}}]\boldsymbol{b}$. If the gravity analogy is used, the total charge Q is similar to the total mass, the dipole moment $\boldsymbol{q}$ is similar to the total mass multiplied by the offset between the center of a coordinate system and the true center of mass, and the charge tensor $[Q]$ is similar to the inertia tensor. The dipole moment $\boldsymbol{q}$ provides a measure of where the center of charge is in relation to the center of mass. If $\boldsymbol{q}$ is zero, then the center of charge and mass locations are identical. To relate these AFM terms to the variables commonly used in multipole expansions, Q and $\boldsymbol{q}$ are the mono and dipole terms, and the charge tensor $[Q]$ defined here is related to the quadrupole $[Q_p]$ by $[Q_p] = -3[Q] + 2\mathrm{tr}([Q])$.[14]

1.1.2.3.2 Inter-Craft Electrostatic Reactions

This section derives the force and torque on body 2 due the charge on body 1 and 2. This is done using the 2nd order binomial expansion for the denominator of the differential force.

1.1.2.3.2.1 Force Derivation

The total force on body 2 is found by integrating the differential force over the entire body

$$\boldsymbol{F}_2 = \frac{1}{4\pi\epsilon_0 R_c^3}\int_{B_1}\int_{B_2}(\boldsymbol{R}_c + \boldsymbol{r}_2 - \boldsymbol{r}_1)\Bigg(1 - \frac{3r_1^2}{2R_c^2} - \frac{3r_2^2}{2R_c^2} - \frac{3(\boldsymbol{R}_c\cdot\boldsymbol{r}_2 - \boldsymbol{R}_c\cdot\boldsymbol{r}_1 - \boldsymbol{r}_2\cdot\boldsymbol{r}_1)}{R_c^2} + \frac{15((\boldsymbol{R}_c\cdot\boldsymbol{r}_2)^2 + (\boldsymbol{R}_c\cdot\boldsymbol{r}_1)^2 - (\boldsymbol{R}_c\cdot\boldsymbol{r}_1)(\boldsymbol{R}_c\cdot\boldsymbol{r}_2))}{2R_c^4}\Bigg)\mathrm{d}q_2\mathrm{d}q_1 \tag{1.18}$$

This equation is broken into three parts: the terms resulting from the $\boldsymbol{R}_c, \boldsymbol{r}_1,$ and $\boldsymbol{r}_2$ which are denotes as $\boldsymbol{F}_{2_0}, \boldsymbol{F}_{2_1}$ and $\boldsymbol{F}_{2_2}$, respectively. The first term $\boldsymbol{F}_{2_0}$ is expressed as

$$\begin{aligned}\boldsymbol{F}_{2_0} =& \frac{\boldsymbol{R}_c}{4\pi\epsilon_0 R_c^3}\int_{B_1}\int_{B_2}\left(1-\frac{3r_1^2}{2R_c^2}-\frac{3r_2^2}{2R_c^2}-\frac{3(\boldsymbol{R}_c\cdot\boldsymbol{r}_2-\boldsymbol{R}_c\cdot\boldsymbol{r}_1-\boldsymbol{r}_2\cdot\boldsymbol{r}_1)}{R_c^2}+\right.\\ &\left.\frac{15((\boldsymbol{R}_c\cdot\boldsymbol{r}_2)^2+(\boldsymbol{R}_c\cdot\boldsymbol{r}_1)^2-(\boldsymbol{R}_c\cdot\boldsymbol{r}_1)(\boldsymbol{R}_c\cdot\boldsymbol{r}_2))}{2R_c^4}\right)\mathrm{d}q_2\mathrm{d}q_1\\ =& \frac{\boldsymbol{R}_c}{4\pi\epsilon_0 R_c^3}\left[Q_1Q_2-\left(\frac{3}{2R_c^2}\int_{B_1}r_1^2\,\mathrm{d}q_1\int_{B_2}\mathrm{d}q_2\right)-\left(\frac{3}{2R_c^2}\int_{B_2}r_2^2\,\mathrm{d}q_2\int_{B_1}\mathrm{d}q_1\right)\right.\\ &-\left(\frac{3}{R_c^2}\boldsymbol{R}_c\cdot\int_{B_1}\mathrm{d}q_1\int_{B_2}\boldsymbol{r}_2\mathrm{d}q_2\right)+\left(\frac{3}{R_c^2}\boldsymbol{R}_c\cdot\int_{B_2}\mathrm{d}q_2\int_{B_1}\boldsymbol{r}_1\mathrm{d}q_1\right)\\ &+\left(\frac{3}{R_c^2}\int_{B_1}\boldsymbol{r}_1\mathrm{d}q_2\int_{B_2}\boldsymbol{r}_2\mathrm{d}q_2\right)+\left(\frac{15}{2R_c^4}\int_{B_1}\mathrm{d}q_1\int_{B_2}(\boldsymbol{R}_c\cdot\boldsymbol{r}_2)^2\mathrm{d}q_2\right)\\ &\left.+\left(\frac{15}{2R_c^4}\int_{B_2}\mathrm{d}q_2\int_{B_1}(\boldsymbol{R}_c\cdot\boldsymbol{r}_1)^2\mathrm{d}q_1\right)-\left(\frac{15}{2R_c^4}\int_{B_2}(\boldsymbol{R}_c\cdot\boldsymbol{r}_2)\mathrm{d}q_2\int_{B_1}(\boldsymbol{R}_c\cdot\boldsymbol{r}_1)\mathrm{d}q_1\right)\right]\end{aligned} \tag{1.19}$$

Here the moments of the charge distribution given in Eq. 1.17 are used to simplify the equations. Using the identity $\int r^2\mathrm{d}q = \mathrm{tr}([Q])/2$ to simplify the above equation yields:

$$\begin{aligned}\boldsymbol{F}_{2_0} = \frac{\boldsymbol{R}_c}{4\pi\epsilon_0 R_c^3}\Bigg[&Q_1Q_2-\frac{3Q_2}{4R_c^2}\mathrm{tr}([Q_1])-\frac{3Q_1}{4R_c^2}\mathrm{tr}([Q_2])-\frac{3Q_1}{R_c^2}\boldsymbol{R}_c\cdot\boldsymbol{q}_2\\ &+\frac{3Q_2}{R_c^2}\boldsymbol{R}_c\cdot\boldsymbol{q}_1+\frac{3Q_2}{R_c^2}\boldsymbol{q}_2\cdot\boldsymbol{q}_1+\frac{15Q_1}{2R_c^4}\int_{B_2}(\boldsymbol{R}_c\cdot\boldsymbol{r}_2)^2\mathrm{d}q_2\\ &+\frac{15Q_2}{2R_c^4}\int_{B_1}(\boldsymbol{R}_c\cdot\boldsymbol{r}_1)^2\mathrm{d}q_1-\frac{15}{2R_c^4}(\boldsymbol{R}_c\cdot\boldsymbol{q}_2)(\boldsymbol{R}_c\cdot\boldsymbol{q}_1)\Bigg)\Bigg]\end{aligned} \tag{1.20}$$

To solve the two remaining integrals, apply the vector identity $(\boldsymbol{a}\cdot\boldsymbol{b})\boldsymbol{b} = ([\tilde{\boldsymbol{b}}][\tilde{\boldsymbol{b}}]+b^2[I])\boldsymbol{a}$ to the terms of the form $(\boldsymbol{R}_c\cdot\boldsymbol{r})^2$ and integrate to yield

$$\boldsymbol{R}_c\cdot(\boldsymbol{R}_c\cdot\boldsymbol{r})\boldsymbol{r} = \boldsymbol{R}_c\cdot([\tilde{\boldsymbol{r}}][\tilde{\boldsymbol{r}}]+r^2[I])\boldsymbol{R}_c = \boldsymbol{R}_c^T[\tilde{\boldsymbol{r}}][\tilde{\boldsymbol{r}}]\boldsymbol{R}_c + R_c^2r^2 \tag{1.21}$$

$$\rightarrow -\boldsymbol{R}_c^T[Q]\boldsymbol{R}_c + R_c^2\mathrm{tr}([Q])/2 \tag{1.22}$$

and re-write $\boldsymbol{F}_{2_0}$ finally as:

$$\begin{aligned}\boldsymbol{F}_{2_0} = \frac{\boldsymbol{R}_c}{4\pi\epsilon_0 R_c^3}\Bigg[&Q_1Q_2+\frac{3Q_2}{R_c^2}\mathrm{tr}([Q_1])+\frac{3Q_1}{R_c^2}\mathrm{tr}([Q_2])-\frac{3Q_1}{R_c^2}\boldsymbol{R}_c\cdot\boldsymbol{q}_2+\frac{3Q_2}{R_c^2}\boldsymbol{R}_c\cdot\boldsymbol{q}_1\\ &+\frac{3Q_2}{R_c^2}\boldsymbol{q}_2\cdot\boldsymbol{q}_1-\frac{15Q_1}{2R_c^4}\boldsymbol{R}_c^T[Q_2]\boldsymbol{R}_c-\frac{15Q_2}{2R_c^4}\boldsymbol{R}_c^T[Q_1]\boldsymbol{R}_c-\frac{15}{R_c^4}(\boldsymbol{R}_c\cdot\boldsymbol{q}_2)(\boldsymbol{R}_c\cdot\boldsymbol{q}_1)\Bigg]\end{aligned} \tag{1.23}$$

The second part of the force $\boldsymbol{F}_{2_1}$ is much simpler because many of the terms become third order and are neglected in this second order expansion.

$$\boldsymbol{F}_{2_1} = \frac{1}{4\pi\epsilon_0 R_c^3}\int_{B_1}\int_{B_2}\boldsymbol{r}_2\left(1-\frac{3(\boldsymbol{R}_c\cdot\boldsymbol{r}_2-\boldsymbol{R}_c\cdot\boldsymbol{r}_1)}{R_c^2}\right)\mathrm{d}q_2\mathrm{d}q_1 \tag{1.24}$$

$$= \frac{1}{4\pi\epsilon_0 R_c^3}\left[Q_1\boldsymbol{q}_2+\frac{3Q_1}{R_c^2}[Q_2]\boldsymbol{R}_c-\frac{3Q_1}{2R_c^2}\mathrm{tr}([Q_2])\boldsymbol{R}_c+\frac{3(\boldsymbol{R}_c\cdot\boldsymbol{q}_1)}{R_c^2}\boldsymbol{q}_2\right] \tag{1.25}$$

The third part of the force $\boldsymbol{F}_{2_2}$ is similar in form to $\boldsymbol{F}_{2_1}$ with the $\boldsymbol{r}_2$ being replaced with a $-\boldsymbol{r}_1$.

$$\boldsymbol{F}_{2_2} = \frac{1}{4\pi\epsilon_0 R_c^3}\int_{B_1}\int_{B_2} -\boldsymbol{r}_1\left(1-\frac{3(\boldsymbol{R}_c\cdot\boldsymbol{r}_2-\boldsymbol{R}_c\cdot\boldsymbol{r}_1)}{R_c^2}\right)\mathrm{d}q_2\mathrm{d}q_1 \tag{1.26}$$

$$= \frac{1}{4\pi\epsilon_0 R_c^3}\left[-Q_2\boldsymbol{q}_1+\frac{3Q_2}{R_c^2}[Q_1]\boldsymbol{R}_c-\frac{3Q_2}{2R_c^2}\mathsf{tr}([Q_1])\boldsymbol{R}_c+\frac{3(\boldsymbol{R}_c\cdot\boldsymbol{q}_2)}{R_c^2}\boldsymbol{q}_1\right] \tag{1.27}$$

The total force is then expressed as

$$\begin{aligned}\boldsymbol{F}_2 = \frac{1}{4\pi\epsilon_0 R_c^3}\Bigg[&\Bigg(Q_1Q_2+\frac{3Q_2}{2R_c^2}\mathsf{tr}([Q_1])+\frac{3Q_1}{2R_c^2}\mathsf{tr}([Q_2])-\frac{3Q_1}{R_c^2}\boldsymbol{R}_c\cdot\boldsymbol{q}_2+\frac{3Q_2}{R_c^2}\boldsymbol{R}_c\cdot\boldsymbol{q}_1+\frac{3Q_2}{R_c^2}\boldsymbol{q}_2\cdot\boldsymbol{q}_1\\ &-\frac{15Q_1}{2R_c^4}\boldsymbol{R}_c^T[Q_2]\boldsymbol{R}_c-\frac{15Q_2}{2R_c^4}\boldsymbol{R}_c^T[Q_1]\boldsymbol{R}_c-\frac{15}{R_c^4}(\boldsymbol{R}_c\cdot\boldsymbol{q}_2)(\boldsymbol{R}_c\cdot\boldsymbol{q}_1)\Bigg)\boldsymbol{R}_c\\ &+Q_1\boldsymbol{q}_2+\frac{3Q_1}{R_c^2}[Q_2]\boldsymbol{R}_c+\frac{3(\boldsymbol{R}_c\cdot\boldsymbol{q}_1)}{R_c^2}\boldsymbol{q}_2-Q_2\boldsymbol{q}_1+\frac{3Q_2}{R_c^2}[Q_1]\boldsymbol{R}_c+\frac{3(\boldsymbol{R}_c\cdot\boldsymbol{q}_2)}{R_c^2}\boldsymbol{q}_1\Bigg]\end{aligned} \tag{1.28}$$

This equation is visualized in Table 1.6, where the common factor of $4\pi\epsilon_0 R_c^3$ is omitted, allowing easy ordering of terms based on which measures $(Q, \boldsymbol{q}, [Q])$ they incorporate. They are also ordered by the dimensionless ratio r/R_c where r is a characteristic dimension of either spacecraft. As the spacecraft move farther and farther away, the higher order terms in this variable matter less and less. The zeroth order term is in the upper left, the two boxes with two terms each are the first order terms, and the three boxes containing twelve terms along the diagonal are the second order terms. This table allows easy selection of the force terms needed for appropriate fidelity.

Table 1.6: *Force ordering matrix*

	Q_1	$\boldsymbol{q}_1$	$[Q_1]$
Q_2	$Q_1Q_2\boldsymbol{R}_c$	$\frac{3Q_2}{R_c^2}(\boldsymbol{R}_c\cdot\boldsymbol{q}_1)\boldsymbol{R}_c-Q_2\boldsymbol{q}_1$	$\frac{3Q_2}{2R_c^2}\mathsf{tr}([Q_1])\boldsymbol{R}_c$ $-\frac{15Q_2}{2R_c^4}(\boldsymbol{R}_c^T[Q_1]\boldsymbol{R}_c)\boldsymbol{R}_c$ $+\frac{3Q_2}{R_c^2}[Q_1]\boldsymbol{R}_c$
$\boldsymbol{q}_2$	$Q_1\boldsymbol{q}_2-\frac{3Q_1}{R_c^2}(\boldsymbol{R}_c\cdot\boldsymbol{q}_2)\boldsymbol{R}_c$	$\frac{3}{R_c^2}(\boldsymbol{q}_2\cdot\boldsymbol{q}_1)\boldsymbol{R}_c$ $-\frac{15}{R_c^4}(\boldsymbol{R}_c\cdot\boldsymbol{q}_2)(\boldsymbol{R}_c\cdot\boldsymbol{q}_1)\boldsymbol{R}_c$ $+\frac{3(\boldsymbol{R}_c\cdot\boldsymbol{q}_1)}{R_c^2}\boldsymbol{q}_2+\frac{3(\boldsymbol{R}_c\cdot\boldsymbol{q}_2)}{R_c^2}\boldsymbol{q}_1$	
$[Q_2]$	$\frac{3Q_1}{2R_c^2}\mathsf{tr}([Q_2])\boldsymbol{R}_c$ $-\frac{15Q_1}{2R_c^4}(\boldsymbol{R}_c^T[Q_2]\boldsymbol{R}_c)\boldsymbol{R}_c$ $+\frac{3Q_1}{R_c^2}[Q_2]\boldsymbol{R}_c$		

As might be expected, the force expression is symmetric, if one changes the sign on all $\boldsymbol{R}_c$ terms and switches the subscripts the force on body 1 is found to be equal in magnitude but opposite in direction to the force on body 2. This satisfies Newton's 3rd law.

1.1.2.3.2.2 Torque Derivation

The torque on body 2 is given by $\boldsymbol{T}_2 = \int_{B_1}\int_{B_2}\boldsymbol{r}_2\times\mathrm{d}\boldsymbol{F}$, where the same binomial expansion as before is used to approximate $\mathrm{d}\boldsymbol{F}$ to second order.

$$\boldsymbol{T}_2 = \frac{1}{4\pi\epsilon_0 R_c^3}\int_{B_1}\int_{B_2} \boldsymbol{r}_2 \times (\boldsymbol{R}_c + \boldsymbol{r}_2 - \boldsymbol{r}_1)\left(1 - \frac{3(\boldsymbol{R}_c\cdot\boldsymbol{r}_2 - \boldsymbol{R}_c\cdot\boldsymbol{r}_1)}{R_c^2}\right)\mathrm{d}q_2\mathrm{d}q_1 \quad (1.29)$$

Because of the extra $\boldsymbol{r}_2$, many of the terms in the differential force expansion become third order and are neglected. The differential torque has three parts corresponding to the $\boldsymbol{r}_2\times\boldsymbol{R}_c, \boldsymbol{r}_2\times\boldsymbol{r}_2$ and $\boldsymbol{r}_2\times\boldsymbol{r}_1$ components. The middle term is zero and the first and third are labeled by $\boldsymbol{T}_{2_0}$ and $\boldsymbol{T}_{2_1}$, respectivley. $\boldsymbol{T}_{2_0}$ is evaluated first:

$$\boldsymbol{T}_{2_0} = \frac{1}{4\pi\epsilon_0 R_c^3}\int_{B_1}\int_{B_2} \boldsymbol{r}_2\times\boldsymbol{R}_c\left(1 - \frac{3(\boldsymbol{R}_c\cdot\boldsymbol{r}_2 - \boldsymbol{R}_c\cdot\boldsymbol{r}_1)}{R_c^2}\right)\mathrm{d}q_2\mathrm{d}q_1 \quad (1.30)$$

$$= -\frac{1}{4\pi\epsilon_0 R_c^3}\boldsymbol{R}_c\times\int_{B_1}\int_{B_2} \boldsymbol{r}_2\left(1 - \frac{3(\boldsymbol{R}_c\cdot\boldsymbol{r}_2 - \boldsymbol{R}_c\cdot\boldsymbol{r}_1)}{R_c^2}\right)\mathrm{d}q_2\mathrm{d}q_1 \quad (1.31)$$

Where higher order terms in the binomial expansion are neglected. The integral is identical to the force integral in Eq.(1.24) evaluated earlier, and is written down from inspection as:

$$\boldsymbol{T}_{2_0} = -\boldsymbol{R}_c\times\left[\frac{Q_1\boldsymbol{q}_2}{R_c^3} + \frac{3(\boldsymbol{R}_c\cdot\boldsymbol{q}_1)\boldsymbol{q}_2}{R_c^5} + \frac{3Q_1[Q_2]\boldsymbol{R}_c}{R_c^5}\right] \quad (1.32)$$

The other part of the torque comes from the $\boldsymbol{r}_1$ and is evaluated below:

$$\boldsymbol{T}_{2_1} = -\frac{1}{4\pi\epsilon_0 R_c^3}\int_{B_1}\int_{B_2} (\boldsymbol{r}_2\times\boldsymbol{r}_1)\mathrm{d}q_2\mathrm{d}q_1 \quad (1.33)$$

The binomial expansion here is truncated to just the first term because the $\boldsymbol{r}_2\times\boldsymbol{r}_1$ term is already second order. This gives

$$\boldsymbol{T}_{2_1} = -\frac{1}{4\pi\epsilon_0 R_c^3}\boldsymbol{q}_2\times\boldsymbol{q}_1 \quad (1.34)$$

The total torque is found by summing $\boldsymbol{T}_{2_0}$ and $\boldsymbol{T}_{2_1}$ to yield

$$\boldsymbol{T}_2 = \frac{1}{4\pi\epsilon_0 R_c^3}\left[Q_1\boldsymbol{q}_2\times\boldsymbol{R}_c + \frac{3(\boldsymbol{R}_c\cdot\boldsymbol{q}_1)\boldsymbol{q}_2\times\boldsymbol{R}_c}{R_c^2} - \frac{3Q_1\boldsymbol{R}_c\times[Q_2]\boldsymbol{R}_c}{R_c^2} + (\boldsymbol{q}_1\times\boldsymbol{q}_2)\right] \quad (1.35)$$

This equation is visualized in Table 1.7 which follows Table 1.6 in omitting the factor of $4\pi\epsilon_0 R_c^3$ and grouping terms by their order in the dimensionless ratio r/R_c. Terms closer to the upper left corner are lower order.

Table 1.7: *Torque ordering matrix*

	Q_1	$\boldsymbol{q}_1$	$[Q_1]$
Q_2			
$\boldsymbol{q}_2$	$Q_1\boldsymbol{q}_2\times\boldsymbol{R}_c$	$\frac{3}{R_c^2}(\boldsymbol{R}_c\cdot\boldsymbol{q}_1)\boldsymbol{q}_2\times\boldsymbol{R}_c + (\boldsymbol{q}_1\times\boldsymbol{q}_2)$	
$[Q_2]$	$-\frac{3}{R_c^2}Q_1\boldsymbol{R}_c\times[Q_2]\boldsymbol{R}_c$		

As expected, there are no zeroth order terms, in fact there are no terms at all corresponding to the scalar charge Q_2. Unlike the force expansion, the torque is not symmetric, i.e. $\boldsymbol{T}_1 \neq -\boldsymbol{T}_2$. This is because the torque on body 1 and body 2 are not measured about the same point, but rather the center of mass of each body. If all torques are measured about the same point, such as the barycenter of the system, the torques are equal and opposite and cancel out and are not able to change the angular momentum of the system.

1.1.2.3.3 Radial Electrostatic Field Simplification

In Reference 16, the force and torque on a charged body are found by assuming a differential force of

$$\mathrm{d}\boldsymbol{F}_2 = \frac{Q_1 \mathrm{d}q_2}{4\pi\epsilon_0 R^3}\boldsymbol{R} \tag{1.36}$$

and integrating over body 2. Rather than repeating this integration, the first column of the force and torque ordering tables can be added to produce force and torque because that column only considers the scalar charge of body 1. This yields

$$\begin{aligned}\boldsymbol{F}_2 = \frac{Q_1}{4\pi\epsilon_0 R_c^3}\Big[&Q_2\boldsymbol{R}_c + \boldsymbol{q}_2 - \frac{3(\boldsymbol{q}\cdot\boldsymbol{R}_c)}{R_c^2}\boldsymbol{R}_c + \frac{3[Q_2]\boldsymbol{R}_c}{R_c^2} + \frac{3\boldsymbol{R}_c}{2R_c^2}\mathrm{tr}([Q_2]) \\ &- \frac{15}{2R_c^4}(\boldsymbol{R}_c^T[Q_2]\boldsymbol{R}_c)\boldsymbol{R}_c\Big]\end{aligned} \tag{1.37}$$

$$\boldsymbol{L}_2 = \frac{Q_1}{4\pi\epsilon_0 R_c^3}\Big[\boldsymbol{q}_2 + \frac{3}{R_c^2}[Q_2]\boldsymbol{R}_c\Big] \times \boldsymbol{R}_c \tag{1.38}$$

which agrees with the derivation done with the point charge differential force. This shows how force and torque in a radial field is a special case of the general two body problem. This is similar to how in most treatments a satellite is treated as a point mass while the earth is treated as a general body using spherical harmonics.

1.1.2.3.4 Flat Electrostatic Field Simplification

It is also of interest to calculate the force and torque on charged conducting bodies due to ambient flat electric and magnetic fields.[1] The differential force on a differential charge moving at $\boldsymbol{v}$ subject to $\boldsymbol{E}$ and $\boldsymbol{B}$ fields is given in Reference 18 as:

$$\mathrm{d}\boldsymbol{F} = \mathrm{d}q(\boldsymbol{E} + \boldsymbol{v}\times\boldsymbol{B}) \tag{1.39}$$

This differential force only varies significantly across a body if it is rotating very quickly near the geostationary point. The velocity is the orbital velocity $\boldsymbol{v_o}$ plus the transport velocity: $\boldsymbol{\omega}_{\mathcal{B}/\mathcal{E}}\times\boldsymbol{r}$,[19] where $\boldsymbol{\omega}_{\mathcal{B}/\mathcal{E}}$ is the angular velocity between the satellite body frame $\mathcal{B}$ and the magnetic field frame $\mathcal{E}$. For a spacecraft with $r = 1$ m, $\omega_{\mathcal{B}/\mathcal{E}} = 1$ deg/sec, and an ECEF orbital velocity of 1 km/sec, the ratio of the transport velocity to the orbital velocity will be less than 10^{-5}. In many scenarios the transport term can be dropped. The force is then:

$$\boldsymbol{F} = \int_B (\boldsymbol{E} + \boldsymbol{v}_o\times\boldsymbol{B})\mathrm{d}q = Q(\boldsymbol{E} + \boldsymbol{v}_o\times\boldsymbol{B}) \tag{1.40}$$

and the torque is

$$\boldsymbol{L} = \int_B \boldsymbol{r}\times(\boldsymbol{E} + \boldsymbol{v}_o\times\boldsymbol{B})\mathrm{d}q = (\boldsymbol{E} + \boldsymbol{v}_o\times\boldsymbol{B})\times\boldsymbol{q} \tag{1.41}$$

This is the exact answer for the torque on a pure dipole in a flat field.[18,20]

1.1.2.3.5 Susceptibilities of the Measures

The expansions for force and torque in the electrostatic two-body problem, radial field, and flat field are useful formula. However, they rely on knowledge of the charge distribution on both bodies in order to perform the integrations and find the measures. Unlike the gravitational two-body problem, these measures change as charge moves throughout the bodies. Recalculating the entire charge distribution for both bodies would be a very intensive process. Here, a method for predicting the measures from parameters that are much more feasible to measure in situ such as the voltage, attitude, and position of each craft is presented.

To do this, a matrix dependent on the relative position and attitude is used to translate the voltage of each craft into a representation of the charge distribution. From this distribution, the measures are formed as functions of the voltage of each craft. There are many ways to make this matrix, including the Method of Moments or Boundary Element Method. A recent addition is the Multi-Sphere Method, which uses hand-tuned parameters for the size and locations of spheres which are constrained to be equipotential.[3,3]

MSM emerged as a way to predict the force and torque with high-enough fidelity to be useful, while also evaluating fast enough to be practical. MSM approximates the satellite as a collection of spheres with variable position and radii. The voltage of any sphere is a function of both its own charge and the charge on neighboring spheres. If these spheres are far enough away to be approximated as point charges, the voltage on the i^{th} sphere is given by:[3,3,18]

$$V_i = \frac{1}{4\pi\epsilon_0}\frac{q_i}{R_i} + \sum_{j=1,\, j\neq i}^{N} \frac{1}{4\pi\epsilon_0}\frac{q_j}{r_{i,j}} \tag{1.42}$$

Where q_i and R_i are the charge and radius of the i^{th} sphere, respectively, and $r_{i,j}$ is the distance between spheres i and j. If the voltages of each sphere are given by $\boldsymbol{V} = [V_1, V_2, ...V_N]^T$ and the charges are given by $\boldsymbol{Q} = [q_1, q_2, ...q_N]^T$, the relationship between the two is $\boldsymbol{V} = [S]\boldsymbol{Q}$ or $\boldsymbol{Q} = [C]\boldsymbol{V}$, where $[C]$ is the capacitance matrix and $[S]$ is the elastance matrix defined below:[4]

$$[S] = \frac{1}{4\pi\epsilon_0}\begin{bmatrix} 1/R_1 & 1/r_{1,2} & \cdots & 1/r_{1,N} \\ 1/r_{2,1} & 1/R_2 & \cdots & r_{2,N} \\ \vdots & \vdots & \ddots & \vdots \\ 1/r_{N,1} & 1/r_{N,2} & \cdots & 1/R_N \end{bmatrix} \tag{1.43}$$

Since the voltage is assumed known, the charge distribution is found by numerically solving the linear system. If two conductors with n_1 and n_2 spheres each are considered, the elastance matrix can be put into block form:

$$\begin{bmatrix} \boldsymbol{V}_1 \\ \boldsymbol{V}_2 \end{bmatrix} = \frac{1}{4\pi\epsilon_0}\begin{bmatrix} S_1 & S_M \\ S_M^T & S_2 \end{bmatrix}\begin{bmatrix} \boldsymbol{Q}_1 \\ \boldsymbol{Q}_2 \end{bmatrix} \tag{1.44}$$

Where the voltage and charge of each craft are separated. Note that the self elastance terms S_1 and S_2 are much larger than the mutual elastance terms S_M because the inter-sphere separations are much smaller inside one body rather than between the two bodies. Additionally, the self elastance matrices contain the diagonal $1/R$ terms which are larger than the off-diagonal $1/r$ terms. As an example, consider a template box and panel spacecraft with an 8 meter boom made from 248 spheres and a 3 $\times$ 1 meter cylinder made from 138 spheres. The log of the elastance matrix for these two objects with a separation of 40 meters is shown in Figure 1.16.

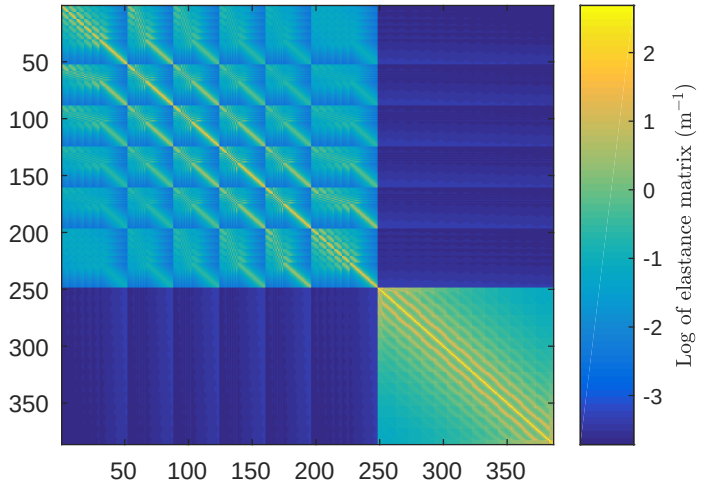

Figure 1.16: *Log of elastance matrix*

There are clearly four blocks, and the diagonals are $10^2 - 10^5$ times larger than the non-diagonal blocks. The blocky structure in the upper diagonal block comes from the method of assembly for the the box and panel spacecraft which is made from six rectangles. In general, the diagonal blocks will not change with relative position or attitude. The blocky structure, symmetry, and the time-fixed properties of the diagonal blocks are exploited when inverting using the Schur complement.

$$\begin{bmatrix} A & B \\ B^T & D \end{bmatrix}^{-1} = \begin{bmatrix} (A - BD^{-1}B^T)^{-1} & -A^{-1}B(D - B^TA^{-1}B)^{-1} \\ -D^{-1}B^T(A - BD^{-1}C)^{-1} & (D - B^TA^{-1}B)^{-1} \end{bmatrix} \tag{1.45}$$

Recognizing that A and D represent the self capacitance matrices, which contain much larger terms than the mutual matrix B, terms second order in B are dropped:

$$\begin{bmatrix} A & B \\ B^T & D \end{bmatrix}^{-1} \approx \begin{bmatrix} A^{-1} & -A^{-1}BD^{-1} \\ -D^{-1}B^TA^{-1} & D^{-1} \end{bmatrix} = \begin{bmatrix} C_1 & -C_1S_MC_2 \\ -C_2S_M^TC_1 & C_2 \end{bmatrix} \tag{1.46}$$

Where $[C_i] = [S_i]^{-1}$ for all blocks. The two matrices C_1 and C_2 are not functions of the relative separation and orientation, which means they will be constant in time. The terms in S_M are of the form $1/||\boldsymbol{R}_c + \boldsymbol{r}_{2_i} - \boldsymbol{r}_{1_j}||$. Since the center to center separation R_c is much greater than the dimensions of either craft r_1 or r_2, this is approximated as

$$[S_M]_{i,j} = \frac{1}{||\boldsymbol{R}_c + \boldsymbol{r}_{2_i} - \boldsymbol{r}_{1_j}||} \sim \frac{1}{R_c} \tag{1.47}$$

Approximating all elements in the mutual capacitance matrix as $1/R_c$ allows the relative attitude to be ignored while still capturing some first-order mutual capacitance and susceptibility. The elastance matrix is now approximately inverted as

$$\begin{bmatrix} \boldsymbol{Q}_1 \\ \boldsymbol{Q}_2 \end{bmatrix} = \frac{1}{4\pi\epsilon_0} \begin{bmatrix} C_1 & -C_1\mathbb{1}(n_1, n_2)C_2/R_c \\ -C_2\mathbb{1}(n_2, n_1)C_1/R_c & C_2 \end{bmatrix} \begin{bmatrix} \boldsymbol{V}_1 \\ \boldsymbol{V}_2 \end{bmatrix} \tag{1.48}$$

Where $\mathbb{1}(n, m)$ is a matrix consisting of ones of size (n, m). If the two bodies are both conductors,

each MSM sphere is at the same voltage this matrix equation is transformed to a vector equation

$$\boldsymbol{Q}_1 = [C_1]\mathbb{1}(n_1,1)V_1 - \frac{[C_1]\mathbb{1}(n_1,n_2)[C_2]}{R_c}\mathbb{1}(n_2,1)V_2 \tag{1.49}$$

$$\boldsymbol{Q}_2 = [C_2]\mathbb{1}(n_2,1)V_2 - \frac{[C_2]\mathbb{1}(n_2,n_1)[C_1]}{R_c}\mathbb{1}(n_1,1)V_1 \tag{1.50}$$

Now the charge on each MSM sphere is approximated as a function of a collection of matrices that do not change with state, and the scalar voltage of each craft. The susceptibility of the total charges, dipoles, and charge tensors to the voltage of each craft are found next.

1.1.2.3.5.1 Total Charges

The total charge on each spacecraft is found by summing the charge on each sphere

$$Q = \sum_{i=1}^{n_1} q_i = \mathbb{1}(1,n)\boldsymbol{Q} \tag{1.51}$$

Thus, the scalar charge of body 1 is given by

$$Q_1 = C_S V_1 + C_M V_2 \tag{1.52}$$

Where the self and mutual capacitances are given by

$$C_S = \mathbb{1}(1,n_1)[C_1]\mathbb{1}(n_1,1) = \sum_{i=1}^{n_1}\sum_{j=1}^{n_1}[C_1]_{i,j} \tag{1.53}$$

$$C_M = \frac{-\mathbb{1}(1,n_2)[C_1]\mathbb{1}(n_1,n_2)[C_2]\mathbb{1}(n_2,1)}{R_c} = -\frac{\sum_{i=1}^{n_1}\sum_{j=1}^{n_2}[C_1]\mathbb{1}(n_1,n_2)[C_2]}{R_c} \tag{1.54}$$

The scalar self capacitance can be computed with high fidelity using a MSM model with hundreds or thousands of spheres and re-used in each time step for computation. The numerator of the mutual capacitance can be similarly computed at high fidelity and then divided by the norm of the separation vector at each time step.

1.1.2.3.5.2 Dipole Moments

The dipole $\boldsymbol{q}$ is defined in a continuous charge distribution and MSM model as

$$\boldsymbol{q} = \int_B \boldsymbol{r}\mathrm{d}q = \sum_{i=1}^{N}\boldsymbol{r}_i q_i = [R]\boldsymbol{q} \tag{1.55}$$

where $[R]$ is a $3 \times N$ matrix containing the x, y, and z coordinates of each MSM sphere:

$$[R] = \begin{bmatrix} x_1 & \dots & x_N \\ y_1 & \dots & y_N \\ z_1 & \dots & z_N \end{bmatrix} \tag{1.56}$$

The dipole is given by

$$\boldsymbol{q} = \boldsymbol{\chi}_S V_1 + \boldsymbol{\chi}_M V_2 \tag{1.57}$$

Where the self and mutual susceptibilities of the dipole for body 1 are

$$\boldsymbol{\chi}_S = [R_1][C_1]\mathbb{1}(n_1, 1) \tag{1.58}$$

$$\boldsymbol{\chi}_M = \frac{-[R_1][C_1]\mathbb{1}(n_1, n_2)[C_2]\mathbb{1}(n_2, 1)}{R_c} \tag{1.59}$$

Once again, these 3×1 vectors can be computed with high fidelity from SMSM models of each body. Each element in the mutual term must be divided by the separation distance, which may change with time.

1.1.2.3.5.3 Charge Tensor

The charge tensor is defined from a continuous charge distribution or MSM model as

$$[Q] = \int_B -[\tilde{\boldsymbol{r}}][\tilde{\boldsymbol{r}}]\mathrm{d}q = \sum_i^N -[\tilde{\boldsymbol{r}_i}][\tilde{\boldsymbol{r}_i}]q_i \tag{1.60}$$

Define $[R_s]$ as a $3 \times 3N$ matrix containing the cross product matrix of each MSM sphere position and A is a $3N \times N$ matrix used to interweave three copies of the charge vector made from smaller matrices a.

$$[R_s] = \begin{bmatrix} [\tilde{\boldsymbol{r}_1}] \\ \vdots \\ [\tilde{\boldsymbol{r}_N}] \end{bmatrix} \qquad [a] = \begin{bmatrix} 1 \\ 1 \\ 1 \end{bmatrix} \qquad [A] = \begin{bmatrix} a & 0 & \dots & 0 \\ 0 & a & \dots & 0 \\ \vdots & \vdots & \ddots & \vdots \\ 0 & 0 & \dots & a \end{bmatrix} \tag{1.61}$$

The charge tensor is now found as a function of both voltages, and two 3×3 matrices,

$$[Q_1] = [\psi_S]V_1 + [\psi_M]V_2 \tag{1.62}$$

where the self and mutual susceptibilities of the charge tensor for body 1 are given by

$$[\psi_S] = [R_{s_1}]^T \mathsf{diag}([A][C_1]\mathbb{1}(n_1, 1))[R_{s_1}] \tag{1.63}$$

$$[\psi_M] = -[R_{s_1}]^T \frac{\mathsf{diag}([A][C_1]\mathbb{1}(n_1, n_2)[C_2]\mathbb{1}(n_2, 1))}{R_c}[R_{s_1}] \tag{1.64}$$

These matrices can be found using high fidelity MSM models before propagation and the mutual term can be adjusted by dividing by the separation distance. The derivations are done for body 1, but the susceptibilities for body 2 can easily be found by changing all subscript 2s to 1s and vice versa.

1.1.2.3.6 Flat Field Susceptibilities

A flat environmental field will change the charge distribution, but not the scalar charge. The only measures that contribute in a flat field are the dipole and the total charge. The scalar charge is still given by

$$Q = CV \tag{1.65}$$

To find the dipole, write the voltage of each sphere as a function both of the charges and its position relative to the total field $\boldsymbol{A} = \boldsymbol{E} + \boldsymbol{v} \times \boldsymbol{B}$ where $\boldsymbol{v}$ is the velocity with respect to the magnetic field.

$$\boldsymbol{V} = [C]^{-1}\boldsymbol{Q} - [R]^T\boldsymbol{A} \tag{1.66}$$

The charges are found by

$$\boldsymbol{Q} = [C](\boldsymbol{V} - [R]^T \boldsymbol{A}) \tag{1.67}$$

The dipole is then

$$\boldsymbol{q} = \boldsymbol{\chi}_S V_T + [\chi_A]\boldsymbol{A} \tag{1.68}$$

where the self and ambient susceptibilities are given by

$$\boldsymbol{\chi}_S = [R][C]\mathbb{1}(n,1) \tag{1.69}$$

$$[\chi_A] = [R][C][R]^T \tag{1.70}$$

for a model with n spheres. The ambient susceptibility is similar to the electric susceptibility used to calculate the polarization of dielectrics in an electric field.[18]

1.1.2.3.7 Numerical Validation

In a flat field, AFMs and MSM give the same answers down to machine precision assuming the same MSM model is used to calculate the susceptibilities of the measures because there is no truncation of a binomial series. For the two-body problem, the accuracy of predictive AFMs is checked against the truth model of SMSM, which places a large number of equal radius spheres uniformly across the surface of the body. The radius of all spheres is varied to achieve the known self capacitance. Although this method is slower to evaluate (due to the much larger number of spheres), it removes the need for hand tuning and has good accuracy relative to commercial FEA software.[2] An example SMSM model for two template "box and panel" spacecraft in close proximity is shown in Fig. 1.17. Note that charge, which is shown as color, tends to bunch up at the corners of conductors and is affected by the nearby spacecraft.

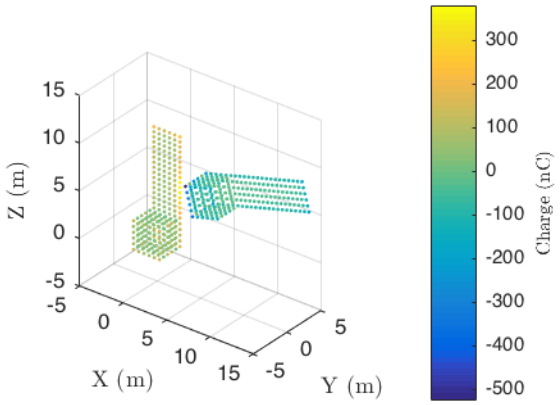

Figure 1.17: *Example SMSM configuration for two satellites*

For validation, one "box and panel" spacecraft has fixed location and attitude at the origin of the coordinate system. The second spacecraft occupies many different positions and attitudes on a shell of a given radius. SMSM is used to find the force and torque on the fixed craft. The force and torque is also predicted using AFMs with the susceptibilities $C_S, C_M, \boldsymbol{\chi}_S, \boldsymbol{\chi}_M, [\psi_S]$, and $[\psi_M]$ for each craft found before computation from the same 256-sphere SMSM model. The average percent error is computed for each spherical shell. The percentage error is computed as:

$$PE = 100 * \frac{||\boldsymbol{a}_{\text{AFM}} - \boldsymbol{a}_{\text{T}}||}{||\boldsymbol{a}_{\text{T}}||} \tag{1.71}$$

Where $\boldsymbol{a}$ is either the force or torque, and the subscript "T" indicates the truth model.

The second craft is placed at points on a spherical shell precomputed using a golden spiral algorithm[9] which arranges 20 points equidistantly on the surface of a sphere. The shells are varied in radius logarithmically from 15 to 200 meters in 10 steps. The attitude of the second object at each of these points is changed using three random Euler angles while the first object is held fixed in attitude at the origin. The mean percentage error per shell is shown in Figure 1.18

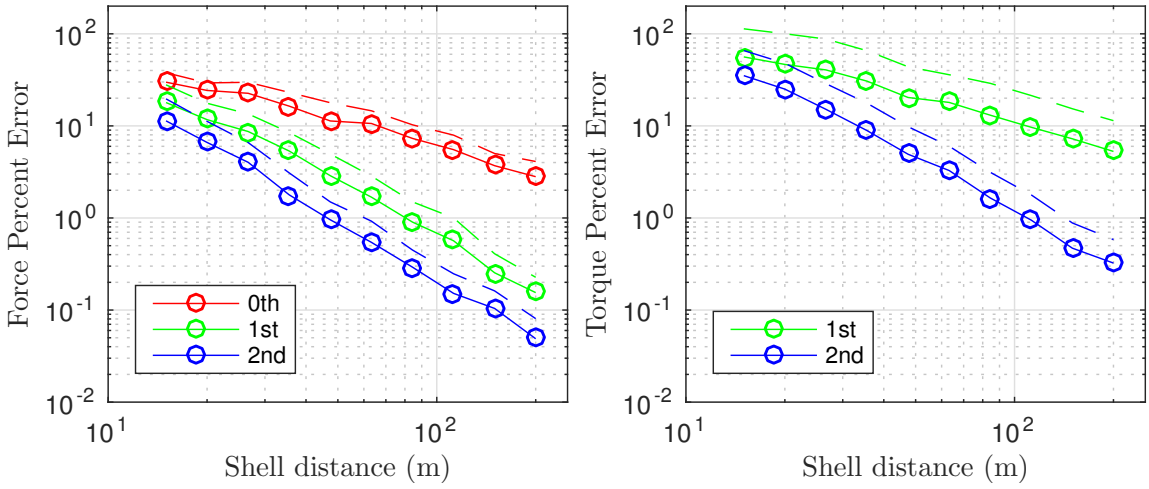

(a) Force percent error (b) Torque percent error

Figure 1.18: *Percentage errors for force and torque using predictive AFMs*

The mean percentage error for the zeroth, first, and second order expressions for force are shown as red, green, and blue lines in the force plot. Since there is no zeroth order term for torque prediction, only the first and second order expressions are shown in the torque plot. A dashed line is shown 1 standard deviation above each of these to give a sense of the variation a user should expect.

The errors are initially very high, a few hundreds of percent, but they drop quickly as the spacecraft move farther apart. Since the AFM derivation hinges on the assumption that the spacecraft sizes are much smaller than the distance between them, this matches intuition. The second order term for force drops below 5% error at 25 meters and the second order term for torque drops below 5% at 48 meters.

1.1.2.4 Analysis and Applications

There are many numerical methods for electrostatic force and torque prediction for conductors. However, they do not give good analytical forms for force and torque. This section summarizes previous work that curve fit the angular and voltage dependencies of electrostatic torque, and then uses AFMs to analytically predict the same result. Next AFMs are used to predict the torque in the case where the center of mass is not aligned with the exact center of the target object.

Bennett et. al. used MSM to calculate the torque on a 3 $\times$ 1 meter target cylinder due to a spherical tug craft for different voltages and angles.[21] This set up is shown in Fig. 1.19. The cylinder has the same voltage magnitude as the sphere, and is always positive while the tug

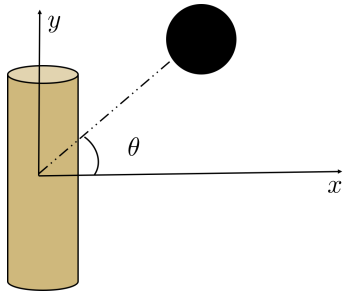

Figure 1.19: *Coordinate system for example analysis*

sphere can change the polarity of its voltage: $V_2 = |\phi|, V_1 = \phi$. The torque is only about the z axis due to the symmetry, and is shown as a function of both the angle θ and the voltage ϕ. This plot is shown for near field (2.5 meter separation) and far field (15 meter separation) cases in Fig. 1.20. The voltage dependance follows a quadratic relationship, and the angular dependance is well approximated by $\sin(2\theta)$. The torque is then curve fit to be:[21]

$$L = \gamma f(\phi)g(\theta) = \gamma\phi|\phi|\sin(2\theta) \tag{1.72}$$

In the near field, γ divides into a larger value for attraction γ_a and a smaller value for repulsion γ_r. At further separations the difference between attraction and repulsion is less evident.

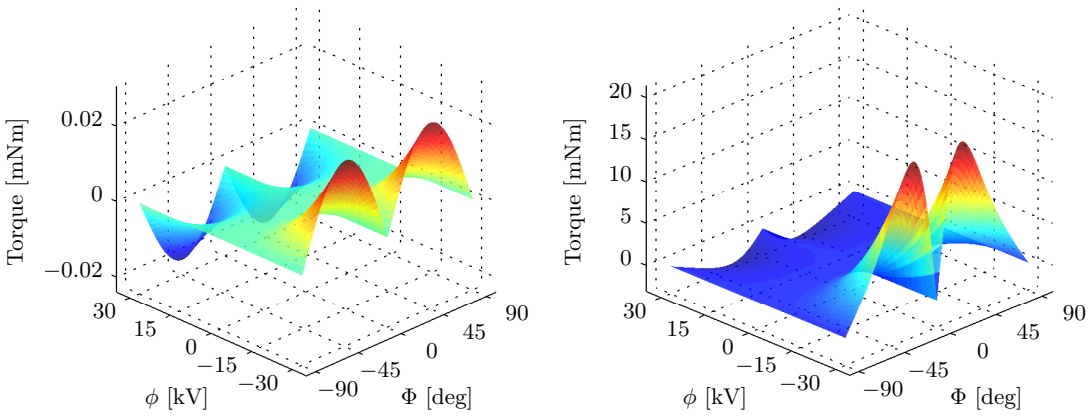

(a) Separation $d = 15$ m (b) Separation $d = 2.5$ m

Figure 1.20: *MSM torque surfaces at a separation distances of $d = 2.5$ m and $d = 15$ m for $V_1 = \phi$ and $V_2 = |\phi|$.*[21]

The angular, voltage, and attraction/repulsion trends that have been empirically found using MSM are now derived using AFMs. Referencing Eq. 1.38, the torque on a general body due to a nearby point charge is given by

$$\boldsymbol{L}_2 = \frac{Q_1}{4\pi\epsilon_0 R_c^3}\left[\boldsymbol{q}_2 + \frac{3}{R_c^2}[Q_2]\boldsymbol{R}_c\right] \times \boldsymbol{R}_c \tag{1.73}$$

re-writing this in terms of susceptibilities gives:

$$\boldsymbol{L}_2 = \frac{C_{S1}V_1 + C_M V_2}{4\pi\epsilon_0 R_c^3}\left[(\boldsymbol{\chi}_S + \frac{3}{R_c^2}[\psi_S]\boldsymbol{R}_c)V_2 + (\boldsymbol{\chi}_M + \frac{3}{R_c^2}[\psi_M]\boldsymbol{R}_c)V_1\right] \times \boldsymbol{R}_c \tag{1.74}$$

This equation is grouped into four separate terms

$$\begin{aligned}\boldsymbol{L}_2 = \frac{1}{4\pi\epsilon_0 R_c^3}\Big[&C_M(\boldsymbol{\chi}_S + \frac{3}{R_c^2}[\psi_S]\boldsymbol{R}_c)V_2^2 + C_{S1}(\boldsymbol{\chi}_M + \frac{3}{R_c^2}[\psi_M]\boldsymbol{R}_c)V_1^2 \\ &+ (C_{S1}(\boldsymbol{\chi}_S + \frac{3}{R_c^2}[\psi_S]\boldsymbol{R}_c) + C_M(\boldsymbol{\chi}_M + \frac{3}{R_c^2}[\psi_M]\boldsymbol{R}_c))V_1V_2\Big] \times \boldsymbol{R}_c \\ = \boldsymbol{A}V_1^2 + \boldsymbol{B}V_2^2 &+ (\boldsymbol{C}+\boldsymbol{D})V_1V_2 \end{aligned} \tag{1.75}$$

In this this 1-D case the torque is purely about the z axis and is written using scalars as

$$L = AV_1^2 + BV_2^2 + (C+D)V_1V_2 \tag{1.76}$$

The terms A and B have one mutual term and are thus 1st order in $(1/R_c)$, C is 0th order, and D is 2nd order. This means that in the far field terms linked to C will persist longer than those linked to A and B, which will persist longer than those linked to D. Because the mutual susceptibilities $(C_M, \boldsymbol{\chi}_M, [\psi_M])$ are negative but the self susceptibilities are positive, A, B and D are negative, but C is positive and larger than D.

Thus the following development switches to the positive variables $F = |A+B|$ and $G = C+D$, and makes use of the definitions $V_1 = \phi, V_2 = |\phi|$ to match prior work.[21] The torque for attractive (L_a) and repulsive (L_r) cases is given by:

$$L_r = (-F+G)\phi^2 = (-F+G)\phi|\phi| \tag{1.77}$$

$$L_a = (-F-G)\phi^2 = (F+G)\phi|\phi| \tag{1.78}$$

In the attractive cases the magnitude of the torque is larger because F and G add rather than subtract. This can be seen empirically in Fig. 1.20(a). Additionally, since G has the highest order term, it will matter most in the far field. Since F matters less in the far field, the difference between the attractive and repulsive torque decreases in the far field, which can also be seen by comparing Fig. 1.20(a) and 1.20(b).

In prior work Reference[21] numerically fit the far field parameter γ to a value of $2.234 * 10^{-14}$ for a 3 meter by 1 meter cylinder 15 meters away from a 1 meter diameter sphere. To compute the corresponding value from AFMs, assume that the center of mass is perfectly aligned with the center of charge so that $\boldsymbol{\chi}_S = 0$ and the body axes are aligned so that $[\psi_S]$ is given by diag(ψ_B, ψ_s, ψ_B), where $\psi_B > \psi_s$. This represents the case of a perfectly axis-symmetric cylinder as shown in Figure 1.19. Ignoring the mutual part of G which decays quickly gives the torque as

$$\begin{aligned} L &= \frac{-3C_{S1}}{4\pi\epsilon_0 R_c^5}\tilde{\boldsymbol{R}}_c[\psi_S]\boldsymbol{R}_c V_1V_2 \\ &= \frac{3C_{S1}}{8\pi\epsilon_0 R_c^3}(\psi_B - \psi_s)\sin(2\theta)V_1V_2\hat{\boldsymbol{z}} \end{aligned} \tag{1.79}$$

where G is defined as

$$G = \frac{3C_{S1}}{8\pi\epsilon_0 R_c^3}(\psi_B - \psi_s) \tag{1.80}$$

SMSM is used to find the values of ψ_S and ψ_B which gives $G \approx 2.531 * 10^{-14}$, only a 13% difference with the numerically fit value used in Reference 21. These two results agree well considering that only a second order AFM model is used and the mutual part of G is ignored, and Reference 21 fits γ to the full MSM solution.

Now consider the same cylinder, but allow the center of mass to move within the craft by a few centimeters along the y axis ($\boldsymbol{\chi}_S = [0, \chi_S, 0]^T$). The torque is still only about the z axis and is given by

$$\begin{aligned}\boldsymbol{L}_2 &= \frac{-C_{S1}}{4\pi\epsilon_0 R_c^3}\tilde{\boldsymbol{R}}_c\Big(\boldsymbol{\chi}_S + \frac{3}{R_c^2}[\psi_S]\boldsymbol{R}_c\Big)V_1V_2 \\ &= \frac{-C_{S1}}{8\pi\epsilon_0 R_c^2}\Big[\chi_S\cos(\theta) + \frac{3(\psi_B - \psi_s)}{2R_c}\sin(2\theta)\Big]V_1V_2\hat{\boldsymbol{z}} \end{aligned} \tag{1.81}$$

Setting $\chi_S = 0$ recovers Eq. (1.79), but even a small CM offset can make the $\cos(\theta)$ term dominate, especially at large separations. As the CM moves away from the geometric center, χ_S grows linearly, and some elements of ψ_S grow quadratically. The torque as a function of θ is shown for a variety of CM offsets in the example of the same cylinder 15 meters away from a 1 μC point charge in Figure 1.21. The different curves are for different values of χ_S – the center of mass offset is shown in the legend.

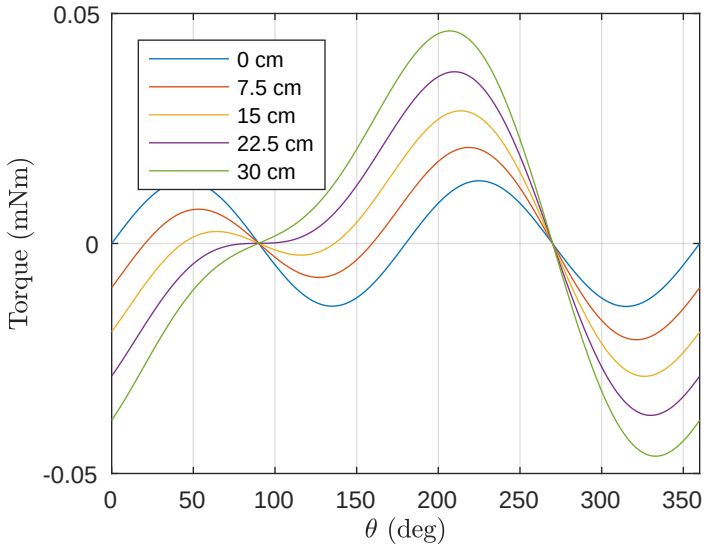

Figure 1.21: *Torque on cylinder for a variety of center of mass offsets*

The torque slowly changes from a perfect sin(2θ) to an augmented -cos(θ) curve as the CM offset varies. The magnitude of the torque also increases by a factor of 3.38. This factor is even greater at further separations since the $\cos(\theta)$ term has lower order in $1/R_c$. Knowledge of center of mass to center of charge differences are essential for the stability of control laws used for de-spinning of passive space debris. If the center of charge location is not properly accounted for, the sign of the predicted torque can be wrong, leading to instabilities in the closed-loop control discussed in Reference.[21]

1.1.3 Geosynchronous Debris Perturbation Modeling of Electrodynamic Disturbances

1.1.3.1 Overview of GEO perturbations

The two-body equations of motion are not sufficient to describe the orbital motions of all objects. At low altitudes, Earth's spherical gravity and drag strongly perturb certain orbits. Further out in

Geosynchronous (GEO) orbit, all objects are perturbed by lunar and solar gravity, and some High Area-to-Mass (HAMR) objects are strongly perturbed by Solar Radiation Pressure (SRP).[22]

However, SRP is not sufficient to explain the motions of all HAMR GEO objects. The 28th International Symposium for Space Technologies and Sciences held in London in June 2011 identified this issue. In particular, Professor Schildknecht discussed that families of HAMR objects have been identified whose mean motion changes remain very small, while the orbital angular momentum of these objects changes significantly with eccentricities varying up to 0.7. Additionally, Wiesel recently reported[23] some near-GEO debris objects which appear to accelerate *towards* the sun during the propagation interval, which is impossible with SRP. One possible source of this discrepancy is that these objects may be interacting with Earth's magnetic field.

Some of these objects that are hard to model are thought to be torn-off pieces of Multi-Layer Insulation (MLI).[24] Samples returned from the Hubble Space Telescope showed cracks in areas of constrained loading, and had a tendency to curl up when peeling off.[25] MLI may peel off of GEO spacecraft, and could charge to very high potentials during geomagnetic storms.[26] This charging causes a translational Lorentz force, and may cause a significant electrostatic torque depending on the relative distance between the center of charge and center of mass. Additionally, if the object is rotating relative to an external magnetic field it will experience a eddy current torque, which acts to slow the rotation.

Früh et al. where the first to publish results modeling the electrostatic charging effects on HAMR objects.[27] This initial work adds the Lorentz force and eddy torque to the more standard list of perturbations for a HAMR plate. Including these two new effects changes the orbit by nearly a tenth of a degree in inclination and 0.002 in eccentricity after only 12 hours. Paul et al.[28] modeled a sphere for which torques are not included and found much less dramatic results. Hughes et. al.[1] considered a flat plate similar to Früh et al., but added electrostatic torques as a perturbation and found that considering these perturbations caused large orbital impacts.

1.1.3.2 Overview of AFM Force and Torque Estimation for Flat Plates

The force and torque on a charged conductor are the result of the Lorentz field and the ambient electric field: $\boldsymbol{A} = \boldsymbol{E} + \boldsymbol{v} \times \boldsymbol{B}$, where $\boldsymbol{A}$ is the total field, $\boldsymbol{E}$ is the environmental electric field, $\boldsymbol{B}$ is the environmental magnetic field, and $\boldsymbol{v}$ is the velocity of the spacecraft relative to the magnetic field, which co-rotates with Earth. Although electric fields are observed in L shells similar to GEO,[29] they are typically oscillatory and would not change an orbit, although they may be able to cause shape changes in flexible materials.

The differential force on a differential charge moving at $\boldsymbol{v}$ subject to $\boldsymbol{E}$ and $\boldsymbol{B}$ fields is given by:[18]

$$\mathrm{d}\boldsymbol{F} = \mathrm{d}q(\boldsymbol{E} + \boldsymbol{v} \times \boldsymbol{B}) \tag{1.82}$$

The torque about the center of mass on a body is defined as $\int_B \boldsymbol{r} \times \mathrm{d}\boldsymbol{F}$, where $\boldsymbol{r}$ points from the center of mass to the volume element. Using the differential force to find the net force and torque on a body gives:

$$\boldsymbol{F} = \int_B (\boldsymbol{E} + \boldsymbol{v} \times \boldsymbol{B})\mathrm{d}q \tag{1.83}$$

$$\boldsymbol{L} = \int_B \boldsymbol{r} \times (\boldsymbol{E} + \boldsymbol{v} \times \boldsymbol{B})\mathrm{d}q \tag{1.84}$$

If a body is rotating, the velocity relative to the magnetic field will vary over the body. Assuming an orbit inclined at 16°, the relative velocity at GEO is ∼1 km/s. If the body has a radius of 1 meter,

and is rotating at 1 degree per second, the relative velocity from rotation is 10^{-5} times smaller than that from the orbit. In this analysis it is neglected.

Define the charge separation vector $\boldsymbol{q}$ and the total charge Q below to simply the force and torque:

$$Q = \int_B \mathrm{d}q \qquad \text{and} \qquad \boldsymbol{q} = \int_B \boldsymbol{r}\mathrm{d}q \tag{1.85}$$

Using the definitions in Eq. (1.85) in the integrals in Eq. (1.83) and (1.84) gives the following results for force and torque:

$$\boldsymbol{F} = (\boldsymbol{E} + \boldsymbol{v} \times \boldsymbol{B})\, Q \qquad \boldsymbol{L} = -(\boldsymbol{E} + \boldsymbol{v} \times \boldsymbol{B}) \times \boldsymbol{q} \tag{1.86}$$

If the charge distribution were known at all times, Eq. (1.86) would be enough to predict force and torque, however, the charge distribution changes as the object rotates and charges or discharges. This subsection predicts the AFM parameters Q and $\boldsymbol{q}$ using the body voltage, ambient field $\boldsymbol{A}$, and two matrices found from the SMSM models discussed earlier.

If the voltage V is known, Q can easily be obtained through $Q = C_s V$ where C_s is the self capacitance, which can be found once using a commercial FEA tool as long as the objet does not change shape. The voltage on a spacecraft is a function of the solar flux, plasma environment, and the material properties of the spacecraft. There are many tools for predicting this voltage including analytical current balance methods as shown in Lai[30] or with computational tools such as NASCAP or SPIS.

Predicting the dipole is slightly more complex. The dipole can be thought of as the total charge Q multiplied by the separation of the center of charge from the center of mass. The charge will increase with the voltage, which will increase the magnitude of the dipole but not change the direction. An ambient field will push all the charge towards one end of the spacecraft. How far an ambient field is able to move the center of charge is dependent on the geometry and attitude of the spacecraft with respect to the ambient field. These two effects are lumped into the following equation:[16]

$$\boldsymbol{q} = \boldsymbol{\chi}_S V + [\chi_A]\boldsymbol{A} \tag{1.87}$$

Both of these susceptibilities ($\boldsymbol{\chi}_S$ and $[\chi_A]$) are found from SMSM models made with 100 spheres. The center of charge moves due to both the offset between center of mass and center of charge ($\boldsymbol{\chi}_S$) and the ambient field ($[\chi_A]$). In this analysis, offsets of centimeters are used which overwhelms the ambient effect. For example, this 10 cm plate charged to 30 kV with a $2\sqrt{2}$ cm offset in a Lorentz field created from a velocity of 1 km/s orthogonal to a 100 nT magnetic field will only see a charge-center movement of 7.7 pm. The torque produced by the center of mass offset is a much stronger (more than 9 orders of magnitude) than the torque created by the induced effect. Nonetheless, both effects are included.

$$\boldsymbol{F} = C_S V \boldsymbol{A} \tag{1.88}$$

$$\boldsymbol{L} = (\boldsymbol{\chi}_S V + [\chi_A]\boldsymbol{A}) \times \boldsymbol{A} \tag{1.89}$$

Note that $\boldsymbol{\chi}_S$ and $[\chi_A]$ are constants in the body frame much like the inertia tensor. Direction cosine matrices can be used to rotate $\boldsymbol{A}$ into the body frame or $\boldsymbol{\chi}_S$ and $[\chi_A]$ into whatever frame $\boldsymbol{A}$ is in to compute torque.

1.1.3.3 Orbital Impact Considering Only Charging

Charging combines with Earth's magnetic field to create an electrostatic force and torque. In this section, only the electrostatic force (Lorentz force) is considered from the perspective of orbital

element changes and the maximum magnitude of acceleration, as torques have no direct effect on the orbital motion. Prior work has postulated if such Lorentz forces on their own could cause significant perturbations.[23] Thus, this section illustrates conservative estimates on the maximum perturbations that could be expected from natural charging. In this analysis a constant voltage of -30 kV is used, even though it will likely change with local time due to changing plasma conditions.

1.1.3.3.1 Gaussian Variation of Parameters

Gaussian variation or parameters are used to find the net impact of the Lorentz force. To find the mean secular rates of the orbital elements, integrate the rates with respect to time over one period. In a perfectly circular orbit this can be done analytically because $\nu = nt$, and Kepler's equation does not have to be solved. This is done for semi-major axis, eccentricity, inclination, and RAAN below. The argument of perigee rate is undefined for a circular orbit, and mean anomaly does not change observability.

$$\dot{a} = \frac{2}{n\sqrt{1-e^2}}\left(e\sin(\nu)a_R + \frac{p}{r}a_S\right) \rightarrow \Delta a = \int_0^P \frac{2}{n\sqrt{1-e^2}}\left(e\sin(nt)a_R + \frac{p}{r}a_S\right)\mathrm{d}t$$
$$= \frac{2P}{n\sqrt{1-e^2}}\frac{p}{r}a_S \tag{1.90}$$

$$\Delta e = \int_0^P \frac{\sqrt{1-e^2}}{na}\left[\sin(\nu)a_R + \left(\cos(\nu) + \frac{e+\cos\nu}{1+e\cos\nu}\right)a_S\right]\mathrm{d}t = 0 \tag{1.91}$$

$$\Delta i = \frac{1}{2\pi}\int_0^{2\pi} \frac{r\cos(\nu+\omega)}{na^2\sqrt{1-e^2}}a_W\,\mathrm{d}\nu = 0 \tag{1.92}$$

$$\Delta\Omega = \frac{1}{2\pi}\int_0^{2\pi} \frac{r\sin(\nu+\omega)}{na^2\sqrt{1-e^2}\sin(i)}a_W\,\mathrm{d}\nu = 0 \tag{1.93}$$

For a perfectly circular orbit, the only secular change is in the semi-major major axis, and is caused by an along-track acceleration. The Lorentz force cannot be in that direction, as the force must act perpendicular to both the velocity and the magnetic field. Since the magnetic field at equatorial GEO points mostly north, the Lorentz force will be nominally in the radial direction. In reality no orbit is perfectly circular, and osculating changes to the elements can cause secular changes through feed back, but this simple analysis shows that a Lorentz force has no first-order impact on a circular orbit.

1.1.3.3.2 Acceleration Magnitude Analysis

In the earlier section, it is shown that there is no expected secular drift due to the Lorentz force for a circular equatorial GEO orbit. In this section the maximum accelerations caused by the Lorentz force are compared to other orbital forces. This provides an estimate of how much charging impacts osculating perturbations. Consider the example case of a charged aluminum sphere subjected only to the point mass gravity of the Earth, SRP, and the Lorentz force. For SRP, assume the cannonball model with full absorption. For the calculation of the Lorentz force, assume a magnetic strength of 100 nT, a velocity difference of 1 km/sec, and a voltage of -30 kV. The velocity difference comes from the orbit being inclined to 16°, as the magnetic field co-rotates with Earth, and -30 kV is a worst-case number. Gravity is calculated for geosynchronous altitude.

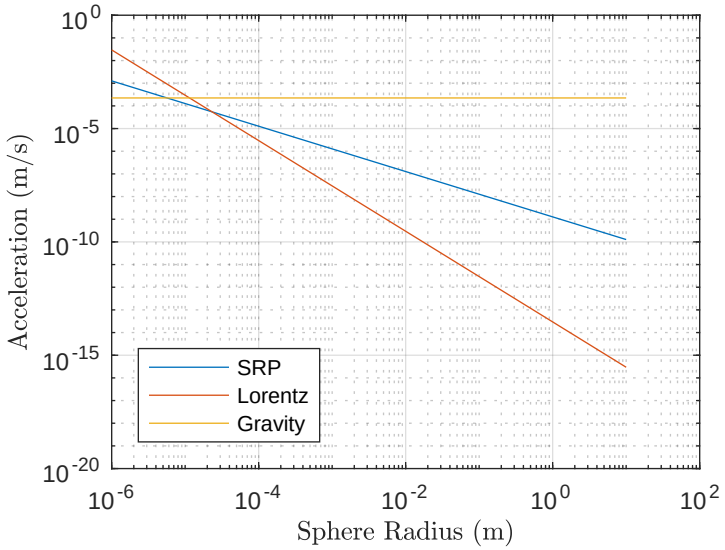

Figure 1.22: *Accelerations of an aluminum sphere as a function of size*

The acceleration of the aluminum sphere due to these three perturbations as a function of its size is shown in Fig. 1.22. As expected, the acceleration due to gravity is constant with respect to the object size. The force from SRP grows with the square of the radius, and the Lorentz force grows linearly with the radius, but the mass grows as the cube of the radius. This means that the SRP acceleration decays as $1/r$ while the Lorentz acceleration decays as $1/r^2$. Because of this, Lorentz forces are more significant when the object is small, as can be seen in Fig. 1.22. For the situation modeled here, charging is as significant as SRP for sphere with $r \sim 20\mu$m and charging is the dominant acceleration for spheres smaller than 10 μm. For larger spacecraft with $r \sim 1 - 10$m, gravity dwarfs SRP, which dwarfs charging. For more conservative charging levels, the sphere must be even smaller for charging to matter. This analysis shows that Lorentz forces only impact dust-sized object in a significant manner. For larger objects as spacecraft or spacecraft components such as torn-off Mylar these electromagnetic forces are exceeding small and have a negligible impact. However, the impact of electromagnetic perturbations does not end here. The next section investigates the impact of electromagnetic torques along with other perturbations.

1.1.3.4 Numerical Propagation of Nominal Case Including Charging

1.1.3.4.1 Perturbations Considered

Numerous perturbations due to Earth, moon, sun solar pressure, electrostatics and Eddy current influence the orbits of HAMR objects at GEO. Each perturbation considered is detailed in Tab. 1.8 with either the exact equation or a short description.

Eddy current torque is included as well. When a conductor spins in a magnetic field, the mobile electrons move in loops because of induction. No net force is felt because the current path is closed, but an eddy current torque is felt. Gomez recently developed a general method for calculating this torque[31] through

$$\boldsymbol{L} = ([M](\boldsymbol{\omega} \times \boldsymbol{B})) \times \boldsymbol{B} \tag{1.94}$$

Table 1.8: *Forces and Torques acting on Space Debris*

Perturbation	Force	Torque
Earth gravity	Spherical Harmonics up to 4th order	$\boldsymbol{L} = \frac{3\mu}{R_c^5}\boldsymbol{R}_c \times [I]\boldsymbol{R}_c$
Lunar gravity	point-mass gravity	0
Solar gravity	point-mass gravity	0
SRP	Absorptive, specular, and diffuse reflection	$\boldsymbol{L} = \boldsymbol{r}_{\text{sep}} \times \boldsymbol{F}_{\text{SRP}}$
Electrostatic	$\boldsymbol{F} = Q\boldsymbol{v} \times \boldsymbol{B}$	$\boldsymbol{L} = \boldsymbol{q}_{\text{sep}} \times (\boldsymbol{v} \times \boldsymbol{B})$
Eddy Currents	0	$\boldsymbol{L} = ([M](\boldsymbol{\omega} \times \boldsymbol{B})) \times \boldsymbol{B}$

where $[M]$ is the magnetic tensor. For a flat plate, the matrix $[M]$ is given by

$$[M] = C_T \frac{\sigma e}{4} \boldsymbol{n}\boldsymbol{n}^T \tag{1.95}$$

where σ is the conductivity, C_T is a constant dependent on shape and size, and $\boldsymbol{n}$ is a unit vector normal to the plane. For a rectangle with length l greater than width w, C_T is found using St. Venant beam theory:

$$C_T \approx \frac{lw^3}{3(1 + 1.38(\frac{w^2}{l^2})^{1.6})} \tag{1.96}$$

in the cases considered, the normal axis of the plate is $\hat{\boldsymbol{z}}$ which makes the torque equal to

$$\boldsymbol{L} = ([M](\boldsymbol{\omega} \times \boldsymbol{B})) \times \boldsymbol{B} = C_T \frac{\sigma e}{4} (\omega_1 B_2 - \omega_2 B_1) \begin{bmatrix} B_2 \\ B_1 \\ 0 \end{bmatrix} \tag{1.97}$$

It is interesting to note that if the plate is spinning about its axis of maximum inertia, ω_3 will be large and ω_1 and ω_2 will be small or zero. The eddy torque will also be small, and the object's spin will be relatively unaffected. If the object is tumbling, only the spin rates about the body 1 and 2 axes are removed and it will eventually fall into a stable spin about its axis of major inertia.

The magnitude of the SRP force is determined by the solar flux and the illuminated area. The direction is governed by the amount of light that is absorbed and reflected specularly and diffusely. The SRP force is given by:[32]

$$\boldsymbol{F} = p_{SRP} A \cos(\theta) \left[\rho_A \hat{\boldsymbol{s}} + 2\rho_s \cos(\theta) \hat{\boldsymbol{n}} + \rho_d (\hat{\boldsymbol{s}} + \frac{2}{3}\hat{\boldsymbol{n}}) \right] \tag{1.98}$$

Where θ is the angle between the sun-pointing line and the face normal, $\hat{\boldsymbol{s}}$ is the sun-pointing vector, $\hat{\boldsymbol{n}}$ is normal to the plane, and ρ_A, ρ_S, and ρ_D are the absorptive, specular, and diffuse coefficients, respectively, which must sum to unity.

1.1.3.4.2 Magnetic Field Models

Earth's magnetic field at low altitudes is well approximated by the IGRF model, which takes many factors affecting Earth's geodynamo into account. Outside Earth's magnetosphere, the magnetic field is purely a function of space weather and has little to no dependance on Earth's own magnetic field. At GEO, these two effects combine to make a complex function of time and space weather parameters. The current state of the art for modeling this field is the Tsyganenko

model.[33] There have been many versions and updates to this model, but in this analysis the 2001 version is used with GEOPACK 2008[1] for coordinate transforms.

Since the magnetic field is position dependent, the model is run at each timestep. The time is assumed to be January 1, 2002, midnight, for all runs. The space weather parameters used are shown in Tab. 1.9, and are representative values that are used by the Community Coordinated Modeling Center (CCMC) on their single-run website[2]

Table 1.9: *Space weather parameters used for Tsyganenko model*

Parameter	Value
Solar Wind Dynamic Pressure	4 nPa
Solar Wind Velocity	400 km/s
IMF B_y	6 nT
IMF B_z	-5 nT
DST	-30 nT

This produces a magnetic field model that accounts for the solar wind and Earth's geodynamo. As shown in Fig. 1.23, the field is not well-modeled by a tilted dipole alone. The x and y axes are in earth radii, and the z axis is arbitrary. Space weather will have a dramatic effect on the charging and the magnetic field strength and direction. Solar storms can cause high charge levels and cause strong electric and magnetic fields.[29] Since these fields are short-lived and oscillatory, the subsequent electrostatic perturbations are not directly capable of causing dramatic orbital changes. However, they may cause shape changes which may then change the orbit. For instance, consider a flexible sheet of conducting mylar, which when uncharged is wadded into a small ball. If it suddenly charges from +10 V to -10 kV due to a solar storm, it may inflate and change its area by a factor of 10 or 100. This would dramatically affect the SRP force and torque which would dramatically affect the orbit.

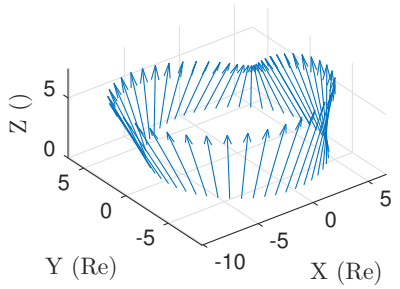

Figure 1.23: *ECI Magnetic field used in this study, Z axis is arbitrary*

The voltage of a conducting sheet is perhaps one of the easier spacecraft charging problems one could pose, nonetheless it is a still a hard problem. The voltage was modeled under very harsh charging conditions by Früh et al.[27] for a sheet with one side conducting and one of different dielectrics such as Kapton and Mylar. The most extreme voltage found was slightly more negative than -30 kV and occurred when using the very high ATS-6 flux. In this analysis, a simple and constant value of -30 kV is used to give a rough maximum for the charge level. In many circumstances, the voltage would be much smaller.

[1] http://ccmc.gsfc.nasa.gov/modelweb/magnetos/tsygan.html
[2] http://ccmc.gsfc.nasa.gov/requests/instant/tsyganenko.php

Table 1.10: *Nominal HAMR propagation values*[27,36]

Parameter	Value
thickness	1/4 mil (6.35 μm)
density	1.39 g/cm^3
L_x	10 cm
L_y	10 cm
C	4.02 pF
$\boldsymbol{r}_{\text{CC}}$	$[2,2,0]^T$ cm
$\boldsymbol{r}_{\text{CP}}$	$[2,2,0]^T$ mm
$\boldsymbol{\chi}_S$	$80.43 * [1,1,0]^T$ fF m
$\chi_A(1,1)$	$5.393 * 10^{-11}$ F m^2
$\chi_A(2,1), \psi_A(1,2)$	$1.711 * 10^{-14}$ F m^2
$\chi_A(2,2)$	$1.613 * 10^{-12}$ F m^2
ρ_A	0.5
ρ_S	0.2
ρ_D	0.3
σ_C	3.5*10^7 S/m
$M_{3,3}$	333.12 Sm^4

1.1.3.4.3 Self Capacitance Estimation for Rectangular Plates

Calculating the self capacitance of a square plate is a well-studied problem. J.C. Maxwell himself estimated it to be 0.40 pF for a 1 cm square,[7] and current computation methods now estimate it at 0.4019 pF.[34] The self capacitance of two geometrically similar objects, will scale linearly with any dimension. For instance, the self capacitance of a sphere is given by $C = 4\pi\epsilon_0 R$. For a flat plate, capacitance can be expressed as $c = C/B$ where C is the true capacitance in Farads, and B is the bigger side of the plate. For a square plate B is just the edge length.

Reitan and Higgins[35] produced a very useful curve from which c can be extrapolated from the aspect ratio of the big to small side B/S. Ten points are read off this curve, and a power law is used to fit it with good accuracy ($r^2 = 0.9995$). The power law is shown below.

$$c = \left(0.402 * 10^{-10} \frac{\text{F}}{\text{m}}\right)\left(\frac{B}{S}\right)^{-0.4733} \tag{1.99}$$

The capacitance is used to convert the voltage, which can often be estimated from space weather parameters and is assumed to not depend on size or shape, to the charge. The amount of charge will dictate the magnitude of the force.

1.1.3.4.4 Numerical Propagation of Nominal Case

A nominal case of a thin rigid square of mylar is considered first. The material parameters are shown in Tab. 1.10. The inertia tensor is computed assuming constant density. The center of charge is separated from the center of mass by $\boldsymbol{r}_{\text{CC}}$ while the center of pressure, which is used for SRP, is separated from the center of mass by $\boldsymbol{r}_{\text{CP}}$. Any matrix values not explicitly defined are zero.

Four different models are used to propagate the orbit of the plate. The longitude and altitude departure over time are shown in Fig. 1.24. Model 1 is the full model, model 2 neglects electrostatic force and torque, model 3 additionally neglects eddy torques, and model 4 additionally neglects attitude-dependent SRP and uses a cannonball model. The orbits for each of these propagators all start at the same place, with no altitude departure and 241° longitude. By the end of the 48 hour propagation, the full model predicts a location that is 1441 km away from the model that neglected only statics, 2351 km away from the model that neglected statics and eddy torques, and 3354 km away from the model that neglected all electromagnetic effects and used cannonball SRP.

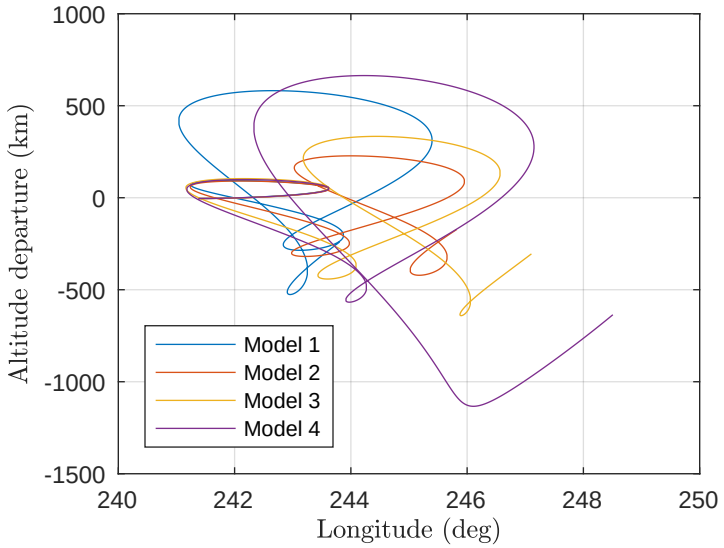

Figure 1.24: *Longitude and altitude for plates with different propagation models*

The Gaussian variation of parameters analysis shows that electrostatic forces can only affect the orbit by a few tens of meters per orbit, yet Fig. 1.24 shows thousands of kilometer departures caused by including electrostatic and eddy effects. To investigate how such small forces and torques can cause such a drastic change in the orbital position, the magnitudes of the linear and rotational accelerations are now investigated. For the full propagator model, the norm of the linear and rotational accelerations are shown in Fig. 1.25.

As is expected for a circular orbit, the linear acceleration from Earth's gravity stays constant. The SRP acceleration is heavily attitude dependent and changes magnitude quickly as the plate tumbles, but is still by far the largest perturbation. Solar and Lunar gravity change slowly as the distance to the plate changes. The electrostatic force is the smallest by many orders of magnitude.

As for the torques SRP is still the largest, but is followed more closely by electrostatic and eddy torques while gravity gradients are many orders of magnitude smaller. Electrostatic and eddy torques cause rotational accelerations near 1 Radian per hour^2, which means that in one hour they could change the attitude by 1/2 a radian if they acted in the same direction using $\Delta\theta = \frac{1}{2}\ddot{\theta}\Delta t$. This is the key to how electrostatic and eddy effects can change an orbit so drastically — over time periods longer than a few hours, electrostatic and eddy torques can significantly change the attitude of a HAMR object, which changes SRP, which changes the orbit.

This matches the findings of other authors as well. Früh et al[27] found that including eddy torques for a thin HAMR object caused major orbital differences, but Paul et al.[28] modeled a sphere for which torques do not act and found minimal orbital differences. The Lorentz force cannot change the orbits of objects large enough to be observable. However electrostatic and eddy

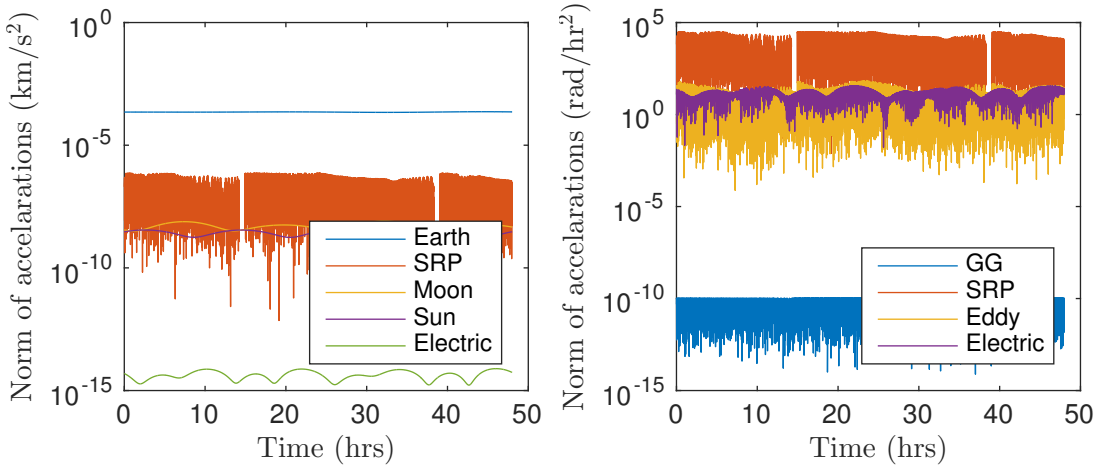

(a) Linear Accelerations (b) Angular Accelerations

Figure 1.25: *Accelerations for charged HAMR object during propagation*

torques can change the attitude, and if the attitude influences SRP, the orbit can be measurably changed.

1.1.3.4.5 Monte Carlo Analysis over Initial Attitude

Attitude makes a large difference in the final position of a HAMR object. This begs the question of whether the thousands of kilometers differences that come from including or neglecting electromagnetic effects are larger or smaller than the normal spread from initial attitude. Put more mathematically, assuming a distribution of initial attitudes, are the differences in the means of the distribution of final positions when including or neglecting electromagnetic effects significant when compared with the standard distribution of either population?

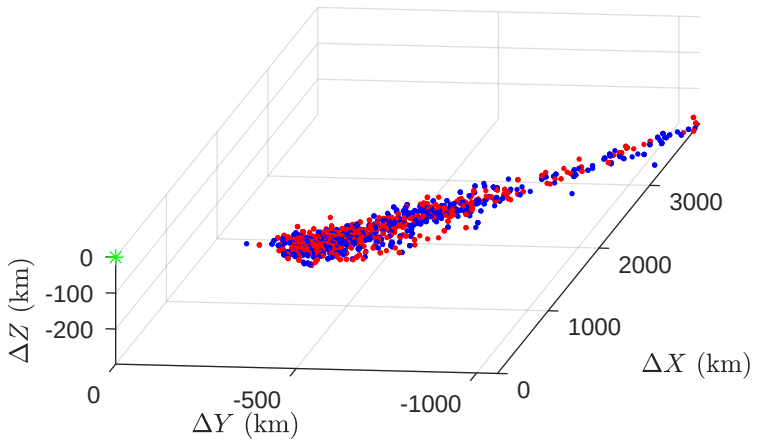

Figure 1.26: *Final positions after of HAMR objects at GEO after 24 hour propagation including or neglecting electromagnetic effects*

To answer this question, the initial attitude of the plate is randomized in a Monte Carlo analysis, and propagated with models that either include electromagnetic effects (electrostatic force and torque as well as eddy torques). One thousand initial attitudes are propagated for 24 hours and the final position and velocities for both models are stored in a master file. The final ECI positions are shown in Fig. 1.26. The red dots represent plates that were propagated including electromagnetic effects, and the blue dots represent plates that were propagated neglecting these effects. The green point is the original position, where all points would lie if a two body propagator is used for this 24 hour propagation. The distances on the axes are given relative to the original position, and are in the ECI coordinate system.

The spread for either population is thousands of km in the along-track direction, which is comparable to the differences found with different propagation models in Fig. 1.24. The mean and standard deviation of the ECI positions for both the populations propagated with and without electromagnetic effects, and are compared against each other. The differences in the means is divided by the standard deviation in the positions of the population propagated without electromagnetic effects and is shown below. Dividing by the standard deviation of the charged population gives very similar results.

$$\Delta\mu_X = -0.205\,\sigma_X \qquad \Delta\mu_Y = 0.219\,\sigma_Y \qquad \Delta\mu_Z = 0.237\,\sigma_Z \tag{1.100}$$

The difference in the means is a significant fraction of the standard deviation when randomizing initial attitude, which suggests that including electromagnetic effects does change the orbits of uncontrolled HAMR objects beyond their normal spread. To further investigate this, the classical orbit elements are computed for both populations at the end of the propagation period. The final distributions are shown for both the propagation models.

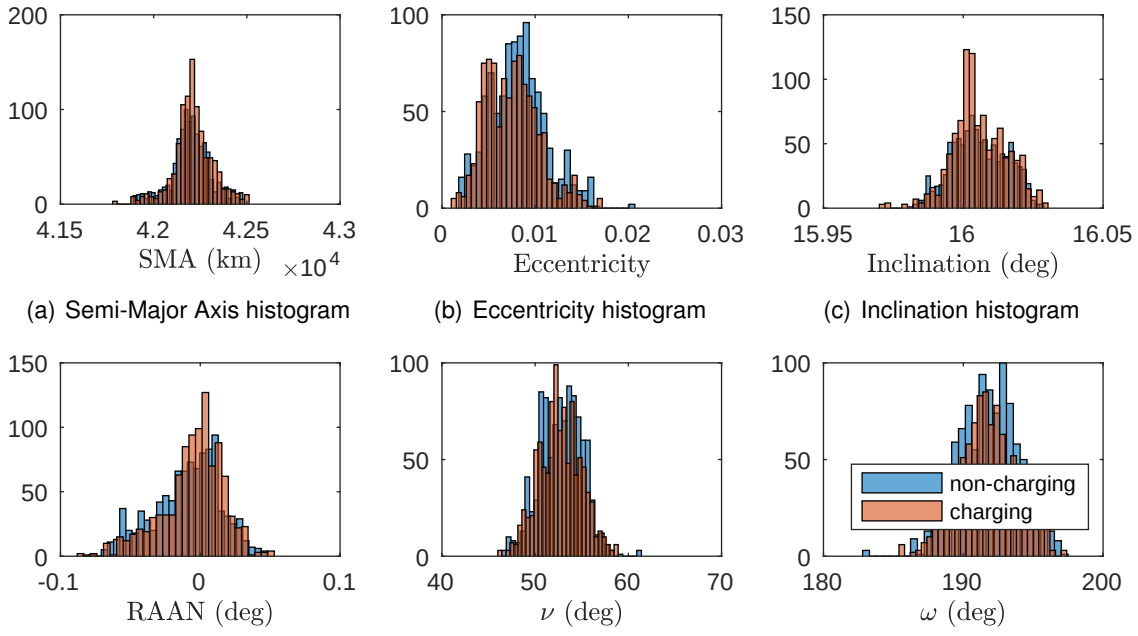

(a) Semi-Major Axis histogram (b) Eccentricity histogram (c) Inclination histogram

(d) Right Ascension of Ascending Node histogram (e) True Anomaly histogram (f) Argument of Perigee histogram

Figure 1.27: *Histograms of classical orbit elements for charging and non-charging propagation*

There are many interesting observations to make from these histograms. Firstly, the spread in all elements after only 24 hours or propagation is very large. All angular elements except incli-

nation and RAAN have at least 10° of spread after only 24 hours, and the semi-major-major axis changes by hundreds of kilometers. The eccentricity and RAAN visually seem to have different populations stemming from different propagators. To test the probability that including electromagnetic effects have no significant effect, hypothesis testing is used. A truth test is used to compute the probability that both sample sets (from using different propagation models) come from the same actual population and any apparent differences would disappear with enough samples. This probability is shown in Tab. 1.11 along with whether the orbital element is effected by electromagnetic effects applying a 5% probability threshold.

Table 1.11: *Hypothesis testing for effect of electromagnetic effects*

Orbital Element	Probability of no Effect	Affected?
Semi-Major Axis	1.96 %	Yes
Eccentricity	9.97e-7 %	Yes
Inclination	76.2%	No
True Anomaly	21.1%	No
RAAN	4.24e-4 %	Yes
Argument of Perigee	44.6%	No

Eccentricity and RAAN have vanishing probabilities of not being effected, and semi-major major axis has a very small one. This means that including electromagnetic effects such as Lorentz forces and torques as well as eddy torques makes a significant difference even when randomizing the initial attitude of the plate. For the example case of an extremely lightweight metallic sheet at -30 kV, including electromagnetic effects is necessary for accurate propagation. The next section will investigate whether electromagnetic effects are as important for other objects and scenarios.

1.1.3.5 Comparison of Torques for General Objects

SRP is the driver for HAMR objects, but it can be steered by electromagnetic torques. This section investigates what objects are susceptible to such electromagnetic torques. First consider the same 10 cm square plate considered in previous analysis, but allow the voltage to vary. If the plate is uncharged electrostatics will no longer act, and earlier analysis shows that at -30 kV it does matter, but is there a charging threshold where electrostatics begin to contribute? To answer this question, the voltage of the plate is varied logarithmically from 10 Volts, which is a normal floating potential, to 100 kV, which is slightly higher than the worst case charging ever modeled.[37] The plate's orbit is propagated for 24 hours, and the torques are recorded. The angular acceleration that the plate experiences due to each perturbation is shown in the log-log plot in Fig. 1.28. The linear accelerations are not shown because the orbit change comes from electromagnetic torques reorienting the plate which changes SRP.

Since all of the torques are attitude dependent, they vary quickly through time as the plate tumbles. To give a sense of the normal variation, the mean and 1-σ bounds are shown. Because many of the torques are logarithmically distributed, the standard deviation is larger than the mean, and does not apply for a non-symmetric distribution. Rather, the logarithms or the angular accelerations are used to make the statistics, then exponentiated for plotting. This is shown below:

$$x' = \log(x) \rightarrow \quad \bar{x} = 10^{\bar{x'}} \tag{1.101}$$

$$\rightarrow \bar{x} \pm \sigma_x = 10^{\bar{x'} \pm \sigma_{x'}} \tag{1.102}$$

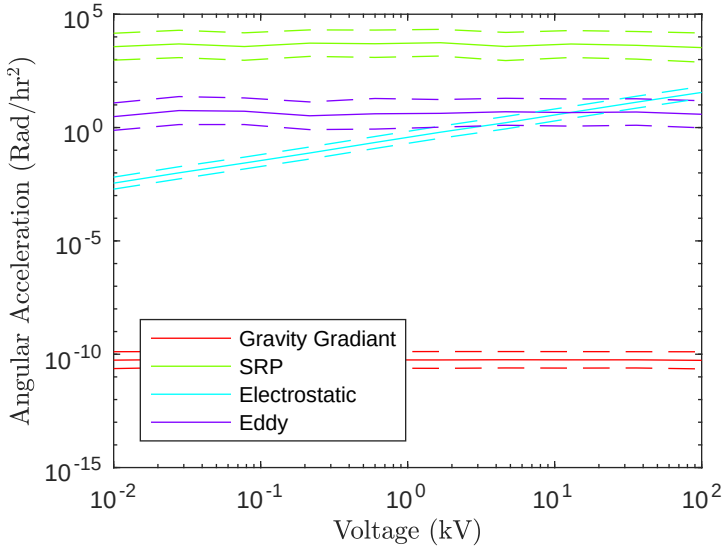

Figure 1.28: *Angular accelerations due to various perturbations at different voltages*

The torques from gravity gradients, SRP, and eddy currents are all relatively constant with voltage, which would be expected. However, the torque from electrostatics rises steadily. If 1 radian is used as an arbitrary marker of a significant attitude change, the time scales on which electrostatics will act can be investigated. For 10 Volts, the mean angular acceleration is 3.5e-3 Rad/hr^2. Using $\Delta\theta = \frac{1}{2}\ddot{\theta}\Delta t^2$ gives a time scale of 23.8 hours. At 600 Volts, the time needed for significant attitude perturbations is 3 hours, and at 100 kV it only takes 14 minutes. Of course this assumes the torque is always about the same body axis, which is not always true but gives a convenient upper bound.

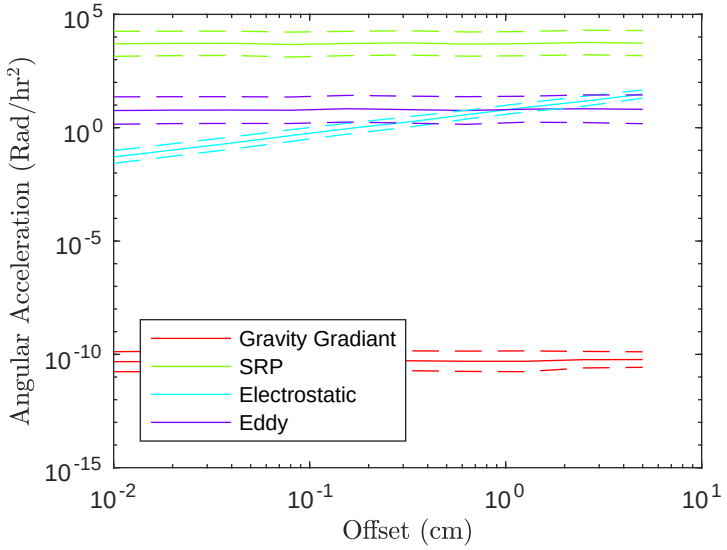

Figure 1.29: *Angular accelerations due to various perturbations at different CM offsets*

This same analysis is repeated varying not voltage but the separation between center of charge and center of mass while the voltage is fixed at 30 kV in Fig. 1.29. Once again all perturbations

except electrostatics are relatively constant, while electrostatic torques grow with the separation, as this lengthens the moment arm. Electrostatics become larger than eddy currents for all offsets larger than 1 cm on this 10 cm square plate, although the variance associated with eddy currents is much larger. Once again using 1 radian as a threshold for significant attitude perturbations that could influence the orbit gives timescales on which charging can act. At 0.1 mm of offset, electrostatic torques will take nearly 6 hours to significantly change the attitude, at 1.5 mm, the timescale is 1.5 hours, and at 5 cm (half the length of the plate), electrostatics have a timescale of only 16 minutes.

Next consider the same thin 10 cm sheet but hold the voltage, separation of center of charge and center of mass, and thickness constant, but allow the initial spin to vary. The initial spin in all prior work is set to zero, but in this section the stability of spinning about an axis of maximum inertia is considered. Intuitively, a frisbee or football will be less susceptible to small torques that would otherwise cause it to tumble if it were spinning faster. Likewise, the thin plate will be less susceptible to small electromagnetic torques if it were spinning stably about its axis of maximum inertia, which is the body z axis.

To study this, consider a plate spinning like a frisbee about its z axis at a rate of ω_0. Apply a torque about the body x axis of $L_x = \chi_S V B \Delta v = (1.1376 * 10^{-13}$ C m$)(30\text{kV})(100\text{nT})(1\text{km/s}) = 3.4127 * 10^{-13}$ Nm for one hour, then propagate normally for another hour. The angle between the body z axis and the inertial z axis (which are aligned at the beginning of the simulation) is plotted below in Fig. 1.30 for a fast initial spin ($\omega_0 = 2^\circ/s$) and a slow initial spin ($\omega_0 = 0.1^\circ/s$). Keep in mind that with no initial spin, this problem becomes 1 dimensional, and after one hour of torque the place should have rotated by $\Delta\theta = \frac{1}{2}\frac{L_x}{I_x}\Delta t^2 = 1723^\circ$, nearly 5 entire rotations.

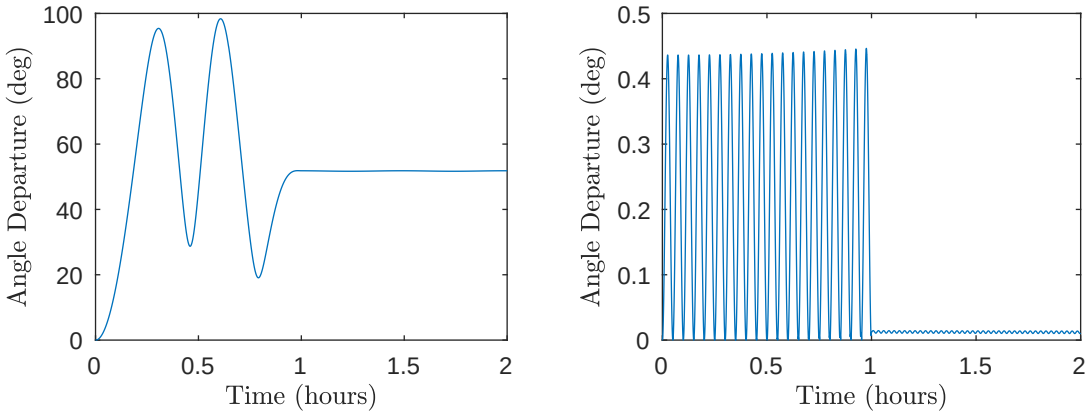

(a) Slow initial spin – $\omega_0 = 0.1^\circ/s$ (b) Fast initial spin $\omega_0 = 2^\circ/s$

Figure 1.30: *Departure from initial sun-pointing angle due to electrostatic torques*

From this simple example the importance of initial spin can be seen dramatically. If the initial spin is a slow 0.1 degrees per second, one hour of electrostatics can change the body attitude, which changes SRP, by 50 degrees. If the initial spin is increased to 2 $^\circ$ per second, the same electrostatic torque only changes the sun pointing angle by a mere 0.01 degrees. Clearly objects spinning stably about the axis of maximum inertia are less susceptible to small electrostatic or eddy torques. As an aside, eddy torques never act about the z axis for plates of vanishing thickness, so they are not able to change the attitude, and therefore the orbits, of thin plates spinning about their maximum inertia axis.

To further investigate the trend illustrated above where objects spinning stably are less suscep-

tible to small torques, vary the initial spin logarithmically from 0.01 to 10 degrees per second and monitor the attitude departure. The attitude is monitored by computing the mean and standard deviation of the angle between the body and inertial z axis in the second hour, after the electrostatic torque has been turned off. This is shown in Fig. 1.31

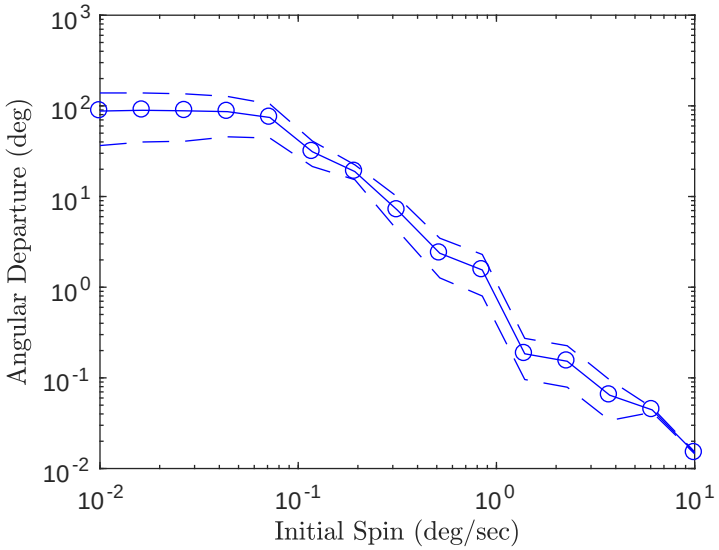

Figure 1.31: *Influence of initial spin on attitude departure*

The mean attitude departure in the second hour is shown as the solid line with the circles and the dashed lines show the 1-σ bounds. When the plate has a low initial spin, (0.01 - 0.1 $^\circ$/s per second), the departure is a nearly flat line, because the body z axis can never be more than 180° from the inertial z axis. For higher initial spin rates ($\omega_0 > 0.1$ $^\circ$/s per second), the departure angle drops quickly. Choosing again the arbitrary marker for significant attitude change of 1 radian ($\sim$ 57°) gives a cutoff spin rate past which electrostatic torques may not have as much influence on the orbit of 0.085 $^\circ$/s per second.

Keep in mind that in this simulation the electrostatic torque is assumed to act completely in the body x axis and be constant. This is not likely in the full coupled problem. Additionally, these results hold only for the 10 cm by 10 cm by 1/4 mil sheet of mylar charged to 30 kV. Heavier and less dramatically charged objects will require smaller stable initial spins to overwhelm the electrostatic torques.

For the thin cases considered earlier, SRP is very sensitive to attitude – if the plate is directly facing the sun the acceleration is thousands of times larger than if the plate faces orthogonal to the sun. For a cube, the attitude only changes the exposed area by a factor of 2 or 3. This shows that objects like plates with highly attitude-dependent cross-sectional are more susceptible to the small torques caused by electrostatics and eddy currents. Additionally this heavier object will be less susceptible to non-gravitational perturbations like electrostatics and SRP.

To explore this, consider the same 10 cm square of Mylar, but allow the thickness to vary from the very thin 1/4 mil (6.35 μm) to 10 cm which turns the sheet into a solid cube of Mylar. As this 10 cm cube weighs 1.39 kg, this is a good approximation of a cubesat. Each of the sheets are propagated for 24 hours, and the linear and angular accelerations are recorded at each time, much like the results shown in Fig. 1.25. The mean and standard deviation are computed for the time-series of the accelerations for each plate thickness and are plotted in Fig. 1.32. The means are plotted as solid lines, and the 1$-\sigma$ bounds are shown as dashed lines. In some cases the

standard deviation is larger than the mean, and the lower bound of the norm is negative and does not appear on this log plot.

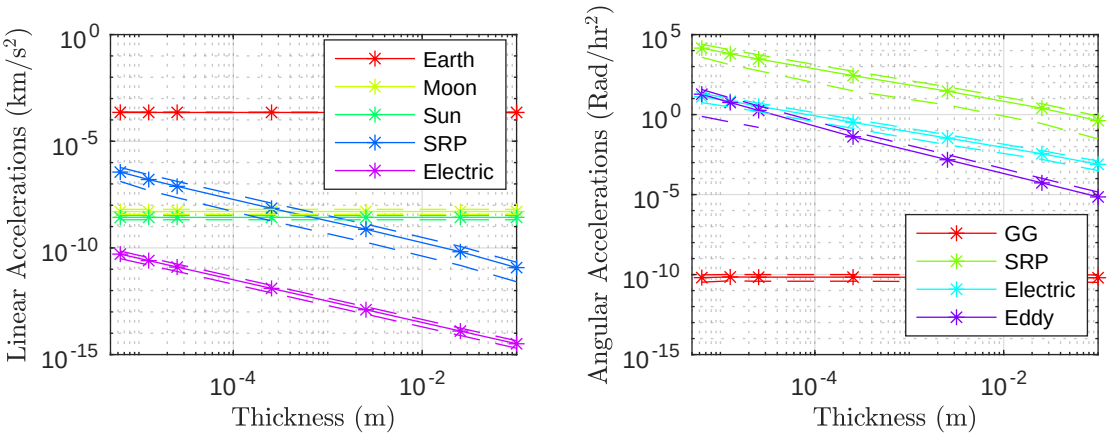

(a) Linear Accelerations (b) Angular Accelerations

Figure 1.32: *Acceleration on plates of varying thickness from different perturbations*

There are many interesting trends in both plots. Considering linear accelerations, the gravitational accelerations are constant with object size. This is expected as mass divides out of the gravitational formula. The non-gravitational accelerations (Lorentz force and SRP) decrease as the plate gets thicker because the force stays roughly constant (the full 3-dimensional SRP calculation is performed, but the self capacitance is assumed to stay constant even though the plate becomes thicker). The Lorentz force is consistently the smallest perturbation, and is nearly 10,000 times smaller than SRP. This will not have a large effect on propagation. For the angular accelerations, gravity gradient accelerations remain constant, as both the torques and the inertia increase as the plate gets thicker. All other accelerations become smaller because of the increasing inertia. SRP is the largest torque, but is followed by electrostatics and eddy torques. Eddy torques have a more negative slope than electrostatics – this is an indirect effect due to the thicker plates spinning up to lower rates, which causes the eddy torques to decrease.

For large heavy objects, the torques will take much longer to change the attitude and "steer" SRP. Furthermore, these objects will not change their exposed areas as much due to rotations, which further suppresses the orbital effects of electromagnetic torques. For small lightweight objects, the small electromagnetic torques can drastically change the orbit by changing the attitude.

1.2 Research Thrust 2: Flexible Shape MSM Applications

1.2.1 Motivation

The original Multi-Sphere Method (MSM) development approximates the electrostatic forces and torques about a general space object, or interacting between multiple closely orbiting space objects, in a faster-than-realtime manner.[2,3] The main benefit of this method is a drastic improvement in the computational speed required to numerically model electrostatic torques and forces compared to finite element or boundary element solutions. The Volume MSM (VMSM) in particular only requires a small set of spheres as base functions and is able to model the forces to within a few percent of accuracy. This enables far faster-than-realtime numerical simulation of the charged

astrodynamics. The MSM models developed thus far all assume the space objects have a fixed shape and conducting outer surface.

This report discusses second year results studying the accuracy of applying the MSM model of a fixed shape to a flexible body. This is explored in this first study on this topic by modeling the charged deformation of a flexible one-dimensional structure. Reference 38 also uses a fixed-shape MSM model that is applied to a deformable shape, but the accuracy of this assumption is not studied. In this paper an MSM model is developed for a non-deformed state, and then used for a range of deformation. To maintain a high computational speed, this assumption avoids a more complex scenario where the MSM is reconfigured for each shape deformation. Of interest is how well such a model is able to predict and approximate the actual electrostatic forces and torques acting on this time varying shape. The accuracy is studied for analytical prototypical shape deformations by comparing numerical flexible MSM simulations to experimental charged actuation results.

1.2.2 Multi-Sphere Method Applied to Flexible Structures

1.2.2.1 Review of Unmodified MSM Technique

MSM is a computationally efficient method of approximating the electrostatic interactions between conductors. Complex spacecraft geometry is replaced with a discrete set of spherical conducting shells to approximate the E-field about a general shape. Two main categories of MSM exist: Volume MSM (VMSM) and Surface MSM (SMSM).[2] VMSM requires that both sphere radii and placement are optimized to match forces and torques,[3] capacitance,[5] or electric fields.[39] SMSM, on the other hand, places spheres equidistantly on the surface of the modeled object, and optimizes only the sphere radii to match any of the physical quantities listed above. For the investigation to follow, a SMSM model using capacitance matching is employed. This papers studies how well the fixed-shape SMSM method can be applied to a flexible one-dimensional string structure.

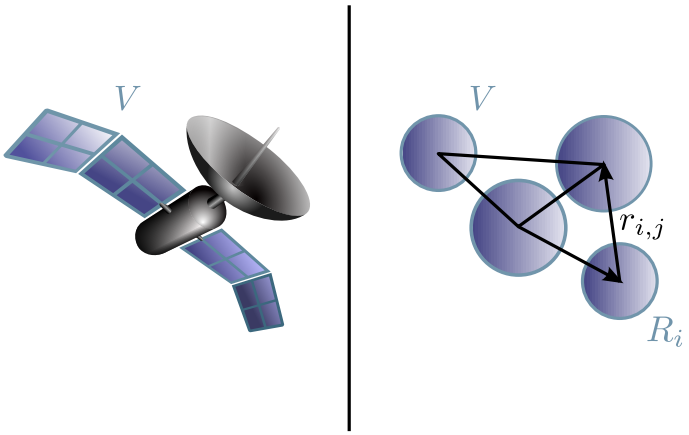

Figure 1.33: *Replacement of complex geometries with SMSM spherical shells*

Figure 1.33 depicts the SMSM concept applied to an object with a fixed geometry and equipotential (i.e. conducting) outer surface. The voltage on each of the spheres shown is related to the charge on that sphere by

$$V_i = k_c \frac{Q_i}{R_i} + k_c \sum_{j=1, j\neq i}^{n} \frac{Q_j}{r_{i,j}} \tag{1.103}$$

where $k_c = 8.99 \times 10^9$ Nm^2/C^2 is Coulomb's constant, R_i is the radius of the i^{th} sphere, and $r_{i,j}$ is the distance between the i^{th} and j^{th} spheres. These relations can be rewritten into a single matrix equation.

$$\begin{pmatrix} V_1 \\ V_2 \\ \vdots \\ V_n \end{pmatrix} = \frac{1}{k_c} \begin{bmatrix} 1/R_1 & 1/r_{1,2} & \dots & 1/r_{1,n} \\ 1/r_{2,1} & 1/R_2 & \dots & 2/r_{2,n} \\ \vdots & \vdots & \ddots & \vdots \\ 1/r_{n,1} & 1/r_{n,2} & \dots & 1/R_n \end{bmatrix} \begin{pmatrix} Q_1 \\ Q_2 \\ \vdots \\ Q_n \end{pmatrix} \quad \rightarrow \quad \mathbf{V} = [S]\mathbf{Q} \tag{1.104}$$

Here, $[S]$ is called the elastance matrix.[4] Another, well-known expression relating charge to voltage, $\mathbf{Q} = [C]\mathbf{V}$ indicates that the capacitance is the inverse of the elastance matrix.

$$\mathbf{Q} = [S]^{-1}\mathbf{V} \tag{1.105}$$

This form is preferable, as the voltage is usually known and the dynamics are dependent on charge. From Eq. (1.105), the Coulomb force experienced by the i^{th} sphere in an electric field is

$$F_{C_i} = Q_i \mathbf{E} \tag{1.106}$$

For rigid structures, the capacitance matrix is constant. For a flexing structure, the relative distances $r_{i,j}$ change as the object flexes as do the charges Q_i. In this paper the application of SMSM to a one-dimensional, flexible conducting structure is explored using a constant capacitance matrix.

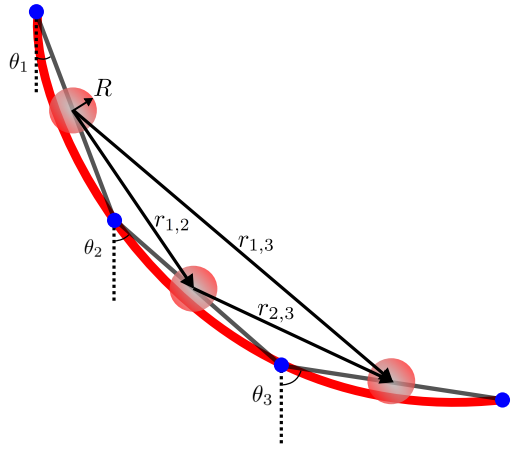

Figure 1.34: *SMSM model of multi-link pendulum*

1.2.2.2 SMSM of a One-Dimensional Wire

Figure 1.34 shows how a flexible wire is modeled as a multi-link pendulum with SMSM spheres placed evenly at the center of each link. The capacitance of a long, thin, straight wire is given by[40]

$$C = \frac{l}{k_c \Lambda}\left[1 + \frac{1}{\Lambda}(1 - \ln(2)) + \frac{1}{\Lambda^2}\left(1 + (1 - \ln(2))^2 - \frac{\pi^2}{12}\right) + \mathcal{O}\left(\frac{1}{\Lambda^3}\right)\right] \tag{1.107a}$$

$$\Lambda = \ln\left(\frac{l}{a}\right) \tag{1.107b}$$

where l is the length of the wire and a is its radius. This equation is valid for large Λ, which requires that the wire length is much greater than the radius. This scalar value is used to optimize the SMSM sphere radius R used in the model. The comparison to the capacitance described in (1.105) is accomplished by summing the members of the matrix capacitance.

$$C_{\text{scalar}} = \sum_{j=1}^{n} \sum_{i=1}^{n} C_{i,j} \tag{1.108}$$

If the wire changes shape, (1.107) no longer holds. In reality, all elements of the capacitance matrix should change, but the SMSM model postulated in later sections holds the matrix constant. Figure 1.35 illustrates the difference between the dynamics resulting from a numerical simulation applying time-varying capacitance versus one with a constant capacitance. The figure shows the percent difference in the inertial angles identified in Figure 1.34 of a 5-link system between the two cases.

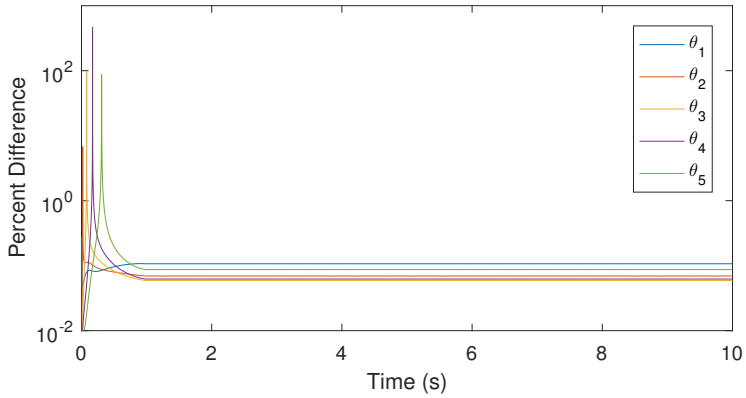

Figure 1.35: *Percent difference between pendulum angles resulting from time-varying capacitance versus constant capacitance*

The analysis to follow considers the steady-state response of the system. This allows a final steady-state shape to be predicted subject to charging and external force field interactions. Matching the time-varying response is the topic of future research. Figure 1.35 shows that, while the dynamics are different between a time-varying and constant capacitance system, the steady-state is nearly identical. Therefore, the use of a constant capacitance matrix optimized using Eq. (1.107) will not significantly affect the results found in this paper. As further validation, Figure 1.36 shows the percent difference in the scalar capacitance calculated from Eq. (1.108). This figure shows that the true, time-varying capacitance does not deviate significantly from the wire capacitance calculated from Eq. (1.107) to which the constant capacitance is optimized. Therefore, Eq. (1.105) should give a nearly constant value for the charge vector $\mathbf{Q}$.

A related question relevant to understanding the applicability of SMSM to flexible structures is the accuracy if the capacitance matrix is modified to account for flexing. In this case, the diagonal elements — the radii of the SMSM spheres — are held constant while the off-diagonal elements change to account for deformation. The case of an anchor ring is considered, as it is another configuration for which there is an analytic capacitance. Reference 41 shows that the capacitance of an anchor ring whose cross sectional radius r is small compared to the ring radius ρ is

$$C = \frac{\pi\rho}{k_c \ln\left(8\rho/r\right)} \tag{1.109}$$

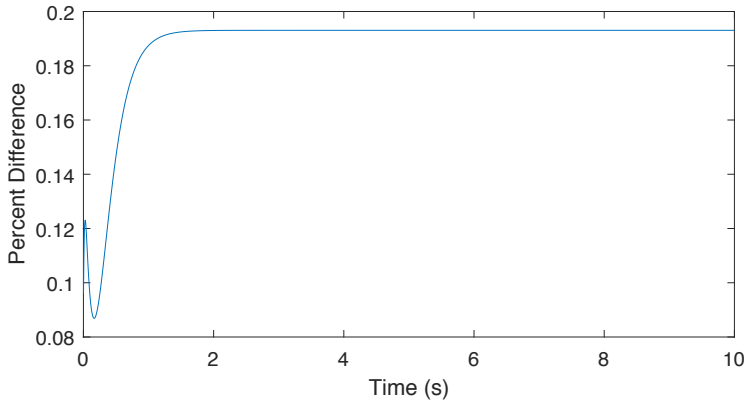

Figure 1.36: *Percent difference between time-varying capacitance and constant capacitance*

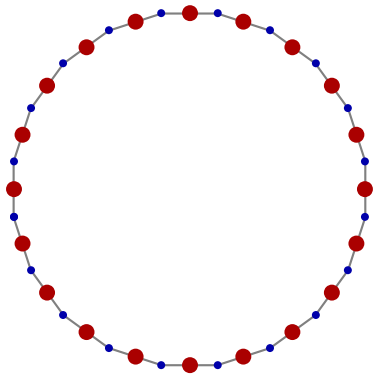

Figure 1.37: *20-link SMSM model of an anchor ring. The blue circles indicate the hinge locations, while the red accurately represent the SMSM sphere radii optimized using Eq.* (1.107)

Two configurations of a 20-link system similar to that shown in Figure 1.34 are compared. First, the link is arrayed as a straight line and the SMSM sphere radii are optimized to match the capacitance in Eq. (1.107). The SMSM system is then rearranged into a ring shape without changing the SMSM sphere locations within each link, or the sphere radii to match the capacitance of the ring. The off-diagonal terms of the capacitance matrix account for this new geometry and the sum of all matrix elements is compared to the analytical result in Eq. (1.109).

The resulting non-optimized SMSM capacitance of the ring calculated using the elastance matrix is within 0.1% of the analytic solution given by Eq. (1.109). A portion of this error is due to the discrete nature of the ring in Figure 1.37. Figure 1.38 shows that the difference between the SMSM capacitance and that from Eq. (1.109) decreases with the number of links. The sign of the error indicates that, up to a 20-link system, the SMSM-calculated capacitance is less than the analytic solution. Given this small error, future work in which a time-varying capacitance is used will likely simulate system dynamics accurately.

1.2.3 Charged Wire Equations of Motion

As shown in Figures 1.34 and 1.39, the flexible, conducting wire studied is approximated as a multi-link pendulum system with SMSM spheres placed at the center of each link. The sphere position is one of several tunable parameters, but is held at link-center for simplicity. To account for the stiffness of the wire, torsional springs are simulated at the hinge points of the model. The

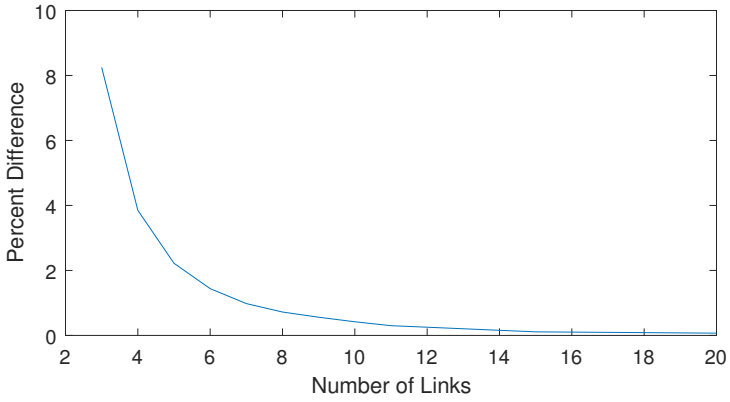

Figure 1.38: *Percent difference between SMSM and analytic anchor ring capacitance for various numbers of links*

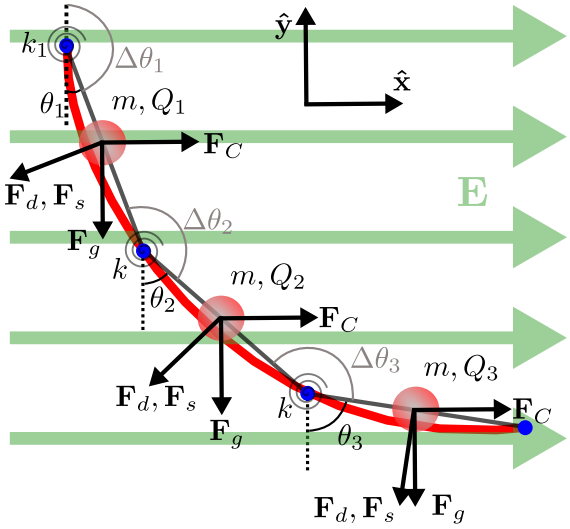

Figure 1.39: *SMSM model of a wire showing forces*

spring constants are main tunable parameter. Note that in Figure 1.39, the first spring is labeled with a different spring constant, k_1, than the others. This accounts for an attachment mechanism in the model that affects only the first link. A schematic of the model and forces are shown in Figure 1.39. Note that the directions of the Coulomb and gravitational forces $\mathbf{F}_C, \mathbf{F}_g$ do not change, while the drag and spring forces, $\mathbf{F}_d, \mathbf{F}_s$ are always opposite of the direction of motion. This model assumes that the wire does not feel its own electric field, so the charges on the SMSM model do not repel each other.

The relationship between a conservative force and the corresponding potential energy is

$$U = -\int \mathbf{\Theta} \cdot \mathbf{ds} \tag{1.110}$$

where $\mathbf{\Theta}$ is a force or torque, and $\boldsymbol{ds}$ is the relevant differential. The gravitational force and spring torque are related to the mass of a link m and the relative angles between two links $\Delta\theta$, respectively.

$$\mathbf{F}_g = mg(-\hat{\mathbf{y}}) \tag{1.111a}$$

$$\boldsymbol{\tau}_s = k(\Delta\theta - \Delta\theta_0)(-\boldsymbol{\Delta\hat{\theta}}) \tag{1.111b}$$

Here g is the gravitational acceleration on Earth's surface, k is the spring constant of the torsional spring, and $\Delta\theta_0$ is the equilibrium angle between the two links. Assuming a perfectly vertical and constant gravitational field

$$U_g = mg(y - y_0) \tag{1.112}$$

Here, $(y - y_0)$ is the height of the center of mass above the equilibrium position. The spring potential energy is clearly dependent only the relative angles between two links.

$$\begin{aligned} U_s = -\int_{\Delta\theta_0}^{\Delta\theta} \boldsymbol{\tau}_s \cdot \boldsymbol{d\Delta\theta'} = -k\int_{\Delta\theta_0}^{\Delta\theta} (\Delta\theta' - \Delta\theta_0)(-\boldsymbol{\Delta\hat{\theta}} \cdot \boldsymbol{\Delta\hat{\theta}}) d\Delta\theta' \\ = \frac{1}{2}k\left[(\Delta\theta - \Delta\theta_0)^2 - (\Delta\theta_0 - \Delta\theta_0)^2\right] = \frac{1}{2}k(\Delta\theta - \Delta\theta_0)^2 \end{aligned} \tag{1.113}$$

As mentioned above, a different spring constant k is used for the first link as for the rest due to the experimental setup. The kinetic energy of each link consists of two components: translation of the center of mass and rotation of a thin rod about its end.

$$T = \frac{1}{2}m\mathbf{v}_{\text{com}} \cdot \mathbf{v}_{\text{com}} + \frac{1}{2}\boldsymbol{\omega}^T I\boldsymbol{\omega} = \frac{1}{2}mv_{\text{com}}^2 + \frac{1}{6}ml^2\dot{\theta}^2 \tag{1.114}$$

Above, v_{com} is a link's center of mass velocity, l is the length of a link, and $\dot{\theta}$ is the inertial angular velocity of a link. The Lagrangian of the multi-link pendulum system is therefore

$$\mathcal{L} = T - U = \sum_{i=1}^{n}\left(\frac{1}{2}mv_{\text{com}_i}^2 + \frac{1}{6}ml\dot{\theta}_i^2 - mg(y_i - y_{0_i}) - \frac{1}{2}k_i[\Delta\theta_i - \Delta\theta_{0_i}]^2\right) \tag{1.115}$$

where n is the number of links. These n, coupled differential equations are numerically solved simultaneously. The dynamics of the system are determined from Lagrange's Equation.

$$\frac{\mathrm{d}}{\mathrm{d}t}\left(\frac{\partial\mathcal{L}}{\partial\dot{q}_i}\right) - \frac{\partial\mathcal{L}}{\partial q_i} = \mathcal{Q}_i \tag{1.116}$$

Here, q is a generalized coordinate — in this case the inertial angle of a link — and $\mathcal{Q}$ is the sum of generalized, non-conservative forces on a given link. Only two such forces are included in this model: air drag and the Coulomb force. A quadratic drag equation is used. The drag coefficient b is the third tunable parameter in the system and is the same for all links. This value determines the settling time of the system, but does not affect the steady-state position of the multi-link system. It is therefore set to a value that brings the modeled wire to its steady-state quickly to match experiment dynamics.

The Coulomb force is applied as a generalized force because, generally, the charge on each sphere is allowed to vary. Under this condition, the force is not conservative. Since the capacitance matrix is held constant for this model, the charges will not change. In this case, the mathematics works out to be identical to if the Coulomb potential were added as a term in the Lagrangian. This allows for ease of implementation when a time-varying capacitance is used in future model iterations. The forces used to calculate the generalized forces are

$$\mathbf{F}_{D_i} = b\mathbf{v}_{\text{com}_i} \cdot \mathbf{v}_{\text{com}_i}(-\hat{\mathbf{v}}_{\text{com}_i}) \tag{1.117a}$$

$$\mathbf{F}_{C_i} = Q_i\mathbf{E} \tag{1.117b}$$

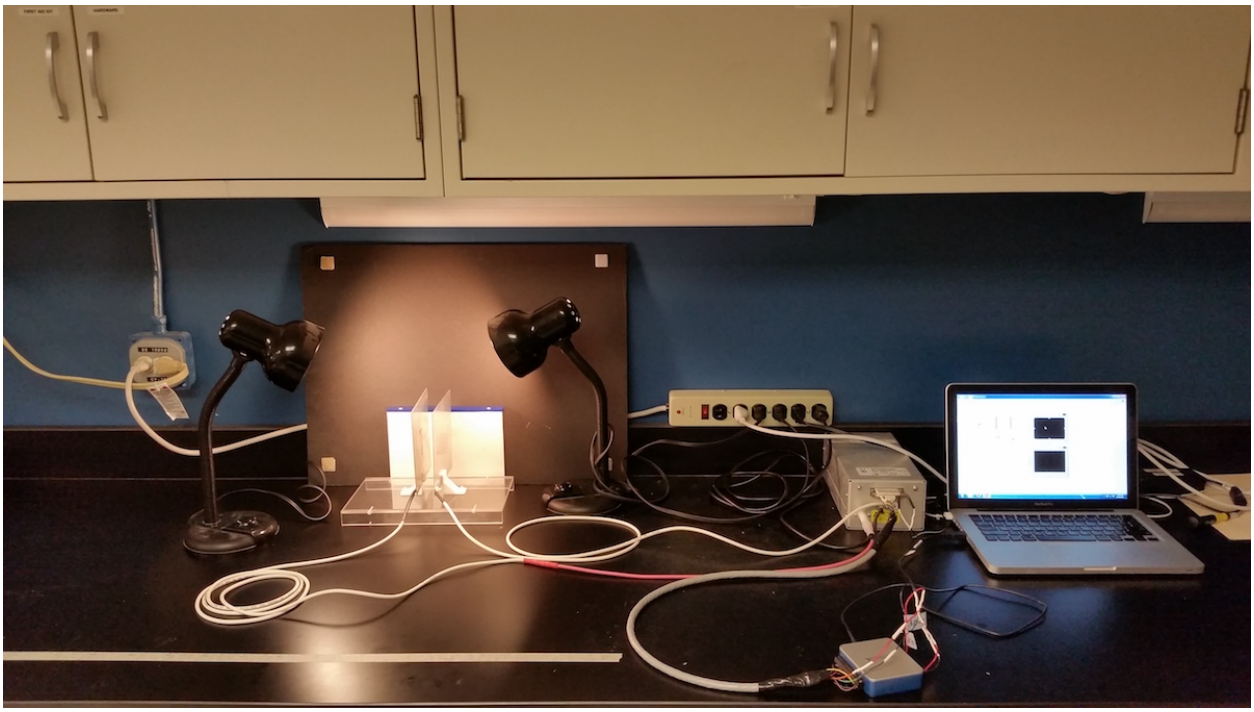

Figure 1.40: *Experimental setup for comparison to computational steady state modeling*

In Eq. (1.117b), Q_i is the charge on the i^{th} sphere and $\mathbf{E}$ is the external electric field. For this paper, only a flat, constant electric field is considered. Therefore, the Coulomb force experience by each link is constant in time.

The equation for the generalized force on the i^{th} sphere corresponding to a non-conservative force $\mathbf{F}_j$ is

$$\mathcal{Q}_i = \sum_{j=1}^{N} \mathbf{F}_j \cdot \frac{\partial \mathbf{r}_j}{\partial q_i} \tag{1.118}$$

where j is a sum over N non-conservative forces, i indicates the relevant link, and $\mathbf{r}_j$ is the position at which a given force is applied. Both drag and Coulomb forces are applied at the center of each link as shown in Figure 1.39.

Mathematica is used to generate and solve the full equations of motion of the multi-link model. Numerical solutions to the equations of motion are used because for large numbers of links the analytical forms are extremely complex. The `NDSolve` function is given initial conditions and integrates the equations of motion to provide the inertial angles and their corresponding angular velocities at each timestep.

1.2.4 Experiment Setup

Validation of the SMSM system to flexible structures is achieved through comparison with experimental results. The goal of this experiment was to apply a potential to a thin strip, take an image of the steady-state configuration and compare to the results from the model described above.

A parallel plate capacitor is chosen to produce a flat electric field. Expansion to more complicated, possibly time varying electric fields will be the subject of future work.

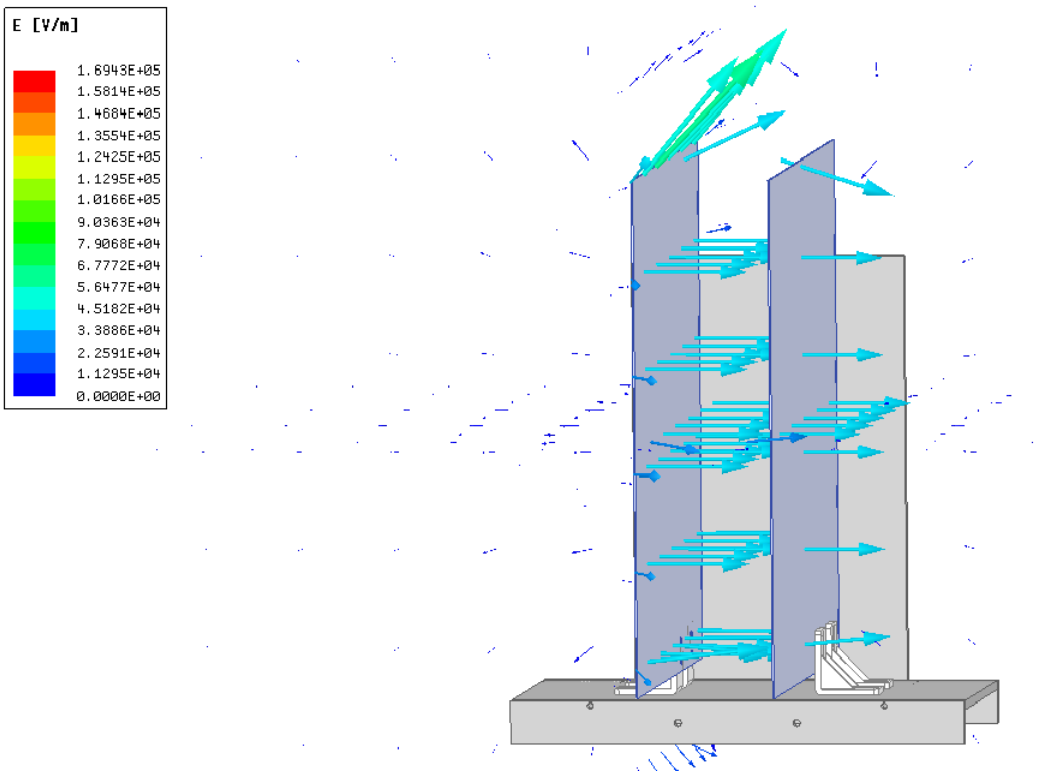

Figure 1.41: *ANSYS Maxwell 3D electric field analysis for experiment structure*

Figure 1.40 shows the experiment setup. The stand-in for a one-dimensional conducting structure is a thin strip of aluminized mylar, which consists of two coatings of 100 $\mathring{A}$ thick aluminum on either side of 2 μm mylar substrate. The aluminum coatings, which are normally isolated by the mylar, are in fact electrically connected due to the cutting process. This strip is attached to the positive plate of the capacitor pictured in Figure 1.40. This ensures that the strip and positive plate are always at the same potential. Future experiments will explore interactions between thin strips at different potentials from the capacitor's cathode.

A Spellman CZE3000 high voltage power supply (HVPS) controlled by LabVIEW via a National Instruments USB data acquisition (DAQ) unit is used to generate large electric fields within the capacitor and put an excess of charge on the thin strip. An image is then taken of the steady-state response of the strip at voltages ranging from 2400 V to 6150 V. A strip of dimension 6 cm $\times$ 2 mm $\times$ 2 μm was used for all experiments.

The commercial finite element solver Maxwell 3D is used to determine the electric field of the parallel plate capacitor used. Figure 1.41 shows the electric field of a modified experimental system from that shown in Figure 1.40 imported into Maxwell 3D with accurate material properties and a voltage drop of $\Delta V = 5$ kV across the plates. This simulation was run at several voltages to determine the electric field for a variety of test voltages. All matched the well-known parallel plate capacitor equation: $E = \frac{\Delta V}{d}$ where d is the plate separation. Note that Figure 1.41 shows that the electric field between the plates is flat everywhere except near edges. The aluminized mylar strip was therefore positioned far from any edges in all experiments.

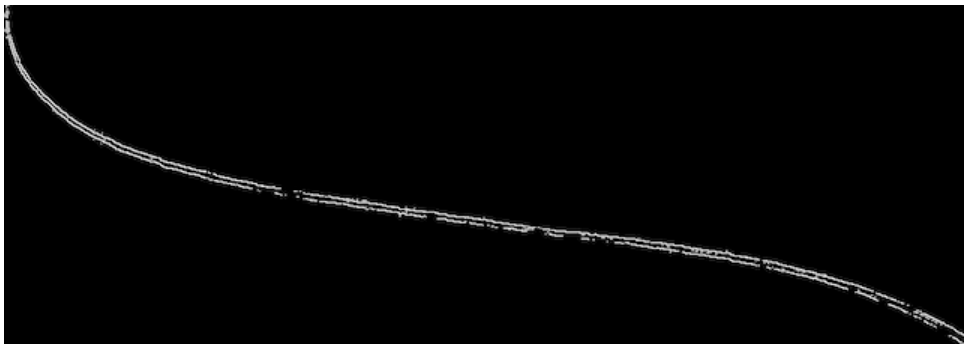

(a) Edge finding result

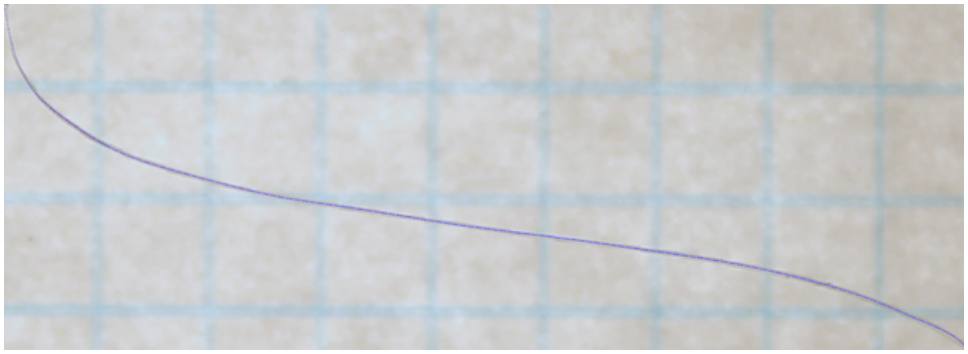

(b) Fit to image data

Figure 1.42: *Image analysis steps.*

1.2.5 Experiment Analysis

As various voltages were applied to the cathode of the parallel plate capacitor pictured in Figures 1.40 and 1.41, images were taken and loaded into MATLAB for analysis. Edge finding algorithms are used to locate the strip and differentiate it from its surroundings. A piece of grid paper is placed behind the experiment to allow for a conversion from pixels to centimeters. The grid also provides an arbitrary vertical direction two which the image can be aligned. This avoids the need of leveling the camera relative to the experiment.

Once the strip is isolated in the image, the points are fit with a 15-degree polynomial using MATLAB's built-in `polyfit` function. This degree was chosen because the resulting polynomial both matches the curvature of the strip and is well conditioned. The polyfit function performed well in fitting all experiment images. The result of edge finding and the final fit of one experiment is shown in Figure 1.42. Once obtained, the polynomial is used to develop a discrete, n-link system for comparison with the n-link model. The positions of the hinges found from image analysis is compared to the steady state hinge positions of the model to determine accuracy.

1.2.6 Model Initialization

One challenge of implementing the numerical model was determining the capacitance of the strip. Recall that Eq. (1.107) is used to optimize the sphere radii in the SMSM model. This equation is for a thin, cylindrical wire, not a flat strip. However, the analysis method required an extremely flexible object that could also be resolved with a camera for comparison with numerical models. No such wire could be found that was also resolvable with the available camera, but efforts are

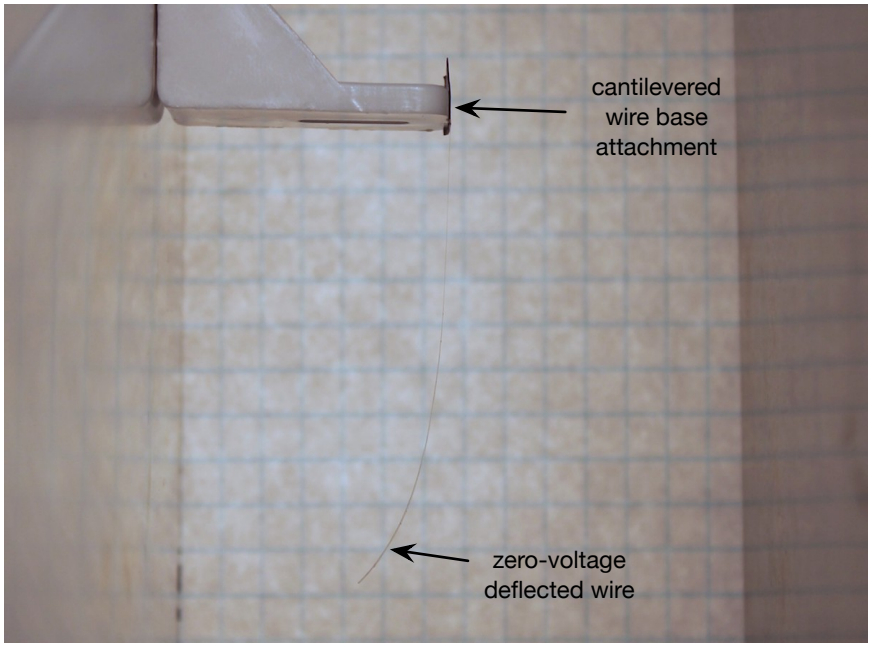

Figure 1.43: *Residual strain on flexible aluminized mylar strip*

continuing for the sake of future investigations.

The capacitance of a flat strip does not have a simple, analytic form, and is difficult to determine with programs like Maxwell 3D because of its extremely thin nature. It was decided to use the total volume of aluminum on the aluminized mylar strip to determine the radius of the fictitious wire being used for capacitance matching. The radius a is therefore

$$V_{\text{wire}} = V_{\text{Al}} \rightarrow \pi a^2 L = L w d_{\text{Al}} \rightarrow a = \sqrt{\frac{V_{\text{Al}}}{\pi L}} = \sqrt{\frac{L w d_{\text{Al}}}{\pi L}} = \sqrt{\frac{w d_{\text{Al}}}{\pi}} \tag{1.119}$$

where w is the width of the strip, L is its length, and d_{Al} is the thickness of the aluminum coating.

The strip initially exhibited some degree of residual stress from the manufacturing, packaging, or cutting processes as shown in Figure 1.43. Rather than attempt to affect the strip to be more flat, a similar process to that shown in Figure 1.42 was used to identify the angles between the n discretized segments. These were then incorporated into the model as the initial inertial angles and as the equilibrium positions for the torsional springs pictured in Figure 1.39.

The method of attaching the strip to the cathode of the parallel plate capacitor with electrical tape creates a hinge about which the strip must bend. This situation is different than bending at any other point in the strip. For this reason, a larger spring constant is used on the first pendulum in the model, as indicated above.

1.2.7 Results

The tuning parameters in the model were the drag coefficient, the aluminized mylar strip capacitance, and the spring constant of the simulated torsional springs. Of these, only the last was changed to match experiment. The system voltages used in experiments are listed in Table 1.12. These voltages were those applied to the strip and to the cathode of the parallel plate capacitor.

Test 1 is used to select the spring constants in the model, and these spring constants are then maintained for the remainder of the tests. The comparison between the image analysis and the

Table 1.12: *System voltages for experiments*

Test #	System Voltages (V)
1	6150
2	5400
3	4650
4	3900
5	3150
6	2400

steady state of the numerical model are shown visually in Figure 1.44. Here, the blue line is the image data representing the unforced strip shown in Figure 1.43. The yellow line represents the experiment fit for each test similar to that shown in Figure 1.42b.

It is clear from the figure that as the voltage gets farther from that in Test 1, the model match begins to degrade. Note however that the shape of the wire seems still to match that of the experiment. The SMSM model is developed to match Test 1, so having a good fit there is expected. Further, these experiments were conducted a sequence of voltages, starting with the 6150V of Test 1. As these tests are performed in atmospheric conditions, the air will ionize about this thin charged structure and cause the electrostatic forces to be different. The impact of this is documented in the charged actuation studies in References 42–44. To see such good agreement in this sequential experiment is very promising. Future work will look at methods to de-ionize the air between experiments, as well as to move the experiment inside a vacuum chamber.

An additional source of error could come from the use of linear, torsional springs in the model. Future iterations of this model will explore the use of non-linear spring constants or different mechanisms entirely of accounting for the strip's resistance to bending. Certainly, an additional source of error is the use of a constant capacitance and the assumption that the strip does not feel its own electric field. Additional computational methods will be explored to incorporate these related affects, which were discarded for computational efficiency. Finally, some small portion of error results from current image analysis methods and experimental setup. The application of a wire capacitance to an aluminzed mylar strip is an unquantified source of error. A search for extremely flexible, conducting wire will be executed. The difficulty is that most highly flexible structures also tend to be extremely thin and therefore difficult to photograph. This adds significant challenge to the experiment analysis.

Figure 1.45 shows the distance between the hinge positions in the model and the discretized experiment fit for each test. Note that the maximum distance is less than a centimeter for all tests. Given the simplicity of the model used in this analysis, these results are promising for future work.

1.3 Research Thrust 3: Dielectric Surfaces

1.3.1 Motivation

MSM has only been applied to continuously conducting spacecraft. Most spacecraft are built to be continuously conducting to avoid differential charging and arcing. However, some of the conducting covering may degrade with time and lose their conductivity. Two scenarios where this may occur is the coverglass coating on the solar panels and the Multi-Layer Insulation. Solar panels require a glass cover to protect from proton radiation, and there is usually a conductive clear coating over the glass, however, this coating may degrade or flake off in space and can

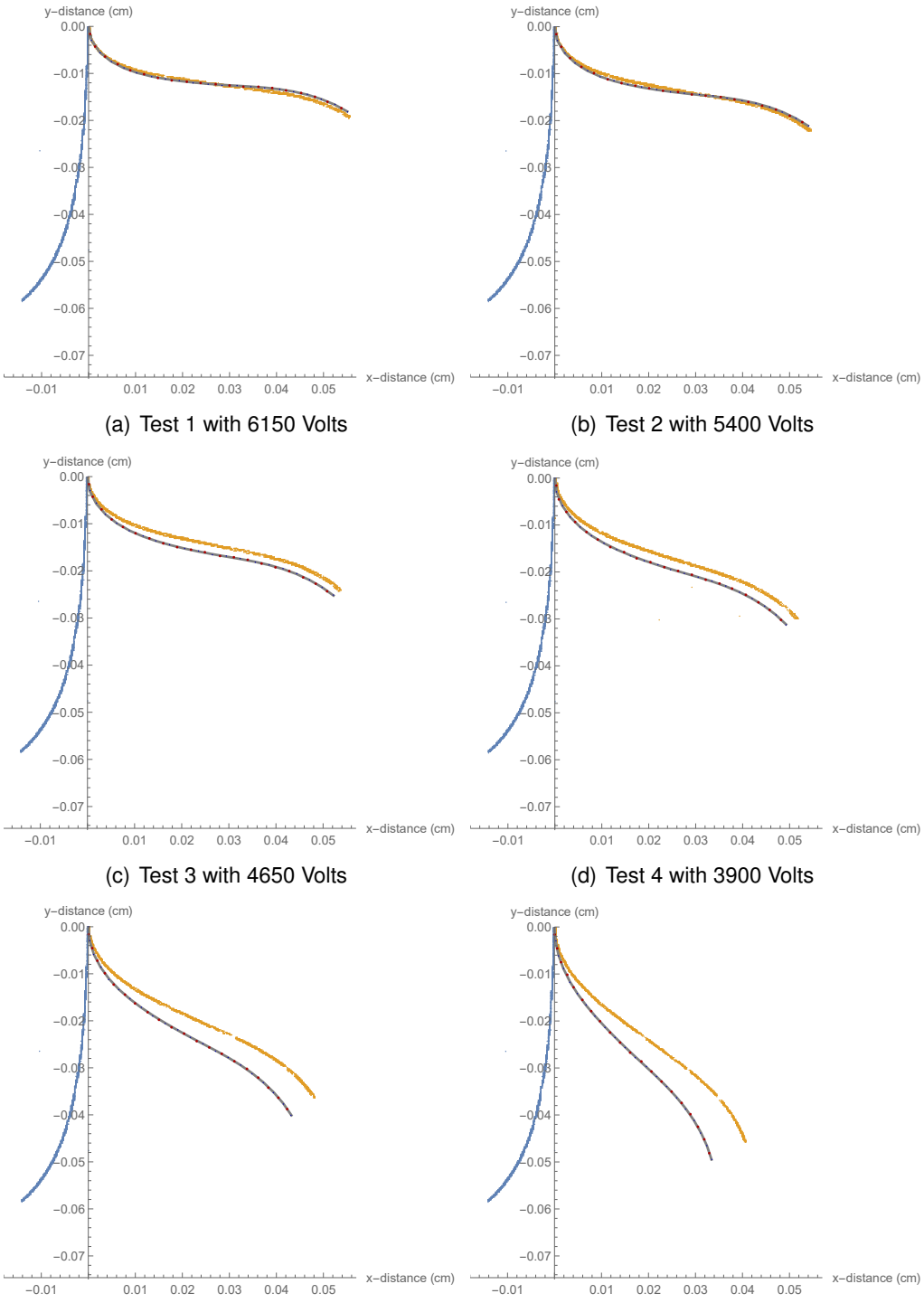

(a) Test 1 with 6150 Volts

(b) Test 2 with 5400 Volts

(c) Test 3 with 4650 Volts

(d) Test 4 with 3900 Volts

(e) Test 5 with 3150 Volts

(f) Test 6 with 2400 Volts

Figure 1.44: *Results of numerical simulations. The blue line represents initial, unforced wire shape while the yellow line represents steady-state experimental configuration. The gray line is the steady-state position calculated using the model described above. On this line, the red spheres represent the placement of the SMSM spheres as well as their actual radii, while the smaller, blue dots represent the breaks between each of the pendulums.*

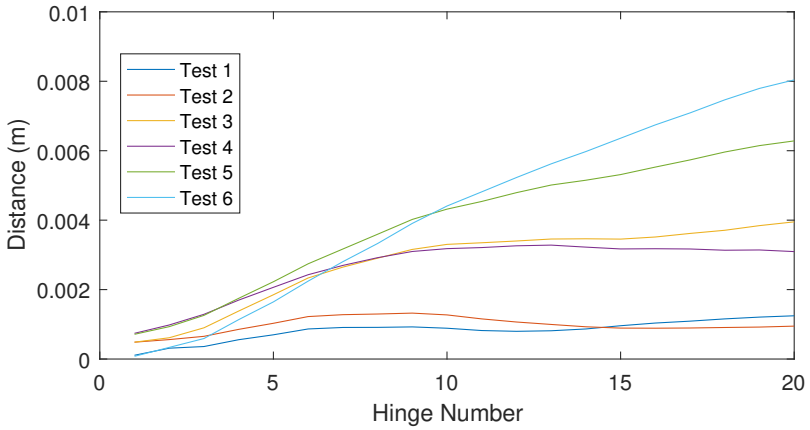

Figure 1.45: *Distance between model and experiment hinge position for each test*

leave sections of the non-conductive glass exposed. MLI also usually has a gold or aluminum coating, but this may flake off or otherwise degrade. Additionally, some spacecraft are not built fully conducting to begin with, and will have large dielectric portions. In the case of coverglass and MLI, there is a thin layer (10-100 μm) of dielectric sitting directly on top of a conductor connected to spacecraft ground. However, in an effort to save weight, some spacecraft have MLI wrapped around a skeleton frame. This complicates matters since part of the dielectric is directly connected to the conducting bus, while the rest is free floating. This case is not considered in this paper.

To estimate the amount of charge stored in a charged dielectric, approximate a complex spacecraft as a parallel plate capacitor. The first plate is the conducting spacecraft bus and the second plate is the surface of the dielectric, thus the separation is the thickness of the dielectric. The mutual capacitance is then $C_m = \frac{\epsilon_0 \epsilon_R A}{d} \approx 0.35$ μF/m^2 for a 1 mil thick sheet of MLI. Assume $\epsilon_R = 1$ for simple computation. The capacitor equation $Q = C_m \Delta V$ gives the difference in charge between the two plates. Assume the spacecraft bus is neutral so that half the charge is on each plate, making the surface charge density on the dielectric 0.17 μC/m^2 V. Thus, a 1 m^2 sheet of 1 mil thick dielectric charged to 200 V different than the spacecraft bus will hold approximately 35 μC of charge. There are many assumptions that go into this simple calculation – the self capacitance of the dielectric is ignored, and the conductor is assumed to be neutral. This calculation is meant to estimate the order of magnitude of the charge density, not to accurately predict it.

The amount of charge will increase linearly with the voltage difference, linearly with the area, and linearly with the relative permittivity. The stored charge increases inversely with the thickness of the dielectric, so doubling the thickness will halve the charge. From this, we conclude that surface charge densities on the order of 35 μC/m^2 are reasonable to assume during a harsh charging event. Keep in mind that an isolated fully conducting sphere of 1m radius will store only 1.1 μC when charged to 10 kV, much less than that stored on the dielectric.

The inclusion of dielectrics introduces two new questions: first, how do dielectrics charge? How much charge is there, and how is it distributed. The second question assumes knowledge of the first, and asks how to best model the inter-craft electrostatic forces quickly and accurately. This paper addresses the second question – Assuming knowledge of the voltage of the conducing spacecraft body and the surface charge density of all conductors, as well as the relative position and attitude, what are the force and torque on both bodies?

1.3.2 The Method of Images

The method of images (MOI) is a trick for solving electrostatic boundary problems by placing point charges outside the boundary that artificially enforce the boundary conditions. It transforms electrostatic problems with boundary problems to problems without boundary conditions on a larger volume. Consider the case of a point charge q a distance y above an infinite grounded conducting plate as shown in Fig. 1.46(a). Charge of opposite polarity will be attracted to the point charge and will pool up below the point charge on the conductor. The system could be solved above the plane with a boundary condition of 0 V on the surface of the plane, or an imaginary image charge q' can be placed a distance y below the surface of the plane. If the image charge is opposite the original charge $q' = -q$, the surface of the plane will be at 0 V due to symmetry and the boundary condition does not have to be enforced. For all computations involving voltage, E field, or force, the imaginary image charge is just as good as the real surface charge distribution.

Now consider the system of a conducting sphere and point charge rather than an infinite plane, as shown in Fig. 1.46(b). For this system, the required image charge to keep the voltage of the surface at a specified voltage is less than the original charge ($q' = -\frac{a}{y}q$) and its position depends on the position of the original charge $y' = \frac{a^2}{y}$. As the point charge approaches the surface of the sphere, the image charge comes forward to meet it, and approaches the equal and opposite charge of the original. Good treatments of the MOI are found in.[14,18] To the author's knowledge, the MOI has only been applied to infinite planes, spheres, and point charges due to symmetry.

(a) Infinite plane (b) Sphere

Figure 1.46: *Method of Images on two simple cases*

The MOI cannot solve the problem of a charged dielectric on the surface of a general shaped conductor, however, it can contribute some insights. As with the point charge near the surface of a conducting sphere, an "image" charged dielectric can be thought of just on the inside of the conductor. For a small and thin dielectric on a large conducting body, the image charge will completely cancel out the original charge. For a larger, thicker dielectric, the image charge will be smaller, and they will be farther apart.

To put rough numbers to this, consider a conducting body of effective radius 1 meter and a dielectric of thickness 20μm that stores 35 muC of charge. The "image" dielectric will lie $R - \frac{R^2}{R+d} \approx 20\mu$m inside of the dielectric, and hold $-\frac{R}{R+d}q \approx -34.9\mu$C. The total charge contributed by the dielectric will be $q + q' \approx 0.7$ nC, a very small amount in comparison to either the charge stored on the dielectric or the conductor. For instance, 0.7 nC translates to $Q/C \approx 6.3$ V on the conductor. Even though the net charge is small, the separation may cause a significant force or torque in a non-flat electric field such as might be generated by a nearby charged spacecraft. Consider a $q_p = 1\mu$C point charge R =5 meters away, the total force caused by the dielectric and image

charge will be

$$F = \frac{1}{4\pi\epsilon_0}\left(\frac{qq_p}{(R-d)^2} + \frac{q'q_p}{(R+d)^2}\right) \approx 31\ \mu\text{C} \tag{1.120}$$

Considering nominal forces $\sim$ 1 mC, this is a small but not insignificant change. As for torques, cross the force with a vector connecting the center of mass to the point about which the force is applied to get approximately T = 30 μCm, also a small but not insignificant fraction of the nominal torques. From this simple example, it seems that the inclusion of charged dielectrics should not change force and torque by a large amount since the image charge will almost cancel out the effects. In the case where the dielectric is far from the conductor, such as where MLI is wrapped directly around the bus, the effects will likely be more significant.

1.3.3 The Multi-Sphere Method Considerations with Dielectric Materials

1.3.3.1 Proposed Modifications for Dielectric MSM

In a conductor, charge will move so that the electric potential energy is at a minimum. This also means that every location on a conductor has the same voltage, even if more or less charge is required to hold that voltage due to mutual interactions. Because the natural charging time for a fully conducting spacecraft is so small, the environmental currents are easily able to provide the extra charge. The natural charging time of a conducting spacecraft is proportional to the self capacitance, here typically $\sim$100 pF.

However, many of the dielectrics used on satellites are very thin, which creates much larger *mutual* capacitances values near $\sim$ 100 nF. This creates a longer natural charging time, which do not allow charge to move on and off fast enough to hold the same voltage. Thus, while conductors can be thought of as lumped *voltages*, dielectrics can be thought of as lumped *charges*. This paradigm, treating the conductors and dielectrics separately, is used to modify MSM to include dielectrics.

The fundamental concept of MSM, that the voltage of every model sphere is a function of its own charge as well as all neighboring spheres is preserved. What changes is that rather than assuming knowledge of all voltages and solving for all charges, now the voltages of all *conducting* spheres and the charge of all *dielectric* spheres is assumed to solve for the charges of all conducting spheres. The charges on the conducting spheres are appended to the apriori known dielectric charges, and the coulomb force and torque can be computed.

To come up with an augmented equation, consider an isolated spacecraft with N conducting spheres and M dielectric point charges.

$$\begin{bmatrix} V_1 \\ \vdots \\ V_N \end{bmatrix} = \begin{bmatrix} S_{1,1} & \dots & S_{1,N} & S_{1,N+1} & \dots & S_{1,N+M} \\ \vdots & & & & & \vdots \\ S_{N,1} & \dots & S_{N,N} & S_{N,N+1} & \dots & S_{N,N+M} \end{bmatrix} \begin{bmatrix} Q_1 \\ \vdots \\ Q_N \\ Q_{N+1} \\ \vdots \\ Q_{N+M} \end{bmatrix} \tag{1.121}$$

$$= [S_C]\boldsymbol{Q}_C + [S_D]\boldsymbol{Q}_D \tag{1.122}$$

Where the C or D subscript indicates conductor or dielectric, respectively. To solve for the unknown $\boldsymbol{Q}_C$, rearrange the equation to yield:

$$[S_C]\boldsymbol{Q}_C = \boldsymbol{V} - [S_D]\boldsymbol{Q}_D \tag{1.123}$$

which can be solved numerically. Keep in mind that this method assumes knowledge of the voltage of the spacecraft bus as well as the surface charge density or total charge on the dielectrics. For a two craft system, both the $[S_C]$ and $[S_D]$ matrices divide into blocks.

The engineer then tunes the size and location of the spheres, which affect the $[S_C]$ and $[S_D]$ matrices. This changes the charges, which change the force and torque. The parameters are tuned so as to produce the same force and torque as a high fidelity truth model.

1.3.3.2 Dielectric MSM test case

Surface MSM (SMSM) is a variant of MSM that uses many equal radius spheres placed equidistantly on the surface of the conductor.[2] Once the positions of all spheres are found, their radius is varied so that the self capacitance of the SMSM model matches that of the physical object, which can be calculated analytically or using a high fidelity FEA program. For dielectrics, the formulation introduced above is used and a sheet of points rather than spheres is placed very close to the surface of the conductor. The spacing between neighboring conducting spheres is used as the separation between conductor surface and dielectric points, but this value could be optimized at a later time.

Consider the special case of a conducting cylinder along the y axis with a diameter of 1 meter and length of 3 meters. This prototype conducting shape has been analyzed in many contexts,[2,3,5,39,43] however a thin dielectric is now added to the positive y end. A SMSM model with 1041 nodes (spheres and point charges) is shown in Fig. 1.47. The conducting body is charged to 30 kV, and the dielectric is given a charge density of 35 μC/m^2 which translates to 27 μC of total charge. For comparison, the conducting cylinder when charged to 30 kV without the dielectric holds just over 3 μC.

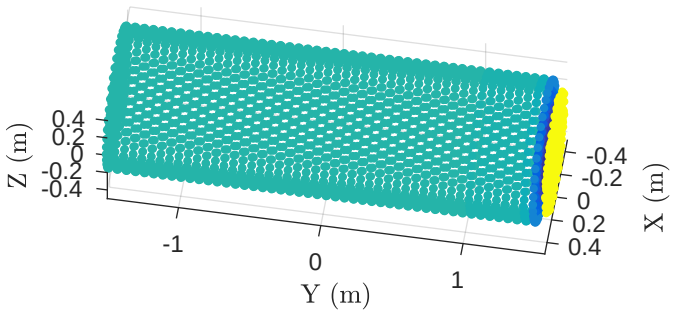

Figure 1.47: *SMSM model of cylinder with charged dielectric end cap. Color indicates charge*

From this model, moments of the charge distribution can be calculated. It has been found that the first two measures, the total charge Q and the electric dipole $\boldsymbol{q}$ are excellent proxies for the force and torque on a body.[17] The total charge is simple to understand, and the electric dipole is the first moment of the charge distribution. Both are defined for the continuum and MSM case for a MSM model with N conducting spheres and M point charges in Eq. (1.124):

$$Q = \int_B \mathrm{d}q = \sum_{i=1}^{N} q_{c_i} + \sum_{i=1}^{M} q_{d_i} \qquad \boldsymbol{q} = \int_B \boldsymbol{r}\mathrm{d}q = \sum_{i=1}^{N} \boldsymbol{r}_i q_{c_i} + \sum_{i=1}^{M} \boldsymbol{r}_i q_{d_i} \tag{1.124}$$

As with any discretized numerical model, the outputs will only be valid for a high enough resolution. To determine that resolution, the number of nodes is varied from 117 to 2544 in 39 steps and the total charge and electric dipole are calculated at each step. The only changing input is the resolution and the goal is to find the resolution at which the solution is a straight line and has no more dependance on the resolution. This is done in Fig. 1.48.

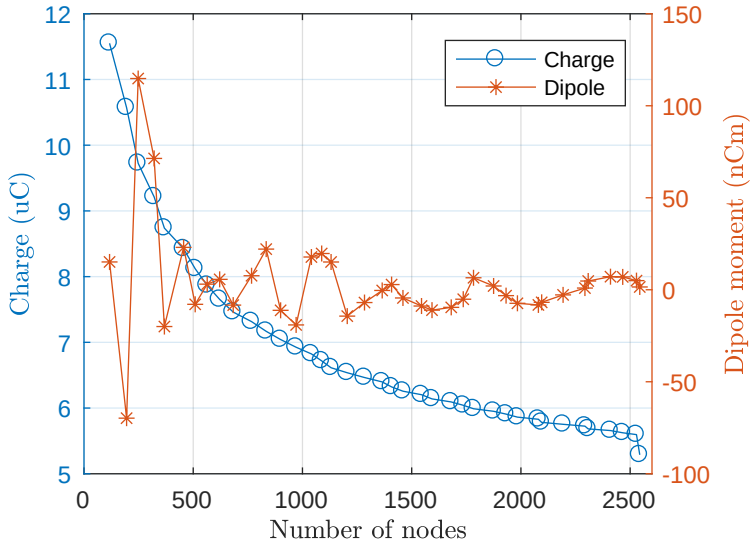

Figure 1.48: *Sensitivity of outputs to number of nodes*

The total charge is plotted with circles on the left axis, and the electric dipole is plotted with asterisks on the right. The total charge is a smooth curve with a decreasing slope. It appears that while the total charge still has some dependency on resolution at this scale, it will eventually become flat if enough spheres are used. At the relatively coarse initial point of 117 nodes, the total charge is near 12 uC, and at the relatively fine resolution of 2544 nodes it is near 5 uC. The MOI would predict that the net charge contributed by the dielectric is nearly zero, which would say that the charge should plateau at around 3.1 μC. The electric dipole, in contrast, takes a lot longer to plateau, and is not monotonic.

Increasing the resolution beyond this point is very computationally demanding, since the brute force method to invert a matrix of size $N \times N$ increases with N^3. To solve the system with only 117 nodes takes 0.6 seconds, while with 2544 nodes it takes more than 3 minutes. This extra time makes it infeasible to use this in dynamical control laws as it is much slower than realtime.

This analysis confirms some of the intuition gained from the MOI analysis. Charge of the opposite polarity does indeed pool up beneath a charged dielectric, and cancels out a lot of the charge from the dielectric. SMSM and MOI do disagree on just how much of that charge is canceled out, although they might agree better if more spheres are used.

1.3.4 Force and Torque Modeling

In this section, three possible approaches are presented for modeling force and torque on a conductor with a charged dielectric. The three approaches are shown pictorially in Fig. 1.49

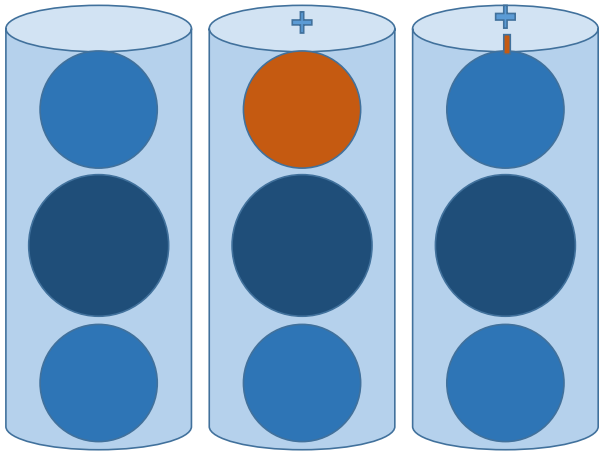

(a) Ignore (b) Point Charge (c) Charge Pair

Figure 1.49: *Three proposed methods for including dielectrics in MSM*

1.3.4.1 Modeling of Conductor

The first and easiest method, shown in Fig. 1.49(a) is to completely ignore the dielectric. For a small dielectric in direct contact with the spacecraft bus, the image charge may cancel out enough of the charge that the force and torque changes are negligible. This method will be most applicable for thin dielectrics sitting directly on the conducting spacecraft surface.

1.3.4.2 Isolated Charge

The second method, shown in Fig. 1.49(b), would be to add one or more point charges where the dielectric physically is. Since the dielectric's position and charge are assumed known, the point charge could be placed without any optimization. The conducting portion of the MSM model could still be optimized though. If more accuracy is needed, the point charge could be allowed to move slightly, and change its charge. This approach would make the nearest sphere in the conducting MSM model take on a charge roughly equal to the image charge.

1.3.4.3 Charge Pairs

The third option, shown in Fig. 1.49(c), would be to add in a pair of point charges for each dielectric present in the system. Since MOI indicates that a static charge exists beneath the surface of the conductor, why not put it there to begin with? As with the second option, the position and magnitude of both point charges could be held fixed at values predicted by MOI, or optimized over. Using pairs of charge that mostly cancel each other out would allow pre-exiting methods for placing MSM spheres inside a conductor to still be used with minimal changes.

Chapter 2

Conclusions and Planned Work

2.1 Conclusions

The second project year was very productive. In particular, the Volume Multi-Sphere-Method (VMSM) process has been greatly revised with the new E-field matching methods. The interesting result from these studies is that even spacecraft geometries with complex non-spherical shapes can be modeled with 2-3 sphere MSM models and introduce only very small approximation errors on the order of a few percent. The new process is more robust and faster to setup than then prior force and torque matching methods. Further, the Appropriate Fidelity Measure (AFM) method has been solved now in its most general form, and applied to simple geometries as well as space debris charged perturbation modeling. While the convergence rate is not as fast as the MSM method, the AFM solution does provide elegant analytical solution suitable for dynamical analysis and stability studies.

The study on using MSM techniques with flexible shapes is progressing well. A modified MSM has be hypothesized, and the resulting total capacitance has been analytically compared to some prototype shape variations. Further, the atmospheric experimental setup has been now fully developed where a thin and flexible wire is charged in a flat E-field environment. The shape capture is done visually using a camera and custom developed software to streamline the workflow of analyzing and recording the shape changes over time.

Modeling di-electrics using MSM methods is progressing well. The charging behavior of di-electrics has been studied, and 2 types of MSM modifications proposed using planted charges and charge pairs. Further, extensive work has been engaged in numerically modeling the prototypical dielectric scenarios in ANSYS Maxwell to create truth models.

The project is on-time and on-cost. An additional 3rd student helped out with the project in the fall which greatly helped advance the VMSM modeling efforts. As an outcome of the program review meeting in December 2016 one of the graduate students was able to spend the summer working at AFRL in Albuquerque working on experimental spacecraft charging and wake studies. Further, the DURIP award was used to purchase extensive experimental equipment to conduct future charged actuation experiments directly in the AVS lab, suitable for the planned year 3 experiments. We are very excited with the range and quality of the results obtained thus far, and looking forward to the 3rd year.

2.2 Year 3 Planned Work

The third year research efforts will proceed as planned focusing mostly on the MSM modifications to consider variable shapes and dielectric charging. The atmospheric experiments will wrap up this fall to be replaced with vacuum chamber based experiments later this calendar year. We have staffed the project with all required graduate research assistant who are eager and well-qualified to pursue this research.

Bibliography

[1] Hughes, J. and Schaub, H., "Charged Geosynchronous Debris Perturbation Using Rapid Electromagnetic Force and Torque Evaluation," *Advanced Maui Optical and Space Surveillance Technologies Conference*, Maui, Hawaii, Sept. 20–23 2016.

[2] Stevenson, D. and Schaub, H., "Optimization of Sphere Population for Electrostatic Multi Sphere Model," *IEEE Transactions on Plasma Science*, Vol. 41, No. 12, Dec. 2013, pp. 3526–3535, doi:10.1109/TPS.2013.2283716.

[3] Stevenson, D. and Schaub, H., "Multi-Sphere Method for Modeling Electrostatic Forces and Torques," *Advances in Space Research*, Vol. 51, No. 1, Jan. 2013, pp. 10–20, doi:10.1016/j.asr.2012.08.014.

[4] Smythe, W. R., *Static and Dynamic Electricity*, McGraw–Hill, 3rd ed., 1968.

[5] Chow, P., Hughes, J., Bennett, T., and Schaub, H., "Automated Sphere Geometry Optimization For The Volume Multi-Sphere Method," *AAS/AIAA Spaceflight Mechanics Meeting*, Napa Valley, California, Feb. 14–18 2016, pp. 2223–2240, Paper No. AAS-16-472.

[6] Schaub, H., "Faster-than-Realtime Electrostatic Force and Torque Modeling for SSA Applications," AFOSR Annual Report, University of Colorado, Aerospace Engineering Sciences Department, Boulder, CO, September 14 2016.

[7] Maxwell, J., *A Treatise on Electricity and Magnetism*, Oxford University Press, 1893.

[8] Lekner, J., "Electrostatics of two charged conducting spheres," *Proceedings of the Royal Society of London A: Mathematical, Physical and Engineering Sciences*, Vol. 468, No. 2145, 2012, pp. 2829–2848, doi:10.1098/rspa.2012.0133.

[9] Bauer, R., "Distriubtion of Points on a SPhere with Applicaiton to Star Catalogs," *AIAA Journal of Guidance, Control, and Dynamics*, Vol. 23, No. 1, 2000, pp. 130–137, doi:10.2514/2.4497.

[10] Grafarend, E., ENgles, J., and Varga, P., "The temporal variation of the spherical and Cartesian multipoles of the gravity field: the generalized MacCullagh representation," *Journal of Geodesy*, 2000.

[11] Hou, X., Scheeres, D. J., and Xin, X., "Mutual potential between two rigid bodies with arbitrary shapes and mass distributions," *Celestial Mechanics and Dynamical Astronomy*, 2016, pp. 1–27.

[12] Scheeres, D. J., *Orbital Motion in Strongly Perturbed Environments*, Springer, Berlin, 2012.

[13] Gibson, W. C., *The method of moments in electromagnetics*, Chapman & Hall, November 28 2007.

[14] Jackson, J. D., *Classical Electrodynamics*, John Wiley & Sons, 1999.

[15] Price, S. L., Stone, A. J., and Alderton, M., "Explicit Formulae for the Electrostatic Energy, Forces and Torques between a Pair of Molecules of arbitrary symmetry," *Molecular Physics*, Vol. 52, No. 4, 1984, pp. 987–1001, doi:10.1080/00268978400101721.

[16] Hughes, J. and Schaub, H., "Appropriate Fidelity Electrostatic Force Evaluation Considering a Range of Spacecraft Separations," *AAS/AIAA Spaceflight Mechanics Meeting*, Napa Valley, California, Feb. 14–18 2016, pp. 3417–3434, Paper No. AAS-16-486.

[17] Hughes, J. and Schaub, H., "Spacecraft Electrostatic Force And Torque Expansions Yielding Appropriate Fidelity Measures," *AAS Spaceflight Mechanics Meeting*, San Antonio, TX, Feb. 5–9 2017, Paper AAS 17–441.

[18] Griffiths, D. J., *Introduction to Electrodynamics*, Prentice Hall, 3rd ed., 1999.

[19] Schaub, H. and Junkins, J. L., *Analytical Mechanics of Space Systems*, AIAA Education Series, Reston, VA, 3rd ed., 2014, doi:10.2514/4.102400.

[20] Giancoli, D. C., *Physics for Scientists and Engineers*, Pearson Prentice Hall, 2008.

[21] Bennett, T. and Schaub, H., "Touchless Electrostatic Three-Dimensional Detumbling of Large GEO Debris," *Journal of Astronautical Sciences*, Vol. 62, No. 3, Sept. 2015, pp. 233–253, doi:10.1007/s40295-015-0075-8.

[22] Schildknecht, T., Muscia, R., Plonera, M., Beutlera, G., Fluryb, W., Kuuselac, J., de Leon Cruzd, J., and de Fatima Dominguez Palmerod, L., "Optical observations of space debris in GEO and in highly-eccentric orbits," *Advances in Space Research*, 2004, pp. 901–911.

[23] Wiesel, W. E., "Estimating Nongravitational Accelerations on High Area-to-Mass Ratio Objects," *AIAA Journal of Guidance, Control, and Dynamics'*, Vol. 39, No. 6, 2016, pp. 1438–1443, doi:10.2514/1.G001464.

[24] Schildknecht, T., Musci, R., Frueh, C., and Ploner, M., "Color Photometry and Light Curve Observations of Space Debris in GEO," *Procedings of the Internaitonal Astronautical Congress*, 2008.

[25] Dever, J. A., de Groh, K. K., Townsend, J. A., and Townsend, J. A., *Mechanical Properties Degradation of Teflon FEP returned from the Hubble Space Telescope*, American Institute of Aeronautics and Astronautics, 1998.

[26] Fennell, J. F., Koons, H. C., Leung, M., and Mizera, P., "A review of SCATHA satellite results: Charging and discharging," Tech. report, Space Division Air Force Systems Command, Los Angeles Air Force Station, Aug. 1985.

[27] Früh, C., Ferguson, D., Lin, C., and Jah, M., "The Effect of Passive Electrostatic Charging on Near-Geosyncronous High Area-To-Mass Ratio Objets," *International Astronautical Congress*, Vol. 64, 2013.

[28] Paul, S. N. and Früh, C., "Space Debris Charging and its Effect on Orbit Evolution," *AIAA/AAS Astrodynamics Specialist Conference*, Long Beach, CA, Sept. 12–15 2016.

[29] Malaspina, D. M., Wygant, J. R., adn G. D. Reeves, R. E. E., Skoug, R. M., and Larsen, B. A., "Electric field structures and waves at plasma boundaries in the inner magnetosphere," *Journal of Geophysical Research (Space Physics)*, Vol. 120, 2015, pp. 4246–4263.

[30] Lai, S. T., *Fundamentals of Spacecraft Charging: Spacecraft Interactions with Space Plasmas*, Princeton University Press, 2011.

[31] Gómez, N. O. and Walker, S. J., "Eddy currents applied to de-tumbling of space debris: Analysis and validation of approximate proposed methods," *Acta Astronautica*, Vol. 114, 2015, pp. 34–53, doi:10.1016/j.actaastro.2015.04.012.

[32] Wie, B., *Space Vehicle Dynamics and Control*, AIAA Education Series, Reston, VA, 2nd ed., 2008.

[33] Tsyganenko, N. A., "A Magnetospheric magnetic field model with a warped tail current sheet," *Planetary and Space Science*, Vol. 37, 1989, pp. 5–20.

[34] Allen, D. N. D. G. and Dennis, S. C. R., "The Application of Relaxiation Methods to the Solution of Differential Equations in Three Dimensions," *Quarterly Journal of Mechanics and Applied Mathematics*, Vol. 6, 1953, pp. 87.

[35] Reitan, D. K. and Higgins, T. J., "Accurate Determination of the Accurate Determination of the Capacitance of a Thin Rectangular Plate," *Transactions of the American Institute of Electrical Engineers, Part I: Communication and Electronics*, Vol. 75, No. 6, 1957, pp. 761–766.

[36] McMahon, J. and Scheeres, D. J., "A New Navigation Force Model for Solar Radiation Pressure," *AIAA Journal of Guidance, Control and Dynamics*, Vol. 33, No. 5, 2010, pp. 1418–1428.

[37] Ferguson, D. C., Denig, W. F., and Rodriguez, J. V., "Plasma Conditions During the Galaxy 15 Anomaly and the Possibility of ESD from Subsurface Charging," *AIAA Aerospace Sciences Meeting including the New Horizons Forum and Aerospace Exposition*, Orlando, FL, January 4–7 2011, Paper AIAA 2011-1061.

[38] Aslanov, V. S., "Chaotic Dynamics of a Satellite with Flexible Appendages in the Coulomb Interaction," *Journal of Guidance Control and Dynamics*, (in review).

[39] Ingram, G., Hughes, J., Bennett, T., Reilly, C., and Schaub, H., "Autonomous Volume Multi-Sphere-Model Development Using Electric Field Matching," *AAS Spaceflight Mechanics Meeting*, San Antonio, TX, Feb. 5–9 2017, Paper AAS 17-451.

[40] Jackson, J. D., "Charge density on thin straight wire , revisited Charge density on thin straight wire , revisited," *American Journal of Physics*, Vol. 789, No. 68, 2000, doi:10.1119/1.1302908.

[41] Thomas, T., "The Capacitance of an Anchor Ring," *Australian Journal of Physics*, Vol. 7, 1954, pp. 347, doi:10.1071/PH540347.

[42] Seubert, C. R. and Schaub, H., "Closed-Loop One-Dimensional Charged Relative Motion Experiments Simululating Constrained Orbital Motion," *AIAA Journal of Guidance, Control, and Dynamics*, Vol. 33, No. 6, Nov.–Dec 2009, pp. 1856–1865, doi:10.2514/1.48274.

[43] Stevenson, D. and Schaub, H., "Terrestrial Testbed For Remote Coulomb Spacecraft Rotation Control," *International Journal of Space Science and Engineering*, Vol. 2, No. 1, 2014, pp. 96–112, doi:10.1504/IJSPACESE.2014.060111.

[44] Stevenson, D. and Schaub, H., "Electrostatic Spacecraft Rate and Attitude Control - Experimental Results and Performance Considerations," *Acta Astronautica*, Vol. 119, Feb. – March 2016, pp. 22–33, doi:j.actaastro.2015.10.023.